Three Dimensional Characterization of Microstructural Effects on Spall Damage in Shocked Polycrystalline Copper

by

Andrew Brown

A Dissertation Presented in Partial Fulfullment
of the Requirements for the Degree
Doctor of Philosophy

Approved February 2015 by the
Graduate Supervisory Committee:

Pedro Peralta, Chair
Marc Mignolet
Karl Sieradzki
Kiran Solanki
Hanqing Jiang

Arizona State University

May 2015

ABSTRACT

Shock loading is a complex phenomenon that can lead to failure mechanisms such as strain localization, void nucleation and growth, and eventually spall fracture. The length scale of damage with respect to that of the surrounding microstructure has proven to be a key aspect in determining sites of failure initiation. Studying incipient stages of spall damage is of paramount importance to accurately determine initiation sites in the material microstructure where damage will nucleate and grow and to formulate continuum models that account for the variability of the damage process due to microstructural heterogeneity, which is the focus of this research. Shock loading experiments were conducted via flyer-plate impact tests for pressures of 2-6 GPa and strain rates of 10^5/s on copper polycrystals of varying thermomechanical processing conditions. Serial cross sectioning of recovered target disks was performed along with electron microscopy, electron backscattering diffraction (EBSD), focused ion beam (FIB) milling, and 3-D X-ray tomogrpahy (XRT) to gain 2-D and 3-D information on the spall plane and surrounding microstructure. Statistics on grain boundaries (GB) containing damage were obtained from 2-D data and GBs of misorientations 25° and 50° were found to have the highest probability to contain damage in as-received (AR), heat treated (HT), and fully recrystallized (FR) microstructures, while {111} Σ3 GBs were globally strong. The AR microstructure's probability peak was the most pronounced indicating GB strength is the dominant factor for damage nucleation. 3-D XRT data was used to digitally render the spall planes of the AR, HT, and FR microstructures. From shape fitting the voids to ellipsoids, it was found that the AR microstructure contained greater than 55%

intergranular damage, whereas the HT and FR microstructures contained predominantly transgranular and coalesced damage modes, respectively. 3-D reconstructions of large volume damage sites in shocked Cu multicrystals showed preference for damage nucleation at GBs between adjacent grains of a high Taylor factor mismatches as well as an angle between the shock direction and the GB physical normal of ~30°-45°. 3-D FIB sectioning of individual voids led to the discovery of uniform plastic zones ~25-50% the size of the void diameter and plastic deformation directions were characterized via local average misorientation maps. Incipient transgranular voids revealed from the sectioning process were present in grains of high Taylor factors along the shock direction, which is expected as materials with a low Taylor factor along the shock direction are susceptible to growth due their accomodation of plastic deformation. Fabrication of square waves using photolithography and chemical etching was developed to study the nature of plasticity at GBs away from the spall plane. Grains oriented close to <0 1 1> had half the residual amplitudes than grains oriented close to <0 0 1>.

ACKNOWLEDGMENTS

I would like to thank my advisor, Dr. Pedro Peralta, for extending an invitation to be a part of his research group nearly five years ago and being there to answer any and all questions I have had...whether they were research related, regarding coursework, or finding out what exactly did happen to Mr. Garibaldi? I would also like to thank my predecessors Leda Wayne and Stephen DiGiacomo for the groundwork they have laid on my research. Very special thanks also go out to my co-workers: Karin Rudman, Kapil Krishnan, Robert McDonald, Harn Lim, Quan Pham, and Jenna Lynch for helping out during crunch times and for all those awesome Taco Tuesdays! Very special thanks also go out to my loving and supporting better half, Catherine McLeod. I appreciate all you have done for me in the final years of my academic journey and always being by my side through thick and thin. The biggest thanks of all go to my parents; they have been supportive of my endeavors throughout my entire life and always show their love and support.

Additionally, I would like to dedicate this work to “Uncle” Dan Wingard, whom was always inquisitive about my research progress and never failed to provide me with comic relief on a regular basis.

This work was funded by Los Alamos National Laboratory under the Laboratory Directed Research and Development – Directed Research (LDRD-DR) program, project #20060021DR, and by the National Nuclear Security Administration under grants # DE-FG52-06NA26169, DE-FG52-10NA29653, and DE-NA002005.

TABLE OF CONTENTS

Page

CHAPTER

CHAPTER Page

LIST OF TABLES

LIST OF FIGURES

Figure Page

Figure Page

Figure Page

Figure Page

Figure Page

1. MOTIVATION

Due to an international ban on the testing of nuclear weapons, there have been no nuclear weapons testing by the United States since 1992 and the entire stockpile of remaining nuclear weapons is at least 20 years of age. The stability of these devices over time is of paramount concern for national security and the research under the National Nuclear Security Administration's (NNSA) Stockpile Stewardship Program (SSP) is vital for the preservation of these devices as well as understanding the physics of shock loading in the detonation process. The NNSA supports progress towards fundamental characterization of materials that aide the development and implementation of advanced computing techniques for materials under extreme conditions, including, but not limited to: high pressures, high strain rates, chemical degradation of fissile material, and loading under high temperature conditions. The development of advanced computational models capable of simulating the detonation of a nuclear weapon is necessary because of the international ceasing of testing. Studying shock physics and material responses subject to shock loading is also of great importance in understanding other dynamic events with similar loading conditions, such as: ballistic impact, blast loading, debris impacts on space vehicles and satellites, automobile crash, large scale geological events (earthquakes, volcanic eruptions), etc. Advancements in supercomputers enable computational models to be utilized for predicting damage due to shock loading and serve as an invaluable resource that must be supported by experimental validation. Microstructural properties and material strength were once thought of as unimportant at shock pressures, but it has since been shown that variations in microstructure in engineering alloys (e.g., steels and aluminum alloys) affect the damage modes in a material. Observing how materials respond to extreme conditions on the microstructural level is a practical way to characterize damage nucleation in a controlled laboratory environment and provides data for statistical studies and advanced microstructure-based computer models. The predominant mode of failure in metallic materials subject to shock loading conditions similar to those found in the detonation of a nuclear device is spall failure. Understanding the physics of wave propagation through a continuum and subsequent material response during this process is of great interest.

Upon an impact, a shock wave propagates through the material producing internal stresses well beyond the elastic limit, resulting in plasticity and potentially spallation. Effects of variables in the loading conditions such as: impact pressure, pulse duration, impact zone, etc, have been explored extensively in the literature [1-10]. Extensive work has been reported on the role microstructure plays in spall failure, and it has been shown that the spall strength can be affected by material anisotropy [5, 6, 10-14], grain size [5, 10, 14, 15], intrinsic defects such as grain boundaries (GBs) and triple points [2, 3, 5, 10, 12-30], and extrinsic defects such as precipitates and inclusions [2, 3, 5]. Studying spall failure at its initiation, or, incipient, stage is of extreme importance to further understand the weak links in a material and how to further improve the material to withstand high dynamic loads. This understanding of the spall process with regards to the material also improves upon computational efforts that accurately predict spall failure.

2. LITERATURE REVIEW

2.1 Fundamental Shock Physics

Wave propagation is an important phenomenon that affects a medium when subjected to local excitations. Upon excitation, the disturbance in a medium propagates as a stress wave with a velocity of [1]:

$$C^2 = \frac{1}{\rho}\frac{\partial \sigma}{\partial \varepsilon} \tag{1}$$

At some point the amplitude of the stress waves may result in a stress state that greatly exceeds the dynamic yield strength of the material. This occurrence, coupled with appropriate geometric constraints for a uniaxial strain condition, results in the compressive hydrostatic component of the stress becoming much greater than that of the shear stresses. Uniaxial strain conditions present in the compressed region lead to convexity in the stress-strain curve [1]:

$$\frac{\partial}{\partial \varepsilon}\left(\left.\frac{\partial \sigma}{\partial \varepsilon}\right|_S\right) > 0 \tag{2}$$

This causes the wave front to steepen up; resulting in a rapid discontinuity of pressure, temperature, and density. Thus the definition of a shock wave arises: a traveling discontinuity of pressure, temperature, and density [1]. Shocks are inherently stable and are assumed to have no apparent thickness [1]. The fundamental requirement for establishing a shock wave is that the velocity of the shock pulse increases with increasing pressure [1].

Shock waves exist in an elastic-plastic solid in three well defined pressure regimes: 1) purely elastic: where the waves are assumed to be acoustic in nature, 2) elasto-plastic: a two-wave structure is present, and 3) hydrodynamic: stresses are high enough to neglect the shear strength of the material altogether [16]. The critical pressure for which plasticity occurs is known as the Hugoniot elastic limit (HEL). It is important to study and understand elastic waves because the shock wave is preceded by an elastic wave for materials shocked in certain pressure ranges, known as the elastic precursor, [31] and the initial release waves generated immediately after a shock wave reaches a free surface behave elastically. The longitudinal wave velocity in an elastic body below the HEL depends on the bulk modulus (K), shear modulus (G), and the density (ρ) [18]:

$$C_l = \left(\frac{K+\frac{4}{3}G}{\rho}\right)^{\frac{1}{2}} \qquad (3)$$

As previously stated, for pressures above the HEL one may neglect shear effects when determining the wave velocity [18]:

$$C_0 = \left(\frac{K}{\rho}\right)^{\frac{1}{2}} \qquad (4)$$

As a shock wave propagates through a material, the mass, momentum, and energy are all conserved across the discontinuity and the Rankine-Hugoniot equations can be used to represent these conservation conditions [1].

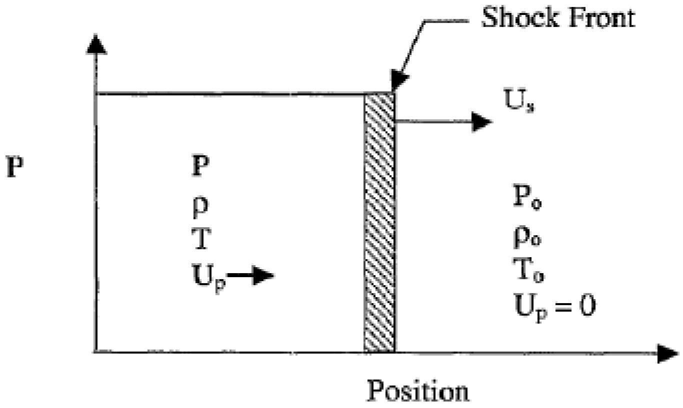

Figure 1: Shock front profile propagating through a material [32].

Conservation of mass: $\rho_0 U_S = \rho(U_S - U_P)$ (5)

Conservation of momentum: $P - P_0 = \rho_0 U_S U_P$ (6)

Conservation of energy: $E - E_0 = \frac{1}{2}(P + P_0)\left(\frac{1}{\rho_0} - \frac{1}{\rho}\right)$ (7)

Where ρ is the density of the material, U_S is the shock velocity, U_P is the particle velocity, E is the energy, and P is the pressure in Figure 1 and equations 5-7. A fourth equation called the equation of state (EOS) may be experimentally determined and relates two or more variables from the Rankine-Hugoniot equations. The EOS incorporates the pressure-volume-energy relations needed for shock calculations by defining all the equilibrium states in a material and making it possible to determine any of the parameters as a function of one parameter. One such relationship between the shock velocity and particle velocity is represented by a linear relationship, known as the U_S-$U_{p,}$ for many materials and is determined empirically [1]:

$$U_S = C_0 + S \cdot U_P \tag{8}$$

Where C_0 is the bulk speed of sound in the material from equation 4 and S is an empirical parameter that changes based on the material. It is noteworthy that the linear relationship presented in equation 8 becomes invalid for materials undergoing a phase transition. Figure 2 shows experimentally measured curves for various materials where one can retrieve the values of the parameter S, knowing C_0.

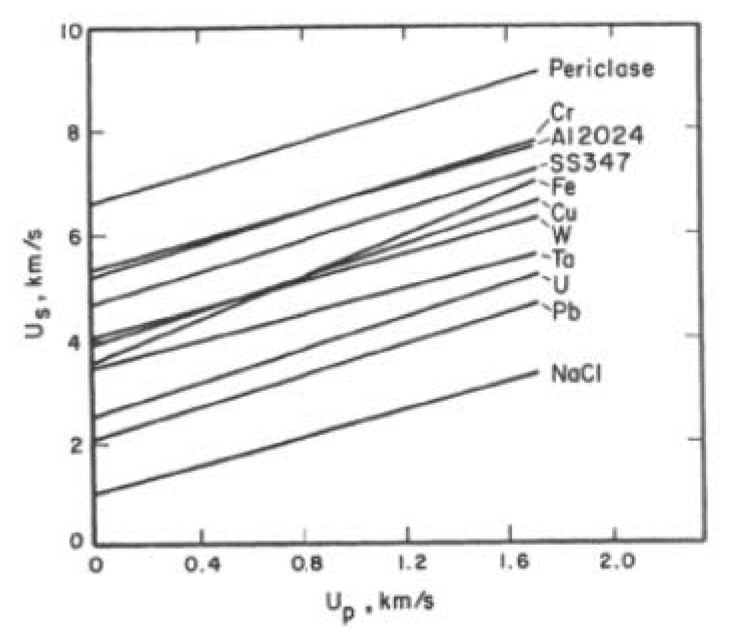

Figure 2: Experimentally measured EOS curves of U_S vs. U_P for various materials [1].

It was noted earlier that an elastic precursor wave precedes the shock wave front as it propagates through a medium. This elastic wave may interact with intrinsic and extrinsic microstructural defects ahead of the shock front that will alter the behavior of the shock wave, and in a polycrystalline material the most common defect that causes heterogeneity are GBs. Equations 3 and 4 assume that the material behaves isotropically, thus it is necessary to understand how anisotropy and heterogeneity affect the propagation of a shock wave in a polycrystalline material [31, 33]. The following section discusses the effects of anisotropy and heterogeneity has on shock wave propagation in a continuum.

2.2 Effects of Anisotropy on Shock Wave Propagation

Anisotropy is defined by the directional dependence of a property on the applied field [34], yielding different values of a physical property of a material when measured along different axes. Meyers [31] noted that the presence of anisotropy produces irregularities in the elastic precursor when it crosses a GB, thus affecting the rise time, which may be used to obtain information on dislocation dynamics. Other contributing factors include the difference in wave velocity with crystallographic direction of the grains, wave refraction at GBs, GB scattering, and scattering due to mode conversion between longitudinal and shear waves while traversing different grains [31].

Many materials of interest are polycrystalline in nature, which means that they are comprised of multiple grains through the material, where each grain is considered to be a homogenous single crystal with its own unique orientation in a three dimensional coordinate system. It is important to understand the wave interaction with defects in a material, such as GBs in a polycrystal, because when a longitudinal wave comes across an interface there are reflected and transmitted waves generated and the difference in elastic properties between adjacent grains governs the speed of these waves, particularly in the acoustic regime. It is deduced that the reflection and refraction occurs when an incident wave traverses a medium with variations in acoustic impedance, which is defined as the product of the elastic wave velocity (C_l from equation 3) and the density (ρ) and varies with crystallographic orientation in a material [1]. The surface plot of C_l^2 in Figure 3 shows how the acoustic impedance varies with crystallographic orientation in monocrystalline copper. This surface plot indicates grains have the lowest impedance along a <1 0 0> direction and the maximum impedance along a <1 1 1> direction. The highest mismatch of acoustic impedance in copper is thus at a GB between grains with shock waves parallel to <100> in one grain and <111> in the other. The resulting mismatch should lead to reflected and refracted waves that maximize strain concentrations at the GB, at least in the elastic regime [35]. The complexity of this impedance mismatch increases when dealing with the onset of localized strain from plasticity at a grain boundary, as the impedance will have, in general, different values with respect to the shock direction and the 3-D GB normal. Analysis becomes an exercise in determining which mismatch corresponds to the most strain localization at a boundary.

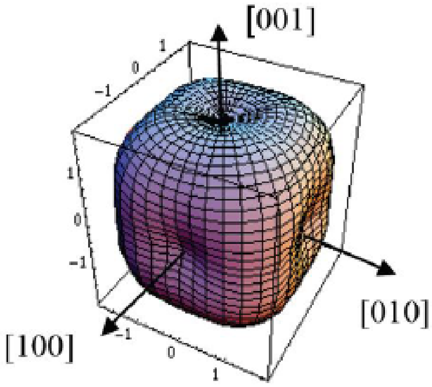

Figure 3: Surface plot of C_l^2 in copper varying with crystallographic orientation. The distance from the center to the surface is proportional to the longitudinal speed of sound along the direction defined by the joining vector [35].

The longitudinal velocities for elastic waves may be expressed as a function of the elastic constants for a cubic material, C_{11}, C_{12}, and C_{44}, along with the density, ρ. The longitudinal velocities for the three crystallographic orientations <100>, <110>, and <111> are expressed as:

$$U_{<100>} = \sqrt{\frac{C_{11}}{\rho}} \quad U_{<110>} = \sqrt{\frac{C_{11}+C_{12}+2C_{44}}{\rho}} \quad U_{<111>} = \sqrt{\frac{C_{11}+2C_{12}+4C_{44}}{\rho}} \qquad (9)$$

A combined experimental and computational effort to characterize the effect of material anisotropy on elastic shock propagation has been performed on laser-induced shock compressed NiAl bicrystals [33]. It was found that the shock arrived at the free surface of the grain with the higher speed of sound first. An accumulation of damage was found inside of the grain that the elastic wave was refracted into, which gives insight into understanding the scattering of elastic waves at interfaces and the resultant stress distributions. Understanding how shock wave scattering leads to stress concentrations at interfaces is important when dealing with multicrystalline and polycrystalline materials.

Since the basic governing physics behind shock wave propagation have been discussed, it is necessary to discuss how shock waves are sent through a material of interest experimentally. The common flyer-target plate impact method, in which a flyer plate is launched into a target sample, is reviewed in the next section.

2.3 Flyer Plate Impact Test

Planar impact is the most common method of producing shock waves in a material at high strain rates 10^5 s^{-1} and higher. This method consists of launching a flyer plate towards a target sample to get shock waves propagating through the target and flyer plates. It is important to maintain a one-dimensional loading condition for these experiments in order to ensure that the lateral strains (perpendicular to the shock direction) are negligible, i.e. uniaxial strain. The geometry of the experiment thus requires the flyer plate and target to be planar and parallel such that it is assumed that all points on the surfaces are contacted at the same time as discussed in Meyers [1]. In order to achieve uniaxial strain conditions one must simulate a semi-infinite body in the lateral direction so lateral release waves do not interfere with the longitudinal waves within the time frame of interest. This may be achieved by having disc-shaped targets with a width to thickness ratio of at least 10:1 [36].

The mechanism behind launching the flyer plate may be achieved from a variety of experimental techniques (i.e. gas expansion, laser irradiation, explosives, etc.) and should be chosen carefully to maximize the user’s ability to control the dynamic conditions of their experiment. Gas guns have been utilized extensively for plate impact experiments and depending on what gas is being compressed (usually helium) and the number of stages, one can achieve a wide range of velocities between 100 and 8000 m/s [1]. The use of laser drive systems to launch flyer plates has proven to induce strain rates up to 10^6 s^{-1}. Lasers also provide the ability to vary the pulse duration and magnitude for a wider range of dynamic test conditions, allow for more control over planarity of impact, and provide quicker test runs that enable more samples to be impacted for analysis. Using lasers to drive plates comes with an inherent limit in size for the launched plate unique to the equipment used, whereas gas guns are better fit at launching projectiles of varying sizes. This compromise of using smaller/thinner flyers is beneficial for studying incipient spall because this leads to shorter pulses and lower stresses. Figure 4 shows a flyer-plate impact assembly using a laser drive system, such as the TRIDENT at Los Alamos National Laboratories, with geometries typical of the samples studied in this work [20]. Lasers may also be used via direct drive to achieve strain rates up to 10^8 s^{-1} [37].

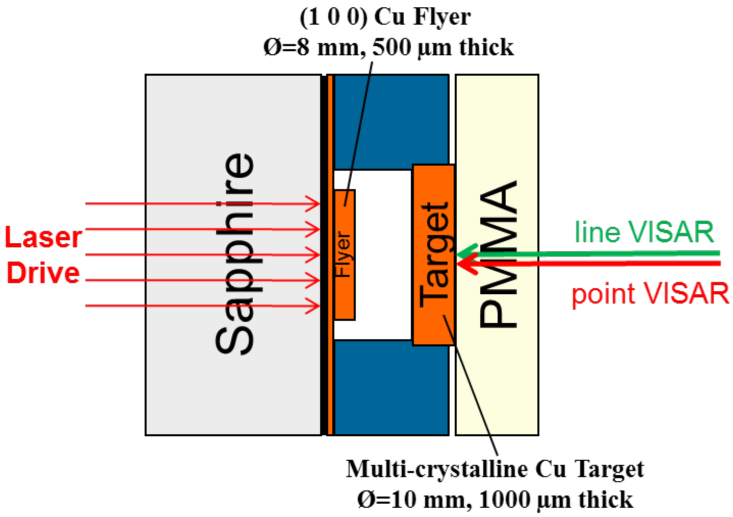

Figure 4: Experimental set-up for flyer-target impact testing using a laser drive with sample geometries typical of the work presented here.

A velocity interferometry system for any reflector (VISAR) is commonly used in dynamic experiments for measuring particle velocity on the non-impacted face of the target [37]. The measured velocity of the free surface (U_{fs}) is twice that of the actual particle velocity (U_p) due to the free surface boundary condition [1]. In some cases a material with lower shock impedance than that of the target (e.g., Plexiglas) is fixed against the non-impacted surface of the target. These materials act as windows and the velocimetry diagnostics record the particle velocity of the shock wave in the sample-window interface. The velocity profile at the diagnostic surface is recorded during the experiment via VISAR, and equations 5-8 may be applied to obtain the other shock parameters.

When a flyer plate impacts a target the shock wave propagates through the material as a compressive wave and upon reaching a free surface this wave reflects as a tensile release wave. The interactions of tensile release waves produced by the flyer and target free surfaces produce internal stresses when they coincide, resulting in localized strain, and, under the right conditions, eventual failure by spallation. Spall fracture is a complex process resulting from the nucleation, growth, and coalescence of voids produced when large tensile stresses are imposed for short durations. An important parameter for materials experiencing high strain rates is the spall strength of the material. The spall strength is more representative of the theoretical strength than the stress values obtainable from quasi-static loading experiments [38]. The next section is dedicated to explaining the phenomenon of spall damage.

2.4 Spall Damage

After a flyer plate hits a target there are two compressive shock waves generated, traveling in opposite directions from the plane of impact: one wave is sent through the target while the other travels back through the flyer plate. When these shock waves reach the free surface interfaces they reflect as release waves. These tensile release waves intersect at a plane within the target specimen and the superposition of these two waves results in a high magnitude tensile pulse. Spall damage occurs within a material when the tensile pulse produces a region of tensile stresses in excess of the threshold required for damage initiation [38], thus, if the magnitude of the tensile pulse approaches or exceeds the spall strength of the material then the ensuing plastic deformation may lead to ductile fracture via nucleation, growth, and coalescence of voids along the spall plane. The voids will continue to grow while the tensile stress remains above the threshold value, where the void growth is driven locally by the deviatoric component of the stress state and remotely by the overall hydrostatic component [2]. One simple way to increase the duration of the tensile pulse experimentally is to increase the thickness of the flyer plate. However, increasing the pulse duration is undesirable if one wishes to study the incipient stage of void nucleation as the voids may potentially reach a length scale similar to, or larger, than the grain size of the material [10,18-20,22,23]. Having voids that are approximately the same size of the grains in the material makes it difficult, if not impossible, to determine where damage sites nucleate. This will be discussed in more detail in section 2.5.

Figure 5 illustrates the distance-time diagram of the spall process for a flyer plate of thickness δ_1 impacting a target from the left at time t = 0. Note that δ_1 is greater than the thickness of the target. The stress profiles are given, showing when the material is in compression and tension at different distances and times. If the acoustic impedance of the flyer and target are equal and the target is twice the thickness of the flyer plate then the spall plane will geometrically be half-way through the target plate, which is ideal for analysis.

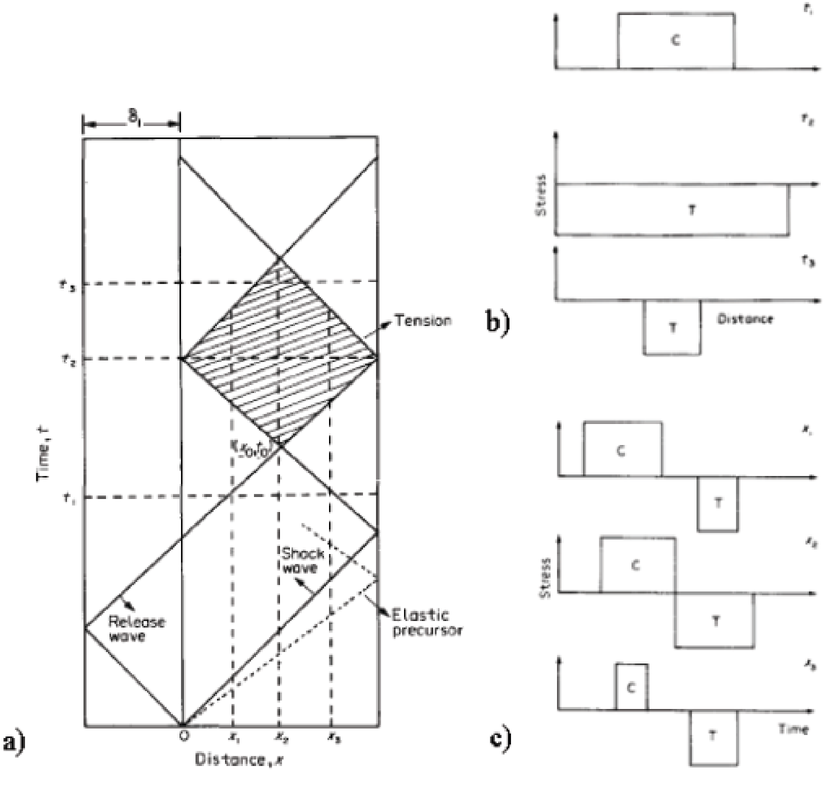

Figure 5: a) Distance-time plot (x – t) showing wave propagation in flyer and target after impact. b) Stress profiles over distance at given time intervals. c) Stress profiles over time at given distances. Note: for sub-figures b) and c), C stands for compression and T stands for tension. [2]

The spall process can be understood more in depth by analyzing the velocity-time plot recorded by the VISAR diagnostics. In Figure 6, the peak velocity of the compressive pulse (U_{max}) is from the initial propagation of the compressive wave accelerating the free-surface. The free-surface velocity just before the arrival of the spall pulse is U_{min}, and the dynamic measurement of the spall strength, called the pullback velocity, is defined as [18]:

$$\Delta U_{fs} = U_{max} - U_{min} \tag{9}$$

When the spall pulse arrives at U_{min} voids begin to nucleate, grow, and coalesce. This forms a new “free surface” within the target in the form of a spall plane from which there is a spall ringing from the compressive release waves reflecting back and forth between the free-surfaces and the spall plane, decreasing the tensile stresses [1]. This is not represented in figure 5, but it would be similar to a sinusoid with decaying amplitude for each subsequent period in time. The slope of the reloading curve after U_{min} characterizes the evolution of damage (growth); the steeper the slope, the more coalescence one would expect to find within the specimen [19].

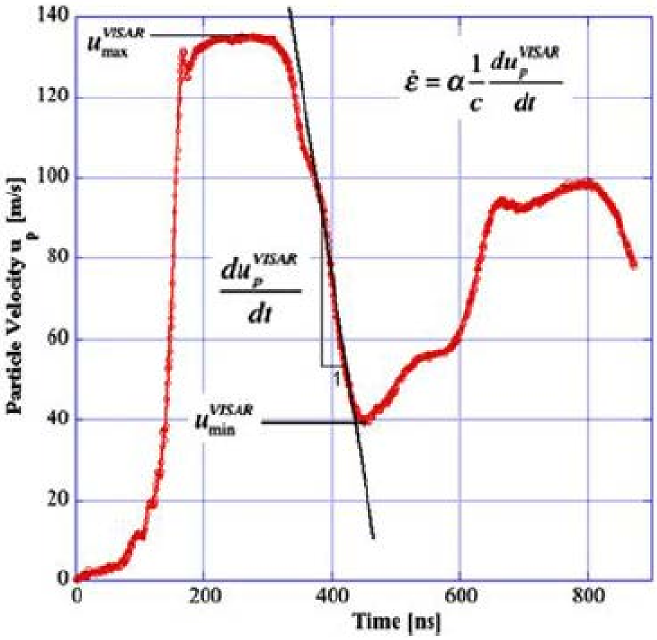

Figure 6: Typical free-surface velocity profile obtained from VISAR [20].

We can use equation 9 to find a general expression for the spall strength, which refers to the tensile stress just before spallation [38]:

$$\sigma_{spall} = \frac{1}{2}\rho_0 C_0 \Delta U_{fs} \tag{10}$$

This is an approximation that assumes the acoustic impedance terms (density ρ_0 and wave speed C_0) remain close to their original values. Romanchenko and Stepanov proposed a correction to equation 10 to account for the effects of the elastic-plastic deformation and spall plate thickness, which affects the wave profile, to determine the fracture stress [38]:

$$\sigma_{spall}^{*} = \frac{1}{2}\rho_0 C_0 \Delta U_{fs} \frac{1}{\left(1+\frac{C_l}{C_b}\right)} + \Delta\sigma \tag{11}$$

where, c_l and c_b are the longitudinal and bulk sound velocities, respectively, and

$$\Delta\sigma = \frac{1}{2}\frac{d\sigma}{dt}\bigg|_{C\_} h_s\left(\frac{1}{C_b} - \frac{1}{C_l}\right) \tag{12}$$

where $d\sigma/dt$ represents the stress gradient along the tail $C\_$ characteristic of the release wave, and h_s is the spall plate thickness.

Also, as noted in Figure 4, the strain rate ($\dot{\varepsilon}$) may be approximated from the VISAR profile as [20]:

$$\dot{\varepsilon} = \alpha\frac{1}{C_0}\frac{dU_{fs}}{dt} \tag{13}$$

where α is a constant stemming from the mismatch between materials at the diagnostic surface interface, which is 0.544 for copper and PMMA, and 0.5 for a free surface, for example.

Spall failure can be classified into three categories depending on the extent of damage, as shown in Figure 7 a-c. These categories are: 1) Incipient spall: when the spall first nucleates, which can be at preexisting defects, such as GBs, vacancies, pores, inclusions, etc. [3] 2) Intermediate spall: voids undergo growth due to plastic flow in the surrounding material and begin to coalesce. 3) Spall fracture: the voids fully coalesce to create a fracture surface, effectively shearing the target into two parts. For extreme cases the target may fracture completely, or separate into multiple parts.

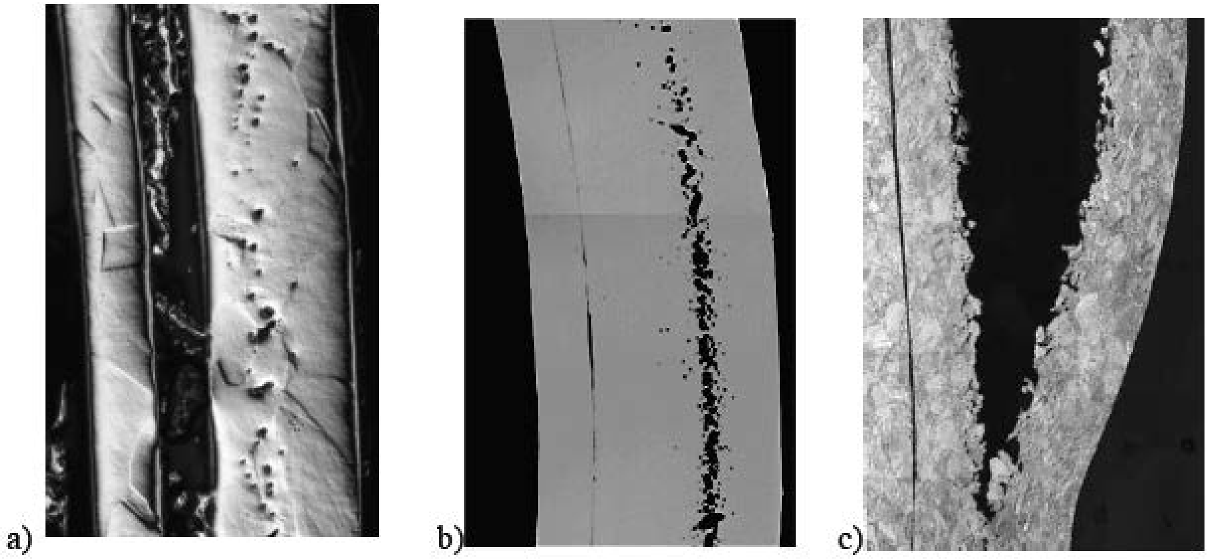

Figure 7: Examples of a) incipient spall, b) intermediate spall, and c) spall fracture [10, 16, 17].

The incipient stage of spall damage nucleation is the failure mode of interest in the research presented here. The principal motivation behind this work is to quantify and clarify the role microstructural features play in nucleating damage, including: grain size, crystallographic orientation, grain boundary strength, material anisotropy, Taylor factors, and plastic strain localization. The next section is dedicated to the effects the microstructure has on spall behavior and is the primary focus of this research.

2.5 Microstructural Effects on Spall Behavior

In order to fully understand where and how damage nucleates and grows within a material it is necessary to understand the effects that microstructure has on spall behavior. A fundamental starting point is to understand how the grain size influences the spall strength of a material, which has been the subject of numerous studies in the literature. It has been discovered that copper single crystals have higher spall strength than polycrystals under impact testing [5, 39]. From a typical Hall-Petch relationship one would expect the yield strength to increase with decreasing grain size in a polycrystal. However, this relationship does not translate well for determining the spall strength of a polycrystal contrary to older gas gun experiment reports [40]. It has been shown that smaller grain sizes correlate to a decrease in the spall strength of a material which is attributed to an increase in GB (defect) density [5]. Recent studies show that an increase of defects in a material, including GBs, inclusions, and second phase particles, result in a lower spall strength [1, 5, 41] and these defects often serve as nucleation sites for damage [10, 16, 40, 42].

Defects in a material have also been shown to affect the local damage mode present [10, 16, 40, 42]. Shock experiments using gas guns on polycrystalline copper suggest that the level of transgranular damage varies inversely with grain size [40, 42]. Buchar et al. [42] found that the spall strength was dependent on strain rate until a critical value that corresponds to the conversion from inter to transgranular damage modes. This increase in spall strength with increasing strain rates was found at rates as high as 10^7 s^{-1} by Fortov [43] and Moshe [41]. Recent findings from laser-driven flyer plate impact experiments in multicrystalline copper show that transgranular damage is present in areas where grain size is large compared to the sample thickness, and intergranular damage is present in areas of the sample with multiple smaller grains through the thickness [10, 16, 17].

The localization of spall damage at GBs has been studied by taking into consideration the material anisotropy in crystalline microstructures. Chen et al. [6] and Vignjevic et al. [11] conducted plate-impact experiments on rolled aluminum alloy (7010-T6) to study the effect of orientation on the spall strength. Vignjevic et al. [11] showed the HEL and spall strength are stronger in the longitudinal direction than the short transverse direction, and introduce the concept of strain rate sensitivity for the properties in the longitudinal direction. Minich et al. [5] tested impact experiments on 99.999% pure copper single crystals with three different orientations with respect to the shock direction and measured the corresponding spall strengths. It was found that the spall strengths in order from highest to lowest were: [1 0 0], [1 1 0], and [1 1 1].

Peralta et al. [10] introduced the concept of property mismatch causing heterogeneity in strain across a GB to explain the variation of spall behavior at GBs in response to dynamic loading. Incipient spall in copper was found to nucleate damage at and around GBs, especially triple points. Hashemian [17] studied the distribution of misorientation angles of damages boundaries in intermediately spalled copper multicrystals. High angle GBs (between 40° and 60°) localized damage more frequently, with the largest peak in the 60° twin range, shown in Figure 8. The majority of these damaged 60° twin boundaries were at the tips of terminated twins, or, incoherent boundaries. Incoherent boundaries have a much higher energy associated to them than coherent ∑3 twin boundaries since they do not typically fall along a (1 1 1) plane [44]. This high interfacial energy, coupled with geometrical discontinuities at the incoherent boundaries should promote intergranular damage, explaining for the high count in the 60° twin range.

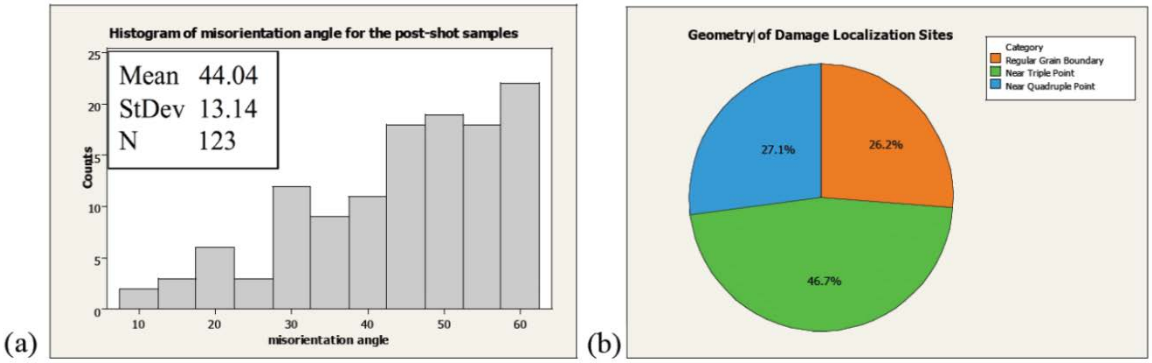

Figure 8: a) Histogram of misorientation angles for boundaries with damage in copper multicrystals. b) Fraction of damage sites according to grain connectivity. [17]

Collecting 2-D images and/or electron backscattering diffraction maps via serial sectioning is a common technique to achieve 3-D reconstructions of microstructures [18]. DeHoff [45] and Uchic et al. [46] both point out that no less than 10 sections per feature should be used to accurately represent its size and shape. Bingert et al. [47] performed 3-D reconstructions of spall damage in shocked tantalum samples and investigated the equivalent spherical void diameters and nearest neighbor distances between the voids. Significant variance was found when comparing the 2-D and 3-D data for nearest neighbor distance values between voids. Henrie [48] metallographically characterized impacted tantalum samples to quantify void statistics, mainly void area fraction, and suggested that 3-D data are required to get a more meaningful volume fraction as it was suspected that there was more radial connectivity than the 2-D sections revealed.

It is of interest to characterize adjacent grains with damage sites along the GB to elucidate what material characteristics at the microscale have the highest impact on localized damage nucleation in the microstructure. 3-D characterization of shocked tantalum samples was performed by Bingert et al. [47], and even though the voids had not coalesced, they had an average diameter 4 times larger than that of the average grain size. This creates ambiguity when trying to discern the original nucleation site within the microstructure.

In Wayne et al. [20], the authors analyze the intergranular damage in their polycrystalline copper samples to obtain statistics on the strength of GBs, and report that that the boundaries with the highest probability to contain spall damage were found to be in the 35-40° misorientation bin (Figure 9), with a tendency for damage at 60° boundaries to occur at the tips of terminated twins. However, these authors acknowledged that more work was needed to determine whether the intrinsic strength of the boundary or localized stress concentrations dominate in void nucleation. Escobedo et al. [15] claim that voids do not nucleate at special Σ1 and Σ3 boundaries, in agreement with the overall trends reported earlier by Wayne et al. [20], except for the tacit exclusion of the tips of annealing twins (terminated twins), which are incoherent ∑3 boundaries, from being considered "weak." Note that the experimental observations reported in [10, 20] of differences in spall damage nucleation between coherent and incoherent ∑3 boundaries are consistent with molecular dynamics (MD) modeling [29, 30], where no link between surface energy at GBs and the spall strength was found.

More recently, Escobedo et al. [14] compared shocked copper and tantalum specimens of varying microstructures to determine where damage exists relative to the GBs. Results once again showed that low coincidence, high angle GBs were preferred sites for damage, irrespective of grain size in copper, but dominant intergranular damage was found in tantalum.

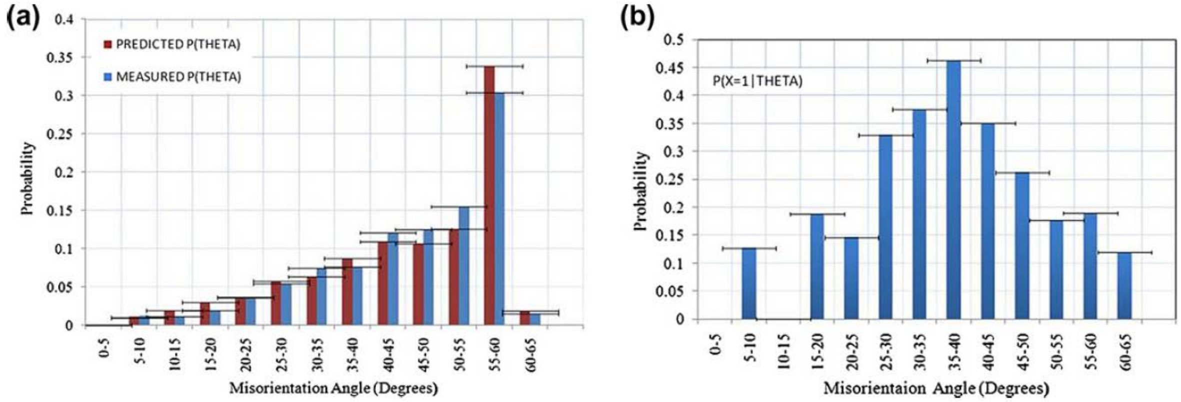

Figure 9: a) Predicted and measured probabilities for finding a given misorientation angle in the specimen. b) Probability of finding a misorientation angle θ with damage. [20]

It was reported by Escobedo et al. [15] that there was no clear correlation between void location and differences in either Taylor/Schmidt factors, or elastic stiffness across grain boundaries containing voids. Again, the issue here is that voids studied are the same size, or larger, than the apparent average grain size, making it impossible to determine at what boundary they nucleated. Further studies are needed as to the role of the Taylor factor on void nucleation and growth for both transgranular and intergranular damage. Spall studies on Cu single crystals have indicated low spall strength for <111> crystals, which have the highest Taylor factor, compared to <100> crystals, which have the lowest Taylor factor [5, 10]. These results are directly correlated to the number of available slip systems for the corresponding crystallographic directions, <100> having 8 and <111> having 6 in cubic materials. The lower availability of slip systems for higher Taylor factors lead to a stiffer response in a material undergoing tensile loading conditions. Additional data is required to gather enough evidence for statistical fits for the Taylor factor's role in damage nucleation and growth in spalled FCC metals.

Although 2-D studies are adequate for statistics on where damage is found within the microstructure, it is of interest to quantify the amount of inter- and transgranular damage present within a shock loaded sample. Three-dimensional data are needed to characterize precisely where voids are located within the microstructure because with 2-D data it cannot be determined if the damage studied is the beginning, middle, or tail of any one void, making it impossible to know where it may have nucleated and which direction it grew. The studies present in Escobedo et al. [15] analyze damage sites at GBs where the voids are approximately the same size as the surrounding microstructure, creating ambiguity when trying to discern the original nucleation site within the microstructure.

The work presented throughout this dissertation takes aim at drawing conclusions on where spall voids nucleate within shock loaded copper targets of varying microstructures and thermo-mechanical histories based on full 3-D characterization from various experimental analysis techniques. Statistics and 3-D data obtained from various characterization techniques (discussed in detail in Chapter 4) are needed in order to supply critical information about microstructural and physical effects from shock loading into computational modelling efforts to reliably predict the behavior of materials under high strain rate impacts without having to test in situ. The next section is dedicated to showing the progress of computational efforts to predict spall damage in a given microstructure based on experimental work and previous computational works.

2.6 Modeling Spall Damage

The experimental efforts of understanding the local effects of microstructure on the initiation and growth on spall damage has made significant progress, however, these results require modeling efforts in order to elucidate whether damage localization is due to early damage nucleation at weaker microstructural sites, due to fast growth kinetics after damage has nucleated, or a combination of both. A widely used constitutive theory for ductile rupture via void nucleation and growth has been developed by Gurson [49], which emphasizes the role of hydrostatic stress in plastic flow and void growth. Contributions by Tvergaard [50] and Needleman [51] were added to the Gurson model, now commonly referred to as the Gurson-Tvergaard-Needleman (GTN) damage model. The GTN framework is a homogenized isotropic matrix that was originally formed for triaxialities (T_x), i.e., the ratio of hydrostatic stress to equivalent von Mises stress, that are indicative of dominance of shear effects, e.g., uniaxial stress states that lead to $T_x \approx 1/3$. This makes GTN far from ideal for studies involving microstructural effects on spall damage since $T_x \approx 10\text{-}20$ during shock loading.

Tong and Ravichandran [52] concurred with the work by Ortiz and Molinari [53] that micro-inertial effects play an important role on void growth and incorporated strain rate dependence and inertial effects into the GTN model, which made it more suitable to model spall damage [52]. Recent modeling efforts have been focused on developing macroscopic continuum models using stochastic methods to predict damage nucleation [27, 54-56]; however, stochastic approaches such as these fail to account for plastic anisotropy resulting from crystallographic texture, and they do not account for the local deformation modes. Trumel et al [56] studied the elastic relaxation zones developed around a nucleated void, where it is only outside of these relaxed, or, inhibition, zones that new voids may be nucleated as seen in Figure 10. The nucleation and inhibition probabilities are linked to the local elastic and plastic properties of the material.

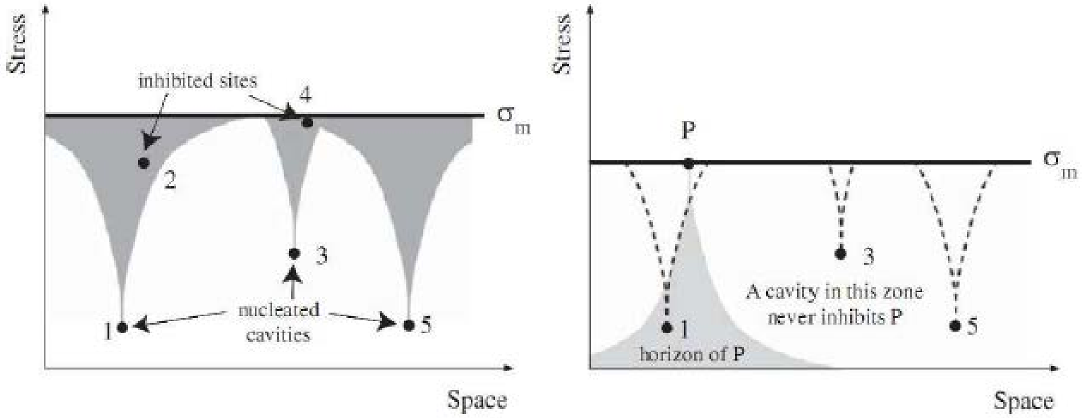

Figure 10: Inhibition and horizon concepts from [56]. Left: grey areas are relaxed zones where void nucleation is inhibited. Right: horizon of site P. Any active site in the grey zone inhibits further cavity nucleation at P.

Lebensohn et al [57] developed a fast Fourier transform (FFT) based approach to study the instantaneous viscoplastic response of voided polycrystalline solids and was extended to upon to further study the link between microstructure and void growth [57, 58]. The Taylor factor of grains in the polycrystalline matrix was used to show that voids tend to elongate and grow more along “soft” crystallographic directions, or, directions with a lower Taylor factor [58]. The FFT models used by Lebensohn et al [57, 58] lack micro-inertia effects, which is necessary to consider for void growth of dynamic processes and accounts explicitly for voids in the microstructure, which makes the approach impractical to scale up to the larger length scales needed for engineering models of spall damage.

Dynamic behavior in anisotropic materials has been modeled [59-62] and there exist several void nucleation and growth models to predict damage initiation and evolution in anisotropic materials [63, 64]. The work of Potirniche et al [63, 65] is of particular interest for studying potential effects of anisotropy on void growth and coalescence, as the work consists of studying not only single voids, but the equivalent plastic strain interactions between neighboring voids, which would lead to void coalescence. It is noteworthy that the voids studied in [65] were modeled as circular 2-D voids, whereas it is known that spall damage in a single crystal tends to take the shape of octahedrons [66]. Clayton and coworkers developed crystalline elasto-plasticity models to study high strain rate behavior in multiphase polycrystalline metals via implementation of cohesive zone techniques to represent grain and phase boundaries, which showed that interfacial properties influence spall behavior prediction more than grain shapes and initial orientations [67, 68].

Traiviratana et al [69] used molecular dynamics simulations in mono- and bicrystalline copper subjected to tensile uniaxial strains, revealing that nucleation of voids is favored at slip planes making an angle of 45° with the void surface, maximizing shear stresses, in agreement with the recent 3-D continuum mechanics studies of Krishnan et al [19, 24]. Furthermore, MD simulations of spall behavior at coherent and incoherent Σ3 GBs also show nucleation at and beside GBs [29, 30], consistent with the behavior reported in [10, 20, 22-24]. Research in the nucleation and growth of voids using atomistic models is encouraging [29, 30, 69-73], as additional information at these specialized time and length scales provide insight as to which micromechanics are needed in continuum models moving forward.

Recently Krishnan et al [19, 24] used a modified GTN crystal plasticity framework to perform 3-D finite element simulations of individual GBs showing the presence of a GB-affected zone, where strain concentration occurs to one side of a GB due to the presence of the boundary itself, with results strongly correlating to damage sites studied experimentally in shock loaded copper multicrystals. Taylor factor mismatch is a crystallographic focus of this work, showing that intergranular damage grows perpendicular to the boundary and into the adjacent grain with the lower Taylor factor. One unique aspect of this work is the incorporation of the physical GB normal into the 3-D finite element model, which changes the stress and strain states at and near any given GB with a varying inclination with respect to the shock direction. The GTN based model used by Krishnan et al [19, 24] contains a scalar damage parameter that does not account for void growth and coalescence along preferential directions, however, it has been shown experimentally by Escobedo et al [14] that damage nucleation of voids in BCC materials tend to follow slip traces.

Experimental data coupled with simulations have been used to determine the effects the Taylor factor plays in damage nucleation, growth, and coalescence in copper multicrystals [18, 19]. Simulations by K. Krishnan [19] reveal that a high Taylor factor mismatch along the crystallographic normal drives the nucleation of the voids at the GB, while the presence of a low Taylor factor along the shock direction promotes void growth perpendicular to the GB and may also lead to transgranular void nucleation, growth, and coalescence. Figure 11 shows results of the equivalent plastic strain and void volume fraction from the simulations and the corresponding microstructures. It was found by K. Krishnan in these models, as well as others, [19] that strain localization appeared next to GBs that nucleated damage, indicating a possible GB affected zone for which dislocation emission controls the nucleation and subsequent plasticity driven growth of voids [71].

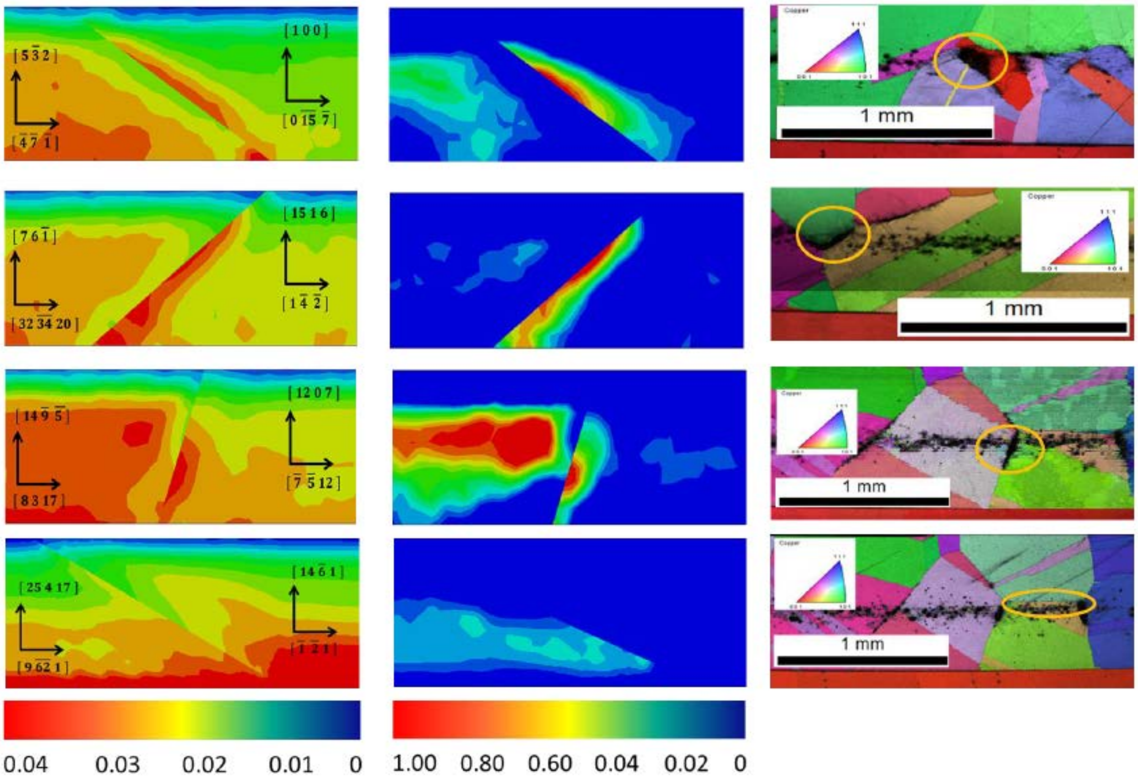

Figure 11: Contour plots of equivalent plastic strain (left), void volume fraction (center), and corresponding EBSD scan images of the damage sites (right) for damage sites (top to bottom): high mismatches in Taylor factors (TF) along the shock direction and GB normal, moderate values for both TF mismatches, low TF mismatch along the shock direction and high along the GB normal, and no damage at a site with low TF mismatches along the shock direction and GB normal. [19]

Despite significant progress in both experimental and simulation work involving the initiation and growth of spall damage based on the local microstructural effects, there does not yet exist a continuum mechanics crystal plasticity framework accounting for microinertia that captures anisotropic effects of the material on void nucleation, growth, and coalescence for both quasi-static and shock loading deformation modes. This is something that the modelling community is working towards, but additional experimental data on localized plastic deformation (strain fields), real 3-D geometry of voids, and additional statistics linking damage nucleation to global and local microstructural characteristics are needed to get there. Recall that the literature is lacking in models that take into account the physical geometry of voids nucleated in single crystals [66], which is important to correctly account for anisotropy effects as the shape of the void will affect the stress and strain concentrations upon loading. A two part study of a modified, homogenized GTN yield criterion for porous ductile solids containing arbitrary ellipsoidal voids was performed by Madou and Leblond [74, 75] using a velocity field analysis. In the work presented here, 3-D studies aim to capture the shape of individual and coalesced voids on shocked copper samples of varying thermo-mechanical histories to add knowledge as to what damage modes (intergranular vs. transgranular) are most probable for each microstructure.

The chapter so far has introduced the concepts of shock loading and spall damage and how both are affected by global and local microstructures. The broad investigation of the literature from both experimental and computational efforts gives insight into what needs to be added to the existing knowledge pool to fully understand how spall damage nucleates, grows, and coalesces within FCC metals of varying microstructures. The primary objective of this research work is to provide a comprehensive 3-D study of spall damage in FCC metals, focusing on the impact global and local microstructures have on the damage mode and shape of nucleated voids and incorporating statistics to determine the weak links within the material.

3. OBJECTIVES

It has been shown that damage nucleation in shock loaded metal is dependent on microstructural effects such as GB misorientation, triple junctions, etc. Comprehensive 3-D reconstructions of both the microstructure and spall damage are needed to determine where damage nucleates and how it evolves through the microstructure, which cannot be verified from 2-D cross-sections. Comprehensive 3-D reconstructions also aide in determining the 5 parameters to fully characterize a GB; the GB physical normal at damaged sites was previously not attainable from 2-D studies as the grains have curvature through the thickness. A 3-D approach to microstructural analysis of shocked copper poly- and multicrystals to provide fundamental scientific information to modeling efforts is the driving force behind this research and aims to meet the following objectives:

1. Gather 2-D statistical data on GB strength in incipient spalled copper polycrystals of varying processing conditions and grain sizes to determine the preferred misorientations for damage nucleation, if any.
    - The crystallographic features of the damaged and undamaged GBs within a consistently defined spall zone will be studied to understand their effect on damage nucleation while taking into account texture in the material.
2. Analyze the distribution and shapes of voids from 3-D X-ray tomography renderings of the spall plane as a nondestructive technique to determine the damage modes present in each microstructure.

    - Use visual inspection and comparisons of void distributions and volumetric data to make a hypothesis for the damage modes present in each microstructure.
    - Develop methods for fitting the shapes of individual voids to that of ellipsoids to determine the amount of intergranular, transgranular, or coalesced damage present within each microstructure.
    - Draw conclusions about the effects global microstructure have on spall damage mode preference from the 2-D and 3-D studies of shocked polycrystals.

3. Investigate large volume damage sites at GBs in spalled copper multicrystals to determine what parameters make these sites "weak links" in the microstructure. 3-D reconstructions of the damage and microstructure enable for full characterization of the damaged GBs. Additional 3-D data needs to be acquired to supplement and expand upon the information gathered from previously consecutive sectioned samples [18].
    - Misorientations across GBs with damage will be compared to the findings of the 2-D statistical analysis of copper polycrystals to identify intrinsic GB strengths. Special boundaries such as CSLs, {111} Σ3 twins, and incoherent twins will be discussed on a case by case basis.
    - Taylor factors provide for insight into the availability of slip systems for a given direction, which can be related to how a material yields under a specified stress state. The Taylor factors and mismatches for adjacent

  grains containing damage at their boundary will be analyzed along the shock direction and crystallographic GB normal to gain insight on the mechanisms driving void nucleation and growth at and around GBs.
  - The angle between the shock direction and the GB normal will be investigated and compared to void volume to determine if the shear component of the overall stress state plays an important role in nucleating damage at a GB.

4. FIB milling around damaged sites in shocked multicrystals is to be coupled with EBSD in order to do partial to complete 3-D reconstructions of individual voids and their surrounding microstructure (intergranular and transgranular voids are to be analyzed). Analyzing the lattice rotation around the voids will capture the nature of the plasticity present at the damage sites and how far and what crystallographic directions the localized plastic zones extend from the voids.
   - Studying the plastic deformation around intergranular and transgranular voids will provide more insight as to which mechanisms are responsible for void nucleation and which drive void growth and will be compared to previous studies on Taylor factors, boundary strengths, and anisotropy to draw conclusions.
   - 3-D reconstructions of the microstructure around intergranular and transgranular voids will provide new information on the size and structure of inhibition zones around voids. Trumel et. al [44] explains the phenomenon of inhibition zones and how nucleated voids prevent new

    voids from forming adjacent to them due to interaction with the release wave coming from the newly formed void surface.

5. Strain localization beside a GB has been observed in simulations by Krishnan [19] to possibly lead to damage nucleation beside the affected GB. Fabrication of uniform surface perturbations on the diagnostic side of shcok loaded copper poly- and multicrystalline target plates allow for strain localization at GBs to be analyzed away from the spall plane and anisotropy may affect yield stresses.
    - Photolithography and chemical etching processes will be developed in order to fabricate surface perturbations with varying wavelengths on the order of micrometers.
    - Impact tests will be performed on the target plates and changes in amplitude of the surface perturbations for grains of varying orientations gain insight into anisotropic hardening of the material.
    - Sectioning of the impacted targets will be done and the cross-sections will be polished and microstructural characterization will be conducted near the perturbation surface and in the spall plane, if any. If there is a spall plane, it is of interest to see how the perturbations may affect the size and position of the voids.

4. EXPERIMENTAL PROCEDURES

4.1 Flyer Plate Impact

Dynamic testing was conducted at the TRIDENT facility at Los Alamos National Laboratory (LANL). For reemphasis, a laser-driven plate impact experiment is ideal for studying incipient stages of void nucleation and minimizing growth, due to the shorter tensile pulse than with similar gas gun experiments, as a result of thinner flyer plates. Trident contains a Nd:glass laser that operates at a fundamental wavelength of 1054nm and produces a homogenous drive for uniform acceleration of the flyer. A diagram of the TRIDENT facility setup is shown in Figure 12. A sapphire substrate was coated with a vapor-deposited ablative layer of C, Al and Al_2O_3, which were contained under a thin shield of Cu foil. Upon laser beam illumination of the sapphire's free surface, the vaporization of the ablative layer created a high-pressure mixture of plasma and hot gases that launch the flyer disk towards the target plate as it expands. The flyer, glued to the thin Cu foil, was launched at velocities ranging from 100-400 m/s. The target sample rested flush against a 9.53mm thick PMMA (Plexiglass) window on the diagnostic side through which the velocity history could be recorded using point and line VISARs. Standard hydrodynamic approximations [1, 17, 20, 76] were used in order to account for the effects of the PMMA window on maximum pressure (P_{max}), the amplitude of tensile pulse reflected from the window (σ_{refl}), spall stress (σ_{spall}), and strain rate ($\dot{\varepsilon}$), which will be further explored in the next section.

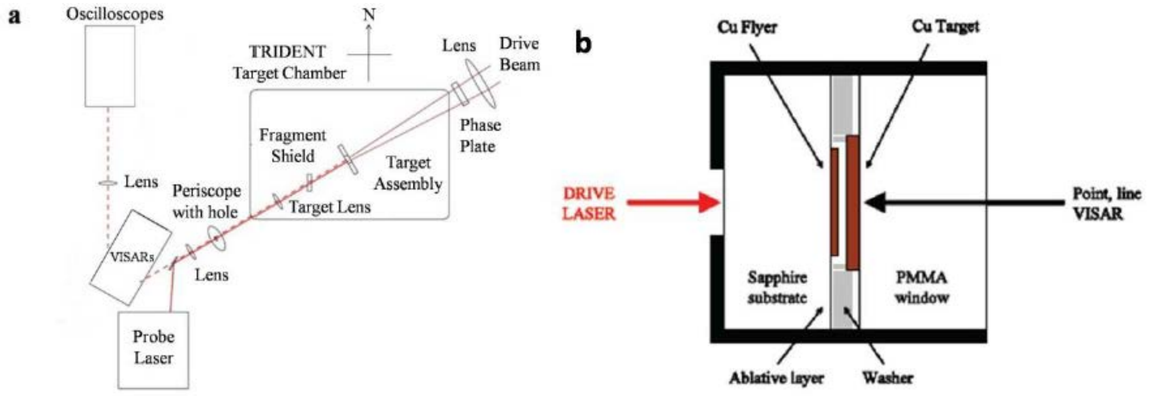

Figure 12: Flyer plate impact experimental setup; a) Schematic of test setup at LANL’s Trident laser facility. b) Side view of a shot assembly for impact testing.

4.2 Velocimetry Diagnostics

Diagnostics for the experiments included two point VISARs, which were used to record the velocity history of the target-window interface during impact. Line VISAR and transient imaging displacement interferometry (TIDI) were used when additional diagnostics were required. For each point VISAR a velocity over time through a series of fringes were recorded with a streak camera. Two different fringe constants were used (one for each point VISAR) in order to capture both high and low resolution fringes, which is helpful in cases where a fringe shift of 2π or greater exists, as it becomes difficult to interpret how many shifts occurred from the data. The center regions of the target surface were probed by the two point VISARs. For more detail of the laser, shot assembly, and diagnostic techniques utilized at TRIDENT refer to Luo et al. [37] and Dolan [77].

Parameters describing material behavior under shock loading are obtained from the velocity profiles at the diagnostic surface obtained from the VISAR for each experiment. The Rankine-Hugoniot equations (5-7) and the EOS (8) were used along with the VISAR data to calculate the shock conditions for the samples analyzed in this work. The particle velocity of the target specimen (U_p^{Target}) was obtained from the particle velocity measured at the target-window interface (U_p^{VISAR}), accounting for the presence of the PMMA window [10]:

$$\frac{U_p^{Target}}{U_p^{VISAR}} = \left(\frac{\rho_0^{Cu} + \rho_0^{PMMA} U_S^{PMMA}}{2\rho_0^{Cu} U_S^{Cu}}\right) \tag{15}$$

Where, ρ_0 and U_S correspond to the densities and shock velocities for each material. The densities used for analysis were: ρ_0^{Cu}= 8.930 mg/m^3 and ρ_0^{PMMA}= 1.182 mg/m^3. Approximating shock velocities via the bulk speed of sound (U_p= 0 at zero pressure), $U_S^{Cu} \approx C_0^{Cu}$ = 3.94 km/s, and $U_S^{PMMA} \approx C_0^{PMMA}$ = 2.6 km/s results in a constant velocity ratio of U_p^{Target} = 0.544U_p^{VISAR}.

The ratio found in (15) can be combined with the Rankine-Hugoniot equation for conservation of momentum (6) to calculate the pressure of the shock, or, more accurately, the approximation of the stress along the shock direction for high triaxiality conditions:

$$P_{max}^{Target} = \rho_0^{Cu} U_S^{Cu} U_{p,max}^{Cu} = 0.544 \rho_0^{Cu} U_S^{Cu} U_p^{VISAR} \tag{16}$$

Where,

$$U_S^{Cu} = C_0 + S \cdot U_{p,max}^{Cu} = C_0 + S(0.544 \cdot U_{max}^{VISAR}) \tag{17}$$

is found from the EOS in (8) and C_0 = 3.94 km/s and S = 1.49 for copper.

The spall strength from (10) must be corrected for the presence of the PMMA window due to the reduction in magnitude of the release wave from the propagation of the shock front through the window. The correction has been proposed by Grady and Kipp [76]:

$$\sigma_{spall} = \frac{1}{2}(\rho_0^{Cu}U_S^{Cu} - \rho_0^{PMMA}U_S^{PMMA})U_{max}^{VISAR} - \frac{1}{2}(\rho_0^{Cu}U_S^{Cu} + \rho_0^{PMMA}U_S^{PMMA})U_{min}^{VISAR} \quad (18)$$

Using Poisson's ratio for copper, ν^{Cu}= 0.33. Lastly, the strain rate upon release can be estimated within the acoustic approximation for the velocity profile [37]:

$$\dot{\varepsilon} \approx \frac{1}{C_0^{Cu}}\left(\frac{dU_p^{Target}}{dt}\right) \approx \frac{0.544}{C_0^{Cu}}\left(\frac{U_{max}^{VISAR}-U_{min}^{VISAR}}{t_{U_{max}^{VISAR}}-t_{U_{min}^{VISAR}}}\right) \quad (19)$$

These parameters are calculated for each sample analyzed throughout this body of work. Methods used for sample preparation for both flyer and target plates used for testing are described in the next few sections.

4.3 Material Selection

Copper was selected as the material for all samples analyzed in this work as a representative face-centered cubic (FCC) structure, due to high anisotropy factor (A = 3.3) for its elastic properties, high ductility, and relatively low strength, making it an ideal material for dynamic testing under varying conditions. Copper is also a readily available material that is easily machinable and straightforward to characterize. All samples were prepared from a rolled plate of high-purity Hitachi copper (99.995%, half-hard, nominal cold reduction of 21%) with an average grain size of 150 μm.

4.4 Flyer Plate Fabrication

For all flyer plates, cylindrical rods 8 mm in diameter were cut from high-purity copper plates via electrical discharge machining (EDM) through the thickness of the plates. Flyer plates were then sectioned via EDM at a thickness of 700-750 μm to allow for mechanical polishing to remove the ~100 μm damage layer produced from EDM on each face. Polycrystalline flyers were then polished within ±10% of the desired 500 μm thickness while maintaining a parallel face tolerance of approximately 0.05°. Each side was polished with 600, 800, 1200 grit SiC paper, followed by 5 μm alumina powder and deionized water slurry, then finished with 0.05 μm colloidal silica suspension. An Allied High Tech Multiprep^{TM} was used for this polishing procedure. Figure 13 shows the process for manufacturing flyer and target plates from raw stock material, the latter of which are discussed in the next section.

Figure 13: Clockwise from top left: raw plate of half-hard copper, EDM manufacturing of cylinders of appropriate diameters for flyers and targets from raw material, bored out cylinders, EDM discs from bored cylinders, discs awaiting polishing on a sample holder that fits onto the polishing machine.

A modified Bridgman technique was used to fabricate single crystal flyers oriented along the [100] direction, as studies have shown this to be the orientation with the highest spall strength [5] and the high symmetry orientation will sustain a pure longitudinal shock wave. Rod stock was used to grow single crystals close to the desired orientation, then each crystal was mounted in a goniometer and Laue backscatter X-ray diffraction was used to determine the actual orientation. Necessary rotations were made in the goniometer to achieve the desired orientation and the EDM was used again to cut the flyers into discs 8 mm in diameter and 700 µm thick. The flyers underwent the same polishing procedure as the polycrystalline flyers, again achieving ±10% of the desired 500 µm thickness while maintaining a parallel face tolerance of approximately 0.05°.

4.5 Target Plate Fabrication

For all target samples in this work, 10 mm diameter cylindrical rods were extracted through the thickness of high-purity copper plates via EDM. Targets were then sectioned via EDM at a thickness of 1.2 mm to allow for mechanical polishing to remove the ~100 µm damage layer produced from EDM on each face. Polycrystalline targets were then polished to ±10% of the desired 1 mm thickness while maintaining a parallel face tolerance of approximately 0.05°, then underwent the same polishing procedure used for the flyer plates (600 SiC grit paper through colloidal silica finish), which is depicted in Figure 13.

Target samples underwent one of four post-fabrication thermal processing procedures:

- No change to target samples, stored in membrane boxes until use. These targets are called “as-received” (AR) specimens since their original 21% nominal cold-reduced microstructures were preserved. Average grain size of ~150 µm for AR targets.

- Target samples underwent a heat treatment (HT) process at 473 K (200 Celsius) for 1 hour under inert atmosphere. Plastic pre-strain was greatly reduced and resulted in average grain sizes of ~120 μm.
- Target samples underwent a full recrystallization (FR) process at 873 K (600 Celsius) for 1 hour under inert atmosphere. Plastic pre-strain was greatly reduced and grain recrystallized, resulting in average grain sizes of ~50 μm.
- Target samples underwent heat treatment to achieve quasi-columnar multicrystalline specimens at 1173 K (900 Celsius) for four hours either under vacuum in a quartz tube ampoule or under inert atmosphere. Plastic pre-strain was greatly reduced and fast grain growth resulted in average grain sizes of ~450 μm.

Targets with various thermo-mechanical histories are desirable to observe how the microstructure affects the transition from transgranular to intergranular damage modes. Figure 14 shows representative microstructures for all four thermo-mechanical processing conditions investigated in this work. Cross sectioning and comparing these samples for post-shot analysis provided for many damage localization sites for each section, allowing for quantitative 2-D statistics of microstructural parameters such as misorientation angle, the Taylor factor, and crystallography of grains surrounding damage sites. Polycrystalline targets provide for more data points when collecting intergranular damage statistics since the smaller grain size increased the number of “weak sites” available for damage nucleation and promotes intergranular damage [12], whereas the multicrystalline targets gave insight into boundaries and microstructural features that are “weak links” by investigating the presence of large volume damage sites at grain boundaries. These “weak links” were also investigated in modeling efforts by Krishnan et al. [19, 24].

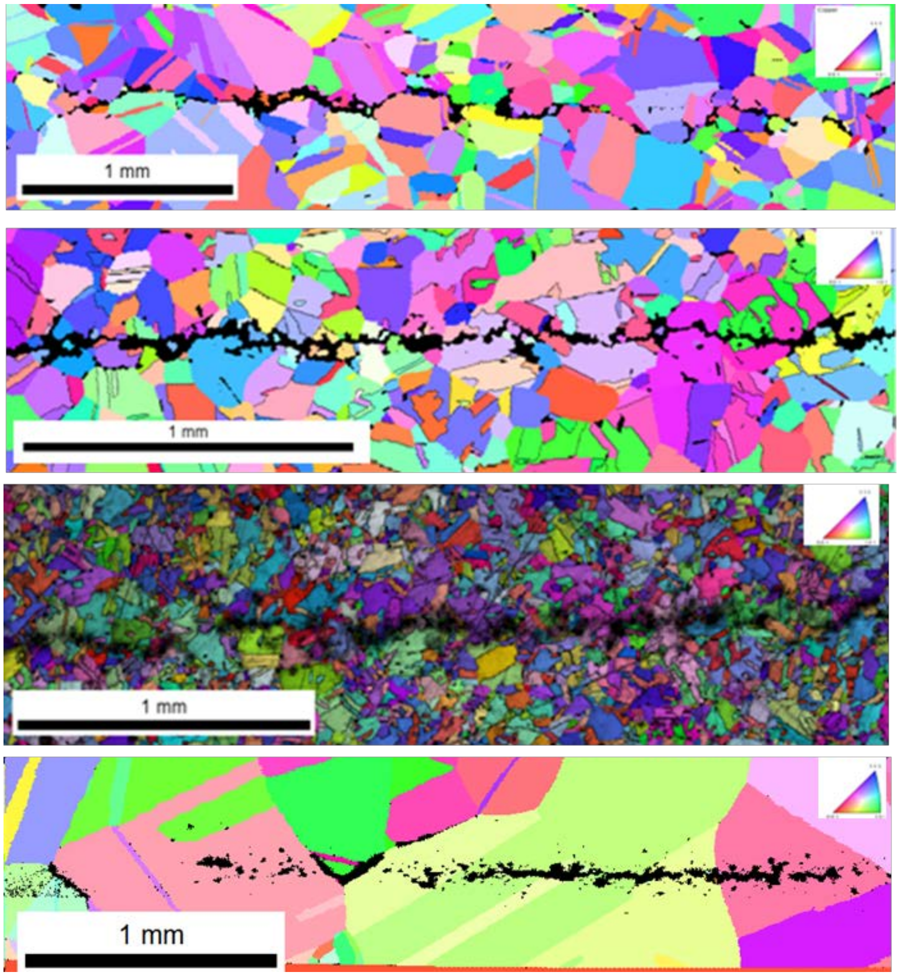

Figure 14: EBSD maps of shock loaded polycrystals, from top to bottom: AR Cu, HT Cu, FR Cu, and MC Cu. All EBSD maps show a single average orientation per grain, ±5°, with colors representative of the standard inverse pole figure (IPF) triangle.

4.6 Target Plate Fabrication with Surface Perturbations

A fabrication process was developed to use photolithography to apply a periodic perturbation on the diagnostic surfaces of target disks. A square wave with periods, or, “wavelengths”, ranging from 30 to 150 μm were created on the diagnostic surfaces of target discs via a columnar photomask pattern. Photolithography processes took place at ASU’s Center for Solid State Electronics Research (CSSER). AZ-4330 photoresist was applied to an optically flat AR Cu targets 10mm in diameter via spin coating to reach a uniform height of approximately 4μm, per the spin recipe shown in Table 1.

Table 1: Spin recipe for AZ-4330 photoresist on Cu target specimens.

Ramp Time (s)	RPM	Spin Time (s)
1	500	10
3	4500	30
3	0	N/A

Photomasks containing patterns of alternating transparent and dark columns of varying wavelengths were used to create the necessary. For cost-efficiency purposes, each photomask plate contained four columnar patterned sections, each with a different wavelength, as shown in Figure 15.

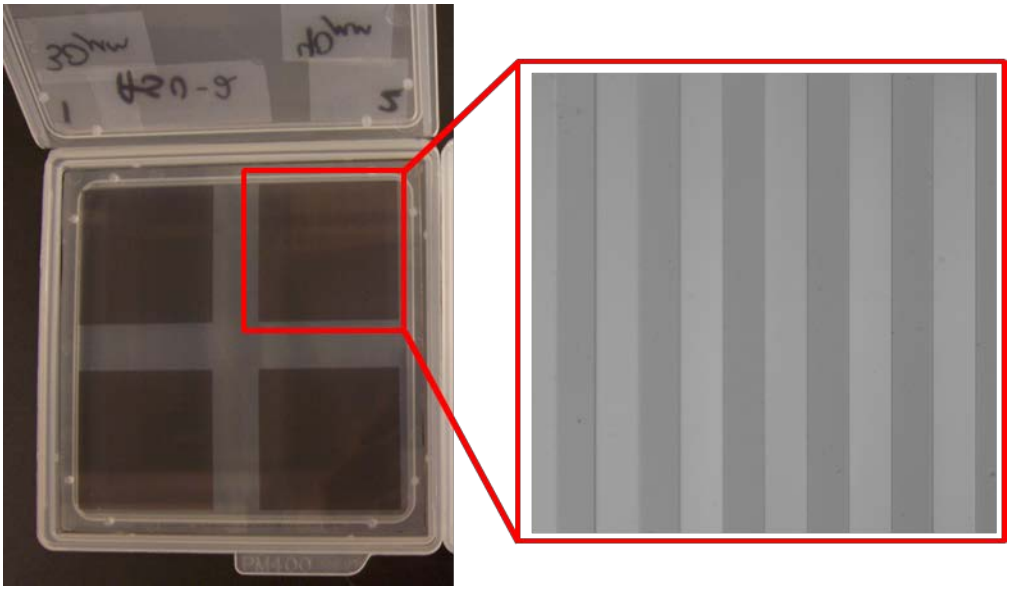

Figure 15: Glass photomask with four columnar grid patterns of various spacing (left) and a 20x objective lens optical image of a columnar pattern (right).

An OAI 808 front/backside aligner (350W mercury lamp) was used for the UV light exposure step of the photolithography process. Frontside alignment was used; meaning the photomask's etched side containing the pattern was in contact with the specimen. Frontside alignment minimizes any UV light bending around the photomask pattern, preserving the geometry of the pattern as best as possible. Gap calibration between the sample and the photomask was done for each individual specimen to maintain the highest precision possible throughout the manufacturing process. Exposure time of the sample to the UV light depended on the thickness of the photoresist layer, the wavelength of the pattern, sample material/composition, and the intensity of the OAI lamp at the time of exposure. It was found that over-exposure leads to non-uniform patterns when developed and 13-20 seconds was found to be the preferred range of exposure time for the Cu targets. Samples were transferred to a base wet bench immediately after exposure and were developed in AZ 300 MIF developer for 120 to 140 seconds, rinsed with deionized (DI) water, and dried with N_2 gas. Then they were examined under an optical microscope with a light filter after 120 seconds of develop time to ensure the photoresist was entirely removed from the exposed columns in the mask pattern. If residual photoresist was present the sample was placed back into the developer for 10 second increments until fully removed. After this step the samples were taken out of the clean room, exposed to full-spectrum light, and prepared for chemical etching. Figure 16 illustrates the photolithography process described here.

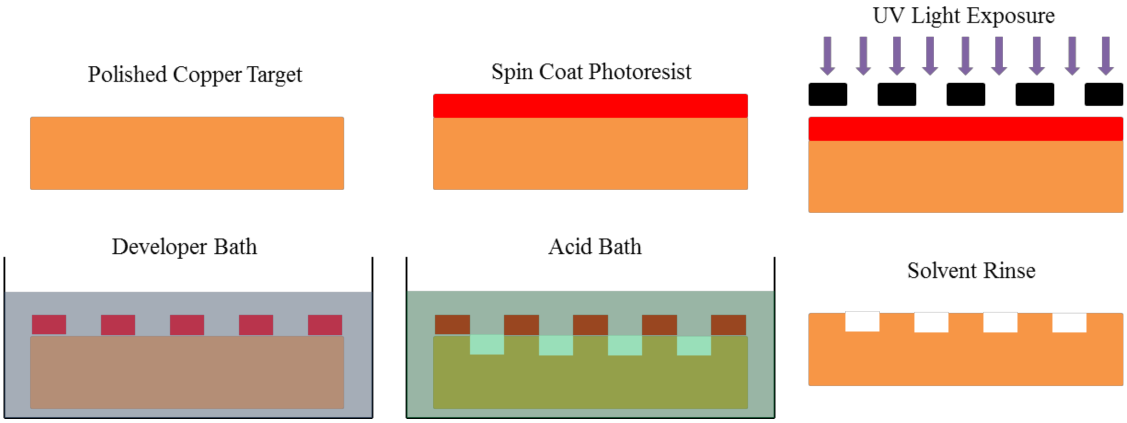

Figure 16: The photolithography process of etching features onto the surface of a flat substrate, sequenced left to right, top to bottom.

After completing the clean room processes, the target specimens have a ~4μm tall step function pattern of photoresist and Cu on the diagnostic side. The samples were taken for optical profilometry on a ZeScope at ASU's LeRoy Eyring Center for Solid State Sciences to determine the height of the photoresist. Chemical etching was used to remove material from the exposed Cu regions such that a step function of a specified height was present after the removal of the photoresist. The sides and impact side of the target specimens were painted with nail polish to protect these surfaces from chemical etching. A chemical etchant composed of 30% FeCl, 3-4% HCl, and DI water was used to create the step function. The etch rate of this chemical is known to be 3.9μm/minute; however, it was found that when the chemical etchant is agitated via electro-magnetic stirring or vigorous manual movement of the sample held with a plastic or carbon coated stainless steel tweezers, the removal rate was found to be 8-9μm/minute, approximately double the known 3.9μm/minute rate. After etching, the sample is rinsed in a 4% HCl and DI water solution, followed by DI water rinse and dried with compressed air.

Optical profilometry was performed a second time to determine the new depth and profile shape of the etched Cu troughs to photoresist peaks and compared to the original Cu to photoresist heights to determine the exact depth of the Cu square wave before removal of the photoresist. If the depths were too shallow then additional etching was done until the desired depth was obtained. Once the desired depth of the Cu steps was achieved, the sample was rinsed in acetone to remove the photoresist and nail polish. Figure 17 shows a top-down optical image of a Cu target with the final square wave etched on the diagnostic surface. Notice that the etched regions clearly show grains with some loss of optical reflection and added surface roughness of 100nm and less, while the regions covered by photoresist remain optically smooth from polishing procedures.

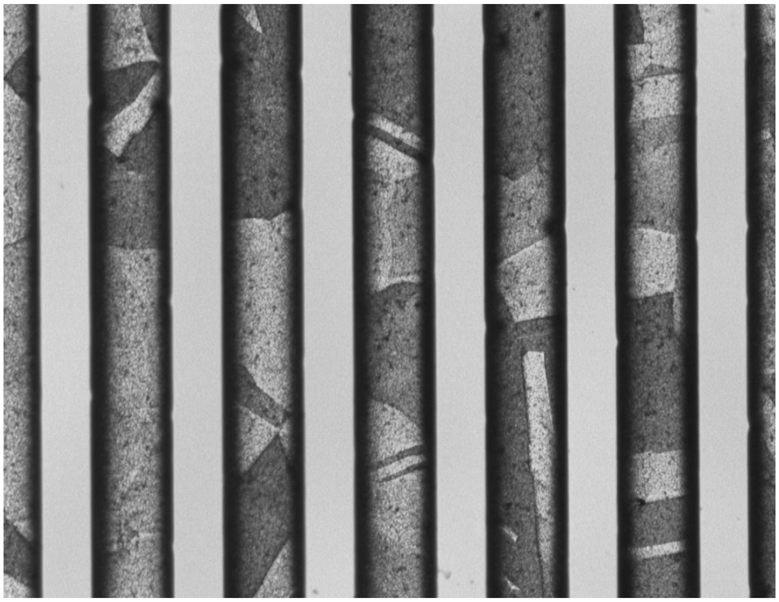

Figure 17: Etched step function on the diagnostic side of a PC Cu target specimen.

Finally, all samples underwent heat treatment under inert gas atmosphere at 473 K (200 Celcius) for 1 hour to aide in surface roughness reduction from etching and to remove pre-existing plastic deformation. Select samples were heat treated under inert gas atmosphere at 1173 K (900 Celcius) for 4 hours to grow quasi-columnar to columnar grains. These MC specimens were then scanned using EBSD to gather information about the orientation of the grains at the diagnostic surface before impact testing. Optical profilometry was done for all samples after heat treatment to get the final geometry of the surface topography before testing. A typical square wave profile is shown in Figure 18. The next section presents an additional manufacturing process that was developed to aide with in-situ laser diagnostics of rippled targets.

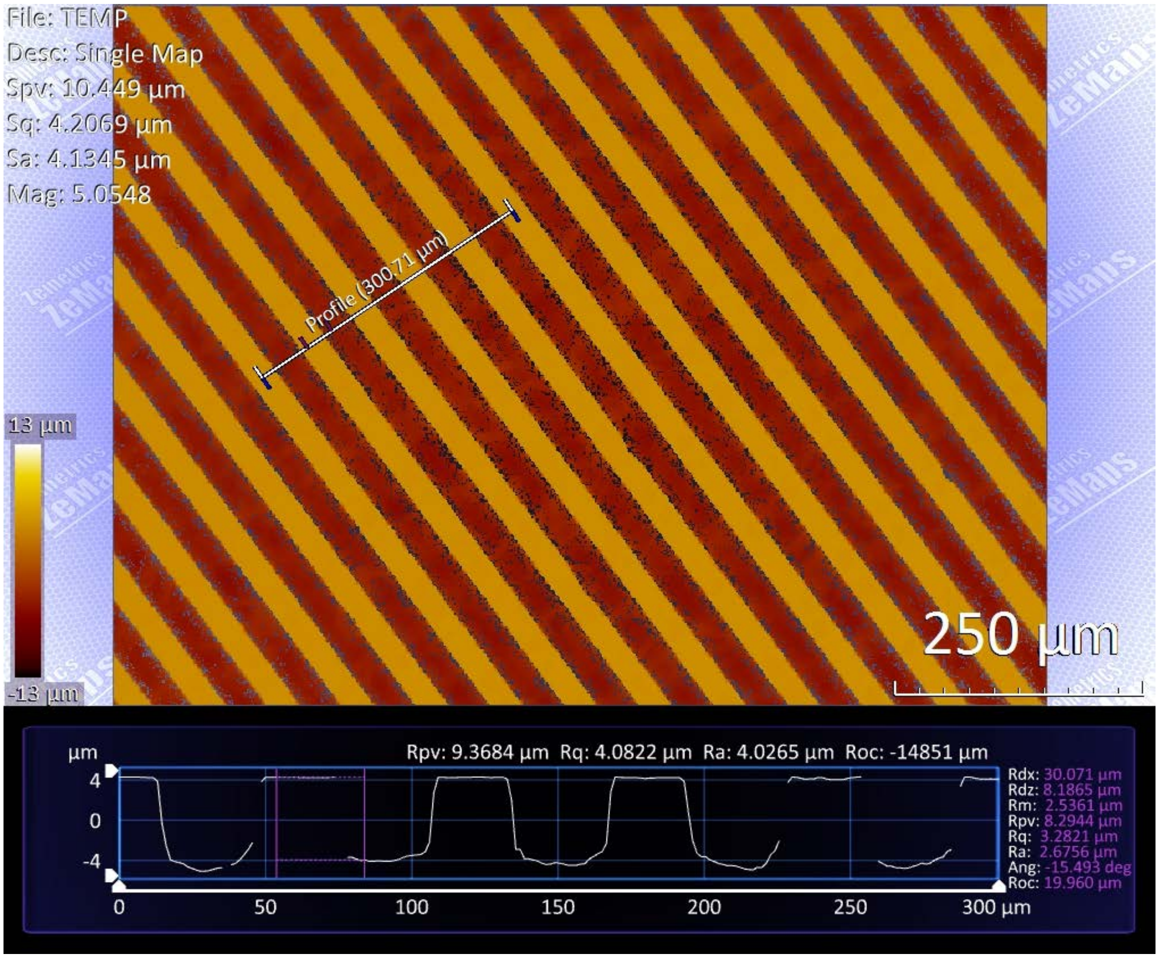

Figure 18: Optical profilometry scan showing uniformity in square wave wavelength and height post heat treatment. Dark spots are missing data points from loss of reflected light and appear as breaks in the surface topography line map, which is the graph at the bottom of the figure.

4.7 Fabrication of Diagnostics Ramps on Surface Perturbation Targets

The testing of target samples with etched surface perturbations, or “ripples,” at TRIDENT proved to be a challenge with regard to producing reliable VISAR diagnostics. Such diagnostics are necessary for obtaining critical information on the sample’s dynamic loading histories and information on spallation, as previously discussed in sections 2.4 and 4.2. One challenge arose from shadowing of the ripple heights on the troughs of the sample, limiting the regions line VISAR and TIDI could probe during testing. The largest available wavelengths from the photomasks (80, 100, and 150 μm) were used to combat this issue. The more challenging issue to overcome was the difficulty in analyzing the fringes that re-create a typical free-surface velocity profile, as seen in Figure 6. Due the presence of the ripples on the diagnostic surface, the fringes produced by the diagnostics become difficult, if not impossible, to follow and analyze. Figure 19 shows the difference in fringe data between a flat sample and a rippled sample.

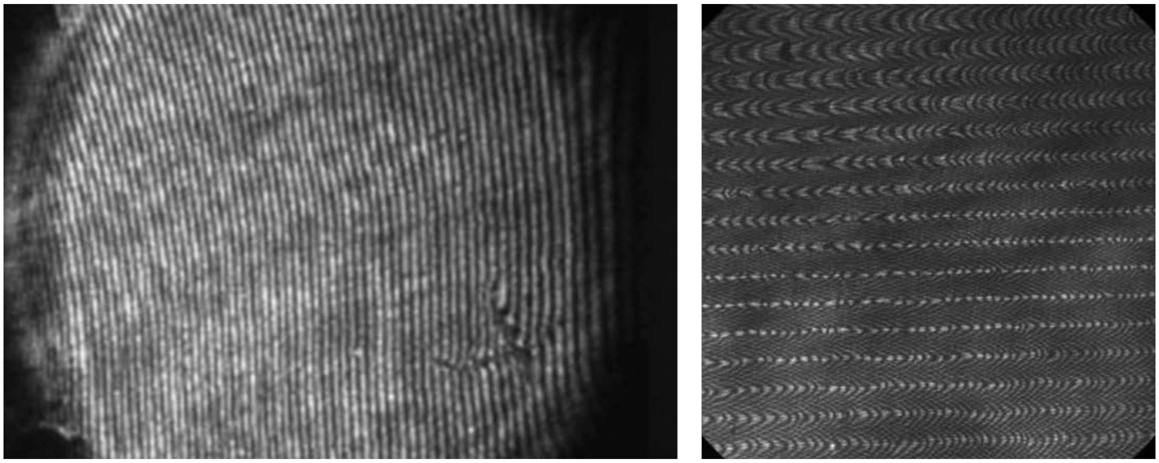

Figure 19: Interferometry data from the diagnostic side of copper target discs for an optically flat specimen (left) and a specimen with a square wave pattern (right).

A strategy to alleviate this issue was to develop a slope the same height as the ripples near the edge of the spall plane on one side of the target. The troughs of the sample become a reference while the peaks can be followed from their maximum height to the reference level. A vertical crystal growth machine with a high precision, variable step motor was used to move a target with ripples into a chemical etchant bath at a rate designed to make the proposed ramp and based on the 3.9μm/minute stagnant fluid etch rate of the 30% $FeCl$, 3-4% HCl, and DI water acid bath. The experimental set-up for this process is shown in Figure 20.

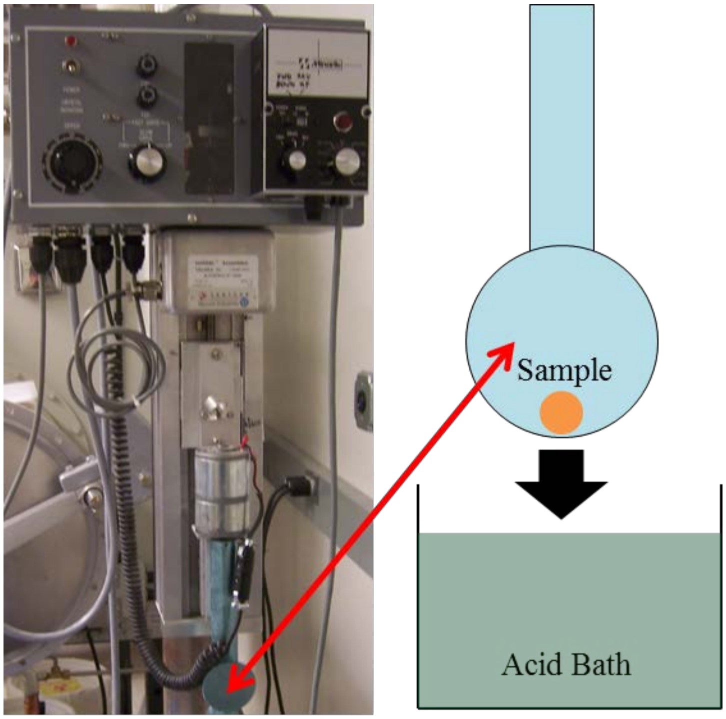

Figure 20: The vertical crystal growth system (left) was used to lower a copper sample into an acid bath (right) and slowly move downward to etch a ramp feature.

4.8 Pre-shot Characterization

After samples were fabricated, pre-shot characterization was performed on the diagnostic side of the targets. A polarized light optical microscope was used to image the diagnostic area, while a Tescan VEGA II Series 4 Scanning Electron Microscope equipped with an EDAX-TSL EBSD camera was used to map microstructural features such as grain size, shape, and crystallographic orientations. Samples were mounted to an attachment piece that slides into the stage of the SEM, and then the stage was rotated 70° from the horizontal, highly tilted toward the EBSD detector. The EBSD detector is comprised of a CCD camera behind a phosphor screen, orientated at 90° from the electron beam pole piece. In this technique, the incident electrons from the microscope beam diffract from the specimen via interaction with the atomic lattice planes of the sample, which are oriented differently for each grain in the specimen, and form Kossel cones around the lattice plane normals. The projection of the diffracted cones of backscattered electrons forms patterns of illuminated light bands, known as Kikuchi bands, on the phosphor screen of the detector, which are detected by the CCD sensor behind the screen [78]. Figure 21 shows a schematic of the SEM-EBSD set-up and the diffraction process.

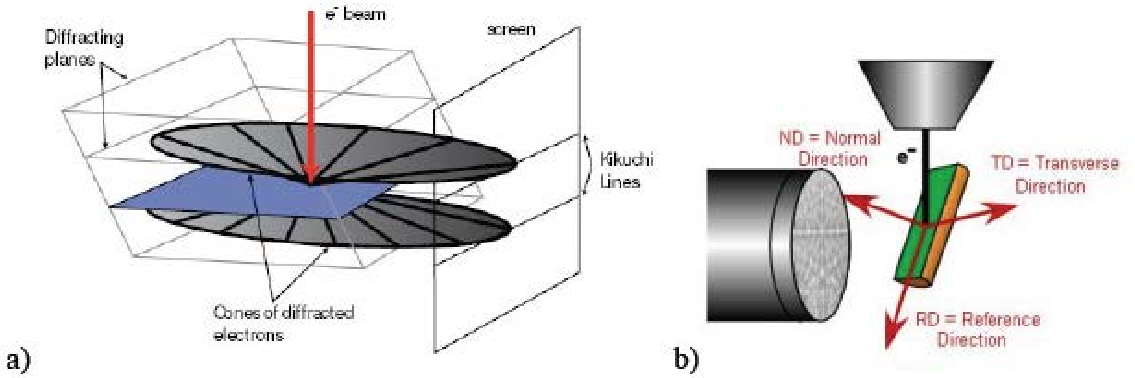

Figure 21: EBSD setup showing the orientation of the electron beam, sample, and EBSD detector with Kikuchi bands on the phosphor screen [78] and the formation of Kossel cones and Kikuchi bands from backscattered electrons [79].

The EDAX-TSL Orientation Imaging Microscopy$^{\text{TM}}$ (OIM) software package was used for EBSD data collection and analysis. The software allows the user to save and read the data in numerous formats and provides many methods for data cleanup and analysis and plotting options. Image quality (IQ) maps and inverse pole figure (IPF) maps are the most convenient ways of visually interpreting acquired EBSD data. Colors corresponding to crystal orientations along a user-specified physical direction make up an IPF map, which is useful for characterizing material texture and lattice orientation changes, as well as a great many other Image quality map overlays give the user a way to visualize the sample's appearance and topography in conjunction with the crystal orientation data from standard IPF maps.

4.9 Post-shot Characterization

All samples were carefully recovered for post mortem characterization using various techniques outlined in detail, in the next few sections, with the underlying goal of linking global and local microstructural features to the presence of nucleated spall. Samples chosen from a copious cache met the fundamental requirement of having tensile pressures at and slightly above the spall strength of the material to ensure void nucleation while suppressing (or slowing) void growth. This information was obtained by analyzing the in-situ diagnostics from testing and utilizing equations 14-18 to calculate shock parameters of interest, such as the maximum pressure, spall strength, and strain rates. In addition to having desirable impact conditions, all characterized samples also had a clear pullback signal indicative of spalling to prevent wasted effort on characterizing samples that may have very few, or no, spall damage sites. Table 2 shows the shock conditions for all samples presented throughout this work.

Table 2: Shock conditions for Cu polycrystalline (PC) and multicrystalline (MC) experiments. The maximum pressure (P_{max}) and spall strength (σ_{spall}) were obtained directly from the VISAR records. The microstructures for the PC specimens are from different processing conditions: as received (AR), heat treated (HT), and fully recrystallized (FR).

Shot ID# & Microstructure	Laser Energy (J)	Flyer Velocity (m/s)	P_{Max} (GPa)	σ_{spall} (GPa)	$\dot{\varepsilon} \times 10^5$ (s^{-1})	Av. Grain Size (μm)
20315 / AR	67	169	3.07	1.48	2.4	150
20316 / AR	54	145	2.62	1.49	2.3	150
20324 / AR	57	148	2.67	1.46	2.4	150
20375 / AR	85	205	4.11	1.22	1.6	150
20366 / FR	68	151	2.98	1.39	0.80	50
20354 / HT	67	155	3.07	1.56	0.80	120
20355 / HT	56	138	2.72	1.56	0.89	120
20357 / HT	100	250	5.04	1.82	2.7	120
24745 / HT	-	-	-	-	-	-
19803 / MC	86	178	3.56	1.64	1.9	450
19804 / MC	93	181	3.63	1.91	2.1	450
19808 / MC	91	185	3.69	1.84	1.8	450
23944 / MC	-	150	2.70	-	-	800
23957 / MC	-	150	2.70	-	-	800

4.9.1 Serial Sectioning of Targets

The key technique for obtaining microstructural information on all shock loaded specimens was consecutive and serial cross-sectioning via mechanical polishing. In serial sectioning, slice depth is dictated by the size of the feature that needs to be resolved or reconstructed. For polycrystalline and multicrystalline samples that require full 3-D reconstruction of their microstructures from EBSD scans, the rule of thumb is that you need at least 10 slices per average grain size to accurately represent the features [45, 46]. Serial sectioning is not adequate to reconstruct the vast majority of individual voids in polycrystalline and multicrystalline samples, as most voids did not grow and coalesce to the average grain size of the materials in this study. The next two sections outline methods used to reconstruct individual voids at acceptable levels of resolution to determine their size and shapes. Figure 22 shows schematically how 2-D sectioning is used to create stacks of images of the spall plane and microstructure to be used for 3-D reconstructions and 3-D FEM models.

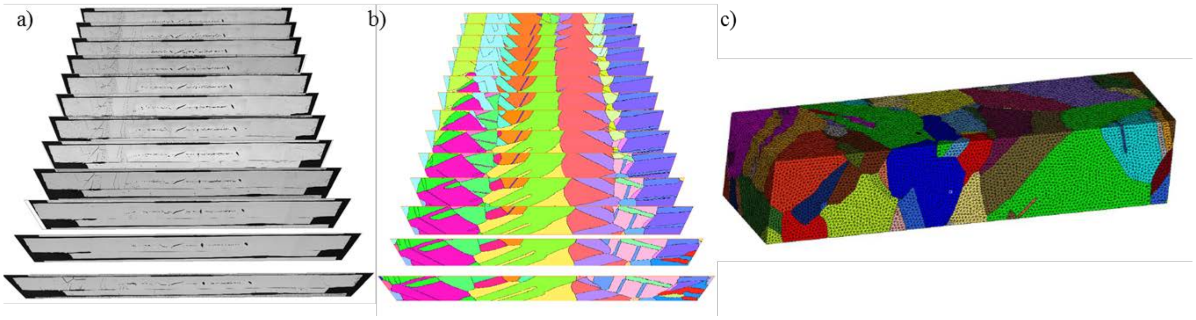

Figure 22: Post shot characterization of copper multicrystals and polycrystals: a) 2-D optical microscopy stack of the spall zone, b) a stack of IPF maps from cross-

sectioning a copper MC, and c) subsequent 3-D finite element model created from a stack of 2-D IPF maps.

In consecutive sectioning, slice depth is dictated by the size of the feature that needs to be considered for analysis, but only once; e.g. for GB statistics enough material needs to be removed between sections so that no unique GBs are double counted. For the work presented here all consecutive sections were done at or slightly larger than the average grain size of the characterized material. Exceptions of two or more large grains sharing a boundary became obvious as material was removed between sections and were thusly thrown out for gathering GB statistics.

Work done by Hashemian [17] and Wayne [18] outline polishing procedures for material removal for each step in sectioning of multi- and polycrystals and were followed for most of the work presented here. The material amount per unit time suggested by Wayne [18] was found to be accurate, though it is noteworthy that material removal for all the work presented here was checked methodically in order to get the correct amount, as there exists slight variations in the material removal between samples. Common methods to adjust the material removal rate during sectioning include, but are not limited to: spending extra time on various steps, varying the applied load, and varying the platen rotation speed and/or direction. As previously mentioned in sections 4.4 and 4.5, an Allied TechPrep^{TM} was used for polishing with both SiC papers and various suspensions. The recent addition of a Pace Technologies Giga-0900 vibratory polisher makes for more controlled and improved final polishing steps using colloidal silica suspensions. The user must change the voltage and frequency controls when using the vibratory polisher to maximize the movement speed of the sample. It was found that a final polish of an hour using colloidal silica yielded substantial optical grain relief and an EBSD quality surface. Table 3 outlines a general procedure used for polishing.

Table 3: Generalized polishing process that may be applied for copper specimens for any sample preparation or characterization procedure. *Indicates an optional step that is usually omitted **Indicates steps that may be used on either the TechPrep™ or Giga-0900 vibratory polisher.

Polishing Surface	Polishing Media	Speed (rpm)	Load (grams)	Oscillation
600 (P-1200) grit SiC	Water	50-80	100-300	No
800 (P-2400) grit SiC	Water	55-65	200	No
1200 (P-4000) grit SiC	Water	55-60	200	Yes
Imperial Pad	5 µm Alumina suspension	45	300	Yes
Imperial Pad*	1 µm Alumina suspension	45	300	Yes
Chem-pol pad, Final A pad, or Final P pad**	0.02 - 0.05 µm colloidal silica	45	300	Yes

Two techniques were used to obtain cross-section samples for mechanical polishing: EDM and diamond wafer blade cutting. EDM became the preferred cutting technique, as the samples do not need to be mounted, the damage layer introduced from the cutting process is well-known (~100 µm thick), and the system is more precise when attempting to cut near or through a feature (such as an individual grain). Since there is a damage layer produced from each cutting technique it was necessary to remove at least

100 µm of material from the free surface in order ensure the material was free of any defects from machining. After exhuming a cross-section sample from a post mortem target disc, the sample was then mounted in epoxy. The sample was typically placed between two copper or brass pieces of roughly the same thickness of the sample itself and held in place by plastic clips. Brass is used as an alternative material to copper as a support piece due to it having a similar removal rate as copper during polishing. The primary purpose of the support pieces was to prevent rounding at the edges of the sample during polishing, which was of great concern, particularly for the samples with surface perturbations. The supports also give additional metallic surface area for removal during polishing. Through experience this tends to make the surface area polish more uniformly than having a sample sitting alone in an epoxy mount. Figure 23a shows a typical cross-sectioned sample mounted in epoxy for analysis.

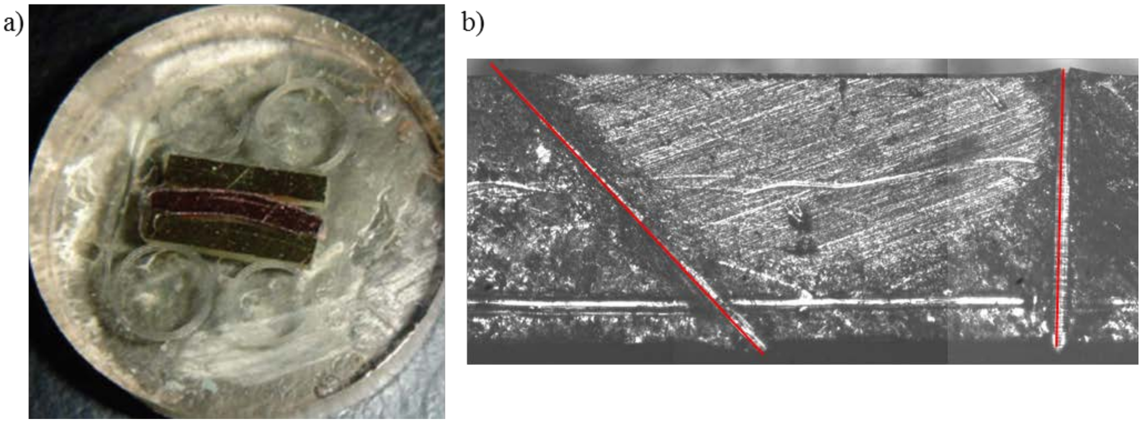

Figure 23: (a) Cross-section of copper sample between two brass support pieces mounted in epoxy for analysis and b) top-down view (shock direction out of page) of two fiducials from CNC milling techniques (highlighted with red lines) on a shocked copper sample.

Image registration is an important factor in 3-D reconstructions of a sample. Serial cross-sectioning provides a stack of 2-D images that can be combined to create a 3-D reconstruction of the microstructure and/or the spall damage itself. There is a need for a physical marker, or fiducial, for this type of precision work. For some samples the fiducials were placed on the support pieces used in the aforementioned epoxy mounting process and for others fiducials were placed on an edge of the sample itself. The fiducials were made by using a razor blade lowered by the vertical displacement precision of a tabletop computer numerical control (CNC) mill. A high resolution camera was placed to monitor the distance between the tip of the razor blade and the sample's surface. Once there was no visible gap between the sample's surface and the razor blade the CNC mill was displaced anywhere from 20-50 microns into the sample for a clear, visible cut. Three fiducials were typically imprinted on the sample using this technique: two marks perpendicular to the cross-section face and one mark between these two at a 45° angle with the face. As material is removed via polishing the distance between the perpendicular marks and the 45° angled mark will decrease for one of them and increase for the other. Since the geometry is known, simple calculations may be done to determine the exact amount of material removed with each sectioning step. Figure 23b shows the geometry of this fiducial method.

Another straight forward technique used for placing fiducials onto a sample for serial sectioning alignment and removal rate control was the use of Vickers indentation. For some polycrystalline samples, Vickers indents were placed in the middle of the cross-sectional area and at the edge of the spall plane for the first polished 2-D section. The

Vickers indent was done at 1 kgf, resulting in a depth large enough for 2-3 serial sections. After a Vickers indent was nearly removed, another pair was placed at the centers of the previous indents to maintain the correct distance between fiducials for reconstruction purposes. One advantage of the Vickers indentation fiducials over the CNC, razor blade method is the hardness of the material is found from the initial indentation. Fiducials are also important for 3-D X-ray tomography analysis, which is discussed in Section 4.9.3.

4.9.2 Serial Sectioning of Individual Voids

It is possible to reconstruct large volume voids from multicrystalline specimens via mechanical serial sectioning, and has been done in previous works [18, 19, 24]. These large volume voids are reconstructed from SEM and/or optical microscopy imaging from sectioning techniques outlined in the previous section. However, since the specimens in this study contain predominantly incipient spall damage, the average void sizes make it difficult to reconstruct individual voids via mechanical polishing. Wayne reconstructed individual voids as small as 5 μm in diameter using Focused Ion Beam (FIB) serial sectioning [19]. Techniques for sectioning voids using FIB are expanded upon in this work to include the surrounding microstructure by including EBSD analysis. The focus from Wayne [19] was void shape, whereas the focus on FIB sectioning here is the plastic deformation surrounding inter- and transgranular voids.

ASU has a FEI Nova 200 that was used to work as a duel-beam FIB-SEM instrument at the Leroy Eyring Center for Solid State Science that consists of a Gallium$^+$ ion source capable of micromachining at the nanoscale. Figure 24 shows a schematic that is representative of the experimental set-up with the inclusion of an EBSD system. The sample must be tilted 52° for ion milling and at 70° for EBSD collection, which made sample maneuvering in the chamber a key element as to not disrupt the sample or the system. The sample was rotated 180° after ion milling then tilted 18° for the EBSD detector.

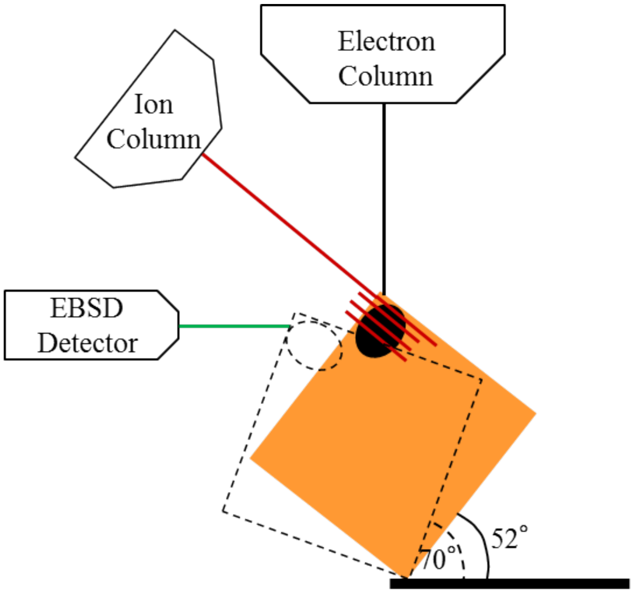

Figure 24: Schematic of the duel beam FIB-SEM with an EBSD detector for serial sectioning and orientation mapping sequencing. The dashed geometry is after rotations about the vertical and out of plane axes for EBSD collection.

For sample preparation, the surface where the flyer struck the target was ground down using a combination of mechanical grinding and final polishing with colloidal silica suspension until the spall plane wasrevealed through the thickness. The through thickness face was also polished to reveal voids through the cross section. With two sides of the sample polished, voids were identified using optical microscopy and the sample were ground until several voids of interest were at the corner of these two faces (see the location of the void in Figure 24). Sectioning was performed on a void in a shocked copper multicrystal target at the LeRoy Eyring Center for Solid State Science. Figure 25 shows that during mill sectioning the lattice orientation changes around the primary void of interest (at the bottom edge of the EBSD scans) and smaller secondary voids were revealed. More detailed results will be analyzed in Chapter 5. Unfortunately, the EBSD detector was removed from ASU’s FIB and further experiments were conducted at Los Alamos National Laboratory under a similar experimental set-up.

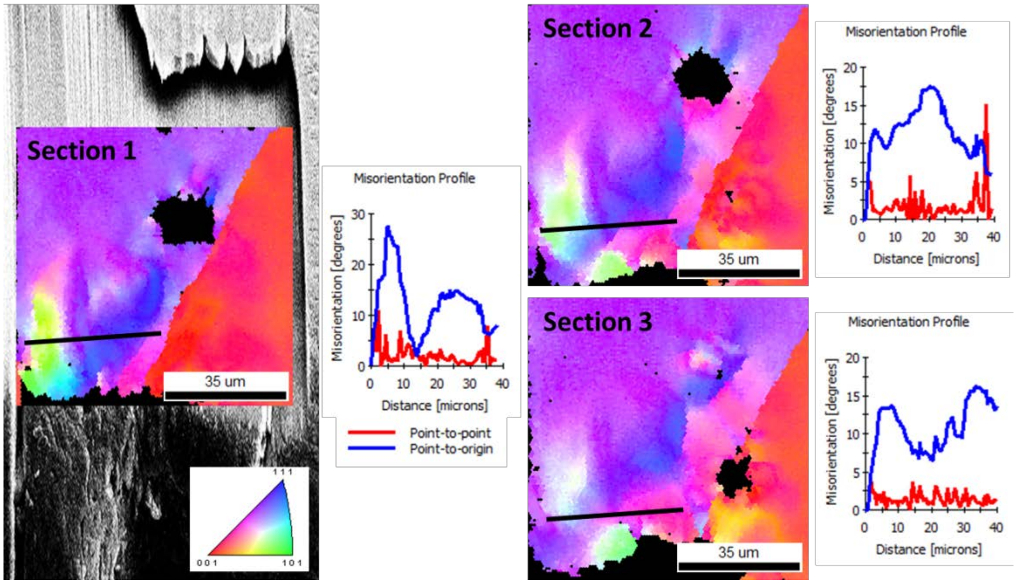

Figure 25: Three sections obtained from FIB milling and EBSD acquisition showing IPF maps with point to point and point to origin misorientation profiles along the black lines. Note that the large transgranular void at the bottom of the images was the void of interest, but smaller voids were also captured during the process, giving insight to void interactions.

4.9.3 3-D X-Ray Tomography of Spall Plane

Serial sectioning techniques are adequate for obtaining microstructural statistics and creating 3-D reconstructions of the microstructure, but lack the resolution to capture accurate size and shapes of individual voids within the spall plane of a shocked target specimen. Data obtained from 3-D X-ray tomography (XRT) are essential to analyze the size, shape, and distribution of voids within the material. Aside from the resolution advantages, X-ray tomography enables one to directly study the shapes of individual voids found in the material, which should differ between inter- and transgranular damage modes [22, 23, 24] based on the microstructure of the material.

Rectangular sections with a 1mm x 1mm cross-section were exhumed from the central spall region of samples for 3-D XRT analysis via either diamond wafer blade or EDM cutting. Exhumed sections, shown in Figure 26a, were polished on the exposed surfaces, removing at least 100 µm from each free surface to remove areas that may be affected by cutting and to provide a smooth surface for fiducials. Radiographs were taken of Samples 20357, 20366, and 20375 at LANL; however, it was discovered that the damage present in the section scanned from sample 20357 was towards the outer edge of the spall, which may be affected by lateral release waves due to the geometry of the experiment [19]. This rendered the data unreliable for quantitative analysis. Information on the X-ray source and beam conditions at LANL may be found in [80].

X-ray tomography data for samples 20354 and 20355 were collected at the Advanced Photon Source (APS) at Argonne National Laboratory (ANL) on beam-line 2-

BM. An uncollimated white beam with energy of 60 keV measuring 50mm x 3mm (horizontal x vertical) at the sample was used for data acquisition. The X-ray source was passed through 15mm of glass and 15mm of silicon to reduce beam hardening. The sample rotated at 1.2° per second during acquisition, remaining within the full 1.66 mm x 1.4 mm (2560 x 2160 pixels) field of view of the CCD camera. The general experimental set-up for XRT is shown in Figure 26b. The pixel sizes of the data acquired from LANL and ANL are 2.24 µm and 0.65 µm, respectively. The ~3.5x better resolution per pixel at ANL stems from the benefits of higher flux and better CCD camera resolution available at the APS.

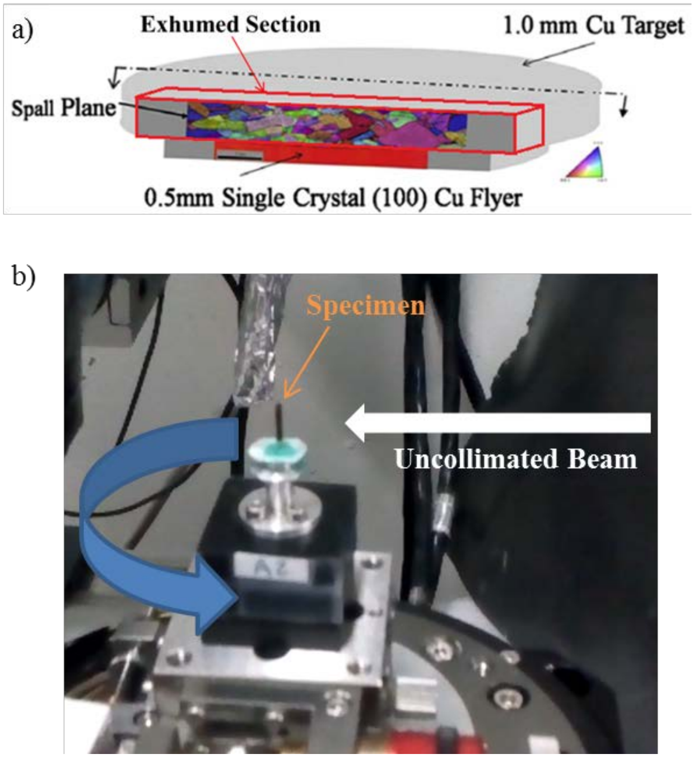

Figure 26: a) Location of a typical exhumed specimen within the central spall region of a shocked target and b) experimental setup inside of the hutch station 2-BM at the APS.

The blue arrow indicates the rotational degree of freedom of the stage during the data acquisition process. The CCD detector is located outside the field of view on the left.

Data obtained from serial and cross-sectioning experiments and XRT experiments required rigorous data processing and analysis to provide quantitative results. Various levels of data cleanup and manipulation were employed throughout the 3-D reconstruction process, prior to gathering quantitative results. The following chapter describes the procedures used for data analysis and 3-D reconstruction for each experimental method.

5. DATA PROCESSING AND ANALYSIS

Serial sectioning and XRT provided the means to comprehensively study spall behavior on both global and local length scales. Serial cross-sections provided for 2-D images that were used to gather statistical information about the location of spall damage within the microstructure for polycrystalline samples. Serial cross-sections of multicrystalline samples provided for detailed 3-D characterization of large volume damage sites and 3-D reconstruction of the surrounding microstructure. Serial sectioning of partial individual voids provided insight into the plastic deformation by means of analyzing the lattice rotations surrounding inter- and transgranular spall damage. Lastly, 3-D XRT provided the data necessary to both qualitatively and quantitatively characterize the shapes of voids within the spall plane of polycrystalline targets of varying thermo-mechanical histories, leading to conclusions on the damage modes present in the materials. Each of these characterization methods involved data cleanup and the use of specialized analysis software to extract meaningful results. Commonalities among the techniques, as well as unique specifics, are discussed in detail throughout this section.

5.1 EBSD Data Cleanup Processes

Before explaining the cleanup processes used, it is important to understand the contents of files using EDAX's Orientation Imaging Microscopy (OIM) software for collecting EBSD data. Each point of an EBSD scan is assigned an x and y coordinate, Euler angles that defines the orientation in 3-D space, and a confidence index (CI). The size of the data points are user defined at the onset of the EBSD scan; a smaller step size means higher resolution, but at the cost of scan time and filament life. Typical scan increment sizes used for this work were 1-3 µm for polycrystalline specimens and 3-10 µm for multicrystalline specimens, yielding at least 100 or more points across an average grain in each microstructure. The CI term is important to understand because it is the primary term called by the software during data cleanup processes. Obtaining the best fit for each individual data point improves the most accurate single average orientation per grain, which is vital for collecting polycrystalline statistics and rendering 3-D reconstructions for multicrystals.

The CI is a parameter calculated during automated indexing of the diffraction pattern and for a given diffraction pattern there may exist several possible orientations that satisfy the diffraction bands detected by the image analysis routines [79]. The solutions for the diffraction bands are ranked by best fit using a voting scheme. The CI is defined as:

$$CI = (V_1 - V_2)/V_{IDEAL} \tag{20}$$

Where, V_1 and V_2 are the number of votes for the first and second best solutions and V_{IDEAL} is the total possible number of votes from the detected bands [79]. Thus, the CI range is from 0 to 1. According to the EDAX-TSL documentation a CI of 0.1 has a 90% probability to have the correct index [79]. It is noteworthy, however, that this process is not without its' flaws, since a CI of 0 may be achieved when $V_1 = V_2$ and the pattern may still be correctly indexed. Smoothing out these possibly correct, yet low CI points is one reason that data analysis and cleanup is necessary. The three most common cleanup procedures used in this work to smooth out data sets in OIM were: grain dilation, neighbor CI correlation, and neighbor orientation correlation.

Grain dilation is an iterative method that assigns points not belonging to a grain to a neighboring grain. A point may be considered as not being part of a grain by either: a) being unindexed or b) belonging to a grain group that does not meet the user defined minimum number of points to be considered a grain [79]. Points that are not allocated to a grain are changed to that of the majority neighboring grain, as seen in Figure 27a. If there is a tie for majority neighboring grain, then a random grain is selected for the point to join. This process repeats for every point in an undefined grain group, and then the orientations for redefined points are changed to match that of the highest CI neighbor of the assigned grain.

Neighbor CI correlation is a simple cleanup method that allows the user to define a minimum CI that is acceptable in the data set. If a point is less than the defined value (0.10-0.15 are a typical values used) then the software checks to find the neighbor with the highest CI value and reassigns that point the orientation and CI of the neighbor with the highest CI [79]. This process is illustrated in Figure 27b.

Neighbor orientation correlation has the most conditions of the three point to point cleanup procedures used here. For this cleanup method, each data point is individually tested for two conditions: 1) Check to determine if the orientation is different from its immediate neighbors based on a given grain tolerance angle (usually ±5°) and 2) determine the number of nearest neighbors that represent like orientations within the given tolerance angle [79]. A cleanup level is specified when this procedure is ran, which ranges from 0 to 5. For condition one a cleanup level of 0 means that all nearest neighbors must differ in orientation to proceed, up to cleanup level 5 where only one nearest neighbor must be different. For condition two a cleanup level of 0 requires all neighbors to be of a similar orientation, up to cleanup level 5 where all may be different. If both conditions are satisfied then the point in question is changed to one of the neighbors involved meeting the conditions, at random. Cleanup levels are performed sequentially, meaning a selected cleanup level of 4 must perform level 0, followed by level 1, then level 2, then level 3, and finishes with level 4 [79]. Figure 27c shows a schematic of this process.

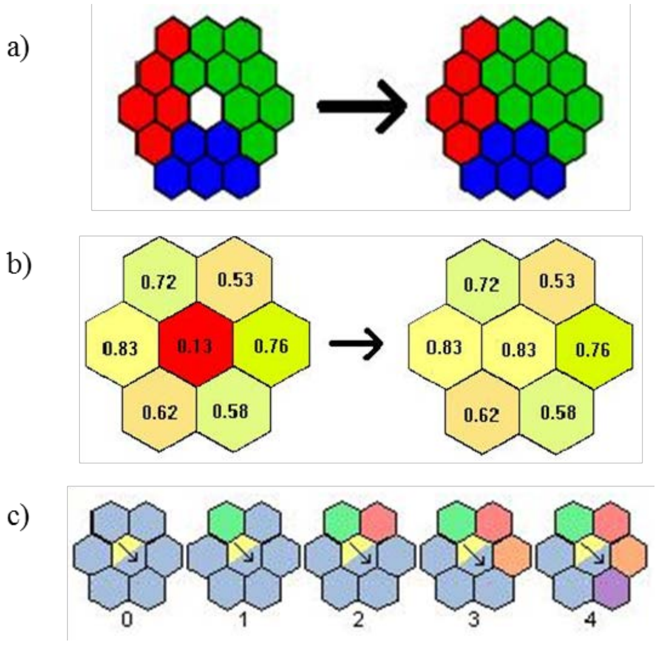

Figure 27: EDAX OIM software cleanup procedures for EBSD data: a) grain dilation, b) neighbor CI correlation, and c) neighbor orientation correlation. Note that the colors in each schematic are meant to be representative of an orientation [79].

5.2 2-D Damage Statistics in Polycrystals

Polycrystalline samples were ideal for the quantitative statistical study of preferred boundaries for damage localization due to the high density of GBs found within each 2-D cross-section, as a result from the small grain sizes. A high density of GBs within the material provided for an increase in potentially weak sites for damage nucleation. Post-mortem EBSD data collected from each cross-section were used to analyze micro-textural information. The misorientation angles of boundaries that contained damage, as well as their crystallographic orientations, were the primary focus of study for a statistical analysis of boundary strength within the materials.

In order to accurately measure these properties, the data cleanup procedures presented in the previous section were explored. Each EBSD scan could have experienced several iterations of data processing and cleanup; however, in most cases EBSD data required only a single iteration of cleanup before executing the single average orientation per grain function. Each procedure ended with taking the single average orientation per grain with a tolerance of ± 5° due to the existence of plastic strain induced by manufacturing of the original copper plate and strain localization around GBs from spallation. Specimens that underwent heat treatments had most of this pre-existing plastic strain removed; however, the single average orientation per grain was still taken for consistent measurements of grain orientations. Figure 28 shows the difference in a raw EBSD scan of a sample containing plastic strain and the same dataset after cleanup. Prior to applying the averaging procedure the misorientation across a boundary could be measured accurately within ± 5°, whereas this improves to ± 2.5° after the averaging procedure.

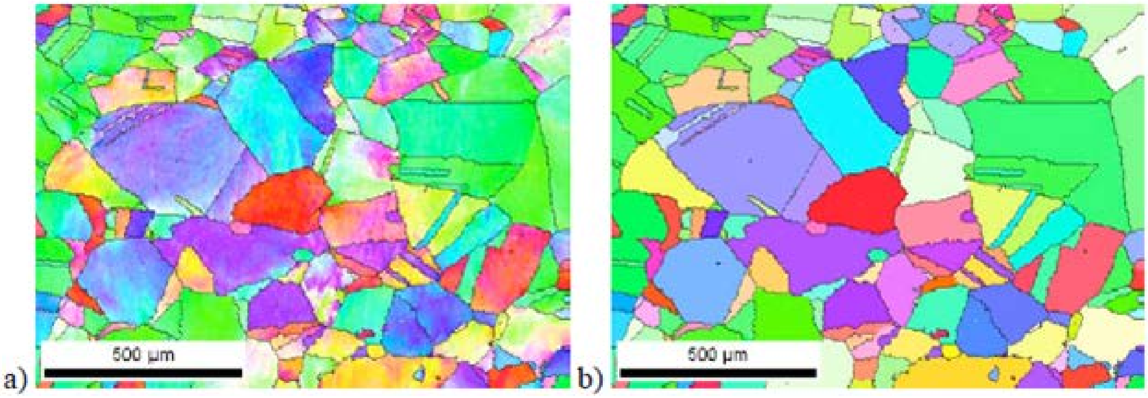

Figure 28: IPF maps from EBSD data for a copper polycrystal in the as-received condition. a) Raw data, and b) the same dataset after a single average orientation per grain cleanup. [20]

The EBSD data analysis software was used to measure the orientation of grains adjunct to each damage site clearly present at a GB, as well as the misorientation angle across each boundary that localized damage. Histograms were constructed from the misorientation angles of the damaged boundaries to showed preferred misorientations for damage nucleation and a distribution based statistics analysis was used to determine the error present in the data. The details on this analysis are presented in the next section.

Before beginning the statistical study on GBs with and without damage in a shock loaded specimen it is important to consistently define the region containing pertinent information. The spall zone was taken by cropping the EBSD cross-sections to encompass a rectangular area bounded by the upper and lower most voids across the entire damaged area, as seen in Figure 29. It was important to not count any boundaries outside of the defined spall zone because this improperly counts undamaged GBs where no damage was present, which would underestimate the overall probability to find damage within the material. On the other hand, it is also important to count every boundary within the defined region, otherwise there may be an overestimation of the probability of finding damage given a misorientation angle range.

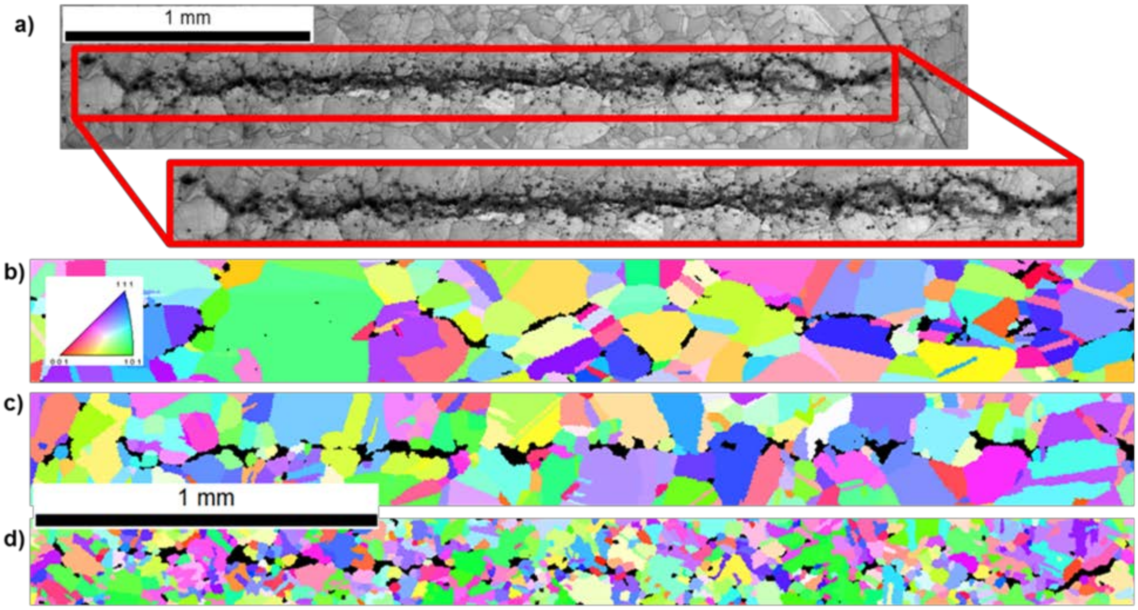

Figure 29: a) Selecting the spall zone from an image quality map in the EBSD software for GB analysis indicated by the red rectangle. Inverse pole figure maps from EBSD data are shown for b) sample 20315 (AR), c) sample 20357 (HT), and d) sample 20366 (FR). The black regions are voids.

After the data were cropped and had undergone proper data cleanup procedures, one final step must had to occur before collecting data. This step was adding a size partition to the IPF, which will omit "grains" smaller than a defined size. Spall damage appears as multi-colored “noise” within an EBSD scan and it was important that after cleanup procedures none of these regions be accidentally counted as grains. The black regions representing voids in Figure 29b-29d are from a partition. Overlaying a transparent image quality map on top of the IPF was a method of double checking all voids were accounted for from the partition step.

The GBs with misorientations of 5^{o} or less were not considered because a tolerance of 5^{o} was used by the EBSD software to define a GB, which was applied for all specimens. Counts of angles were grouped into bins of 5^{o} for each microstructure, ranging from 0^{o} to 65^{o}, and plotted on a histogram, with a horizontal error of $\pm 5^{o}$. As previously discussed in the literature [18, 22], it is important to normalize statistical distributions to estimate the frequency of damaged boundaries for a given misorientation as a fraction of the total boundaries for each misorientation bin within the area of interest. Bayes’ theorem [20] was implemented to normalize the damage distribution to find the true probability of finding damage $(X = 1)$ at a given GB given its misorientation angle θ:

$$P(X = 1|\theta) = \frac{P(\theta|X=1) \times P(X=1)}{P(\theta)} \tag{21}$$

where $P(\theta|X = 1)$ is the probability that a boundary of a misorientation has damage and is measured directly from binning all boundaries with damage and dividing each bin by the total number of damaged boundaries. $P(\theta|X = 1)$ accurately describes the probability to find damage at GBs within the spall zone containing damage; however, it does not reflect the response of the overall microstructure to the presence of spall damage as it does not take into account GBs without damage. Thus, $P(\theta|X = 1)$ is needed to take into account texture and to accurately represent the probability to find damage at misorientations ranges. $P(X = 1)$ is the total number of damaged boundaries over the total number of boundaries, and $P(\theta)$ is simply the total misorientation angle distribution. Each of these terms was also analyzed separately for drawing conclusions on boundary strength.

Vertical error bars were created for the distribution of $P(X = 1|\theta)$ in order to elucidate if changes in probability between bins are relevant. Since the general shape of this distribution is not Gaussian in the sense that the distribution is over a closed interval a more flexible distribution was selected to fit the data. Error bars were created by splitting the $P(\theta|X = 1)$ and $P(\theta)$ distributions into two sections, 0^o to 50^o and 50^o to 65^o, and fitting each section with the highly flexible, bounded Johnson Sb distribution [81], seen below in eq. 22.

$$f(x) = \frac{\delta}{\lambda\sqrt{2\pi}z(1-z)} \exp\left(-\frac{1}{2}\left(\gamma + \delta \ln\left(\frac{z}{1-z}\right)\right)^2\right) \tag{22}$$

Where, γ and δ ($\delta > 0$) are continuous shape parameters, λ ($\lambda > 0$) is a continuous scale parameter, the domain is set by $\zeta \leq x \leq \zeta + \lambda$, and $z \equiv \frac{x-\zeta}{\lambda}$. For each microstructure Johnson Sb distributions were assigned random numbers equal to the number of damaged boundaries within that distribution's misorientation range and repeated 10,000 times. A standard deviation was found for the resulting number of counts in each 5^o misorientation bin and propagation of error [82] was applied to eq. 21 to find the total error for $P(X =$

$1|\theta)$ and applied to the distribution plots as vertical error bars. The results are discussed in detail in Chapter 6.

5.3 3-D Microstructure and Spall Damage Reconstructions

Reconstructions of spall damage and the surrounding microstructure were performed for copper multicrystals. The physical process of serial sectioning, scanning, cleanup procedures, and preliminary reconstructions were documented previously by Wayne [18]. The work presented here aims at using these data sets and improving upon the reconstructions to extract physical 3-D data useful for modeling efforts [19, 24] and for qualitative analysis of microstructural effects.

An issue of primary concern when constructing 3-D rendering of a sectioned microstructure is to be consistent with the orientations of each grain. Slight variations in colors, or, the orientations of individual grains, are probable during the process. The concept of a crystallographic fiducial was developed and implemented by Wayne [18] for reconstructing multicrystalline specimens. A polished silicon single crystal of a known orientation was fixed to the polishing fixture next to the sample being sectioned and scanned along with each section of the specimen [18]. A Matlab code was developed by Wayne [18] to detect any rotation in the orientation of the single crystal from the original section, then multiply it by respective orientation matrices of Euler angles from the specimen's EBSD scan and convert them back to Euler angles to import the corrected orientations back into the EBSD software for analysis [18]. Before importing the EBSD sections into Avizo^{TM} for 3-D reconstruction, each slice underwent noise and non-indexed point removal associated with spall damage with the cleanup features discussed in Section 5.1. To simplify the reconstruction process, the grains were outlined in black on the IPF maps, which aided in assigning labels to each grain.

Each 2-D data slice in a reconstruction, typically in a .tiff format, is dimensioned in pixels in the x- and y- directions. After importing a stack of 2-D slices into the reconstruction software the distance between slices is specified and the dataset becomes represented by 3-D voxels, which are essentially pixels with an added third dimension giving them volume. In the software a function called "orthoslice" may be used to view each 2-D image in sequence to verify that the data sets are properly aligned before continuing to the segmentation process.

The process of assigning voxels to a label field containing one or more materials is called segmentation. For reconstructions of spall damage from optical and/or SEM images, segmentation was performed in one step via simply applying a "threshold" function to the stack of images. The thresholding process, formerly called "binarisation" in the software, is performed by manually adjusting the range of contrast to separate the bulk material (white in this case) from the voids (black). It is important to select a threshold such that the voids maintain their proper shape while avoiding selecting voxels outside of the void. Oversaturation of the voids leads to unwanted connectivity between voids when the process is finalized, which is detrimental to volumetric and shape statistics. A "label field" module may then be used to further assign a number to each unique void for statistics.

Segmentation is not as simple for the microstructural reconstructions as the EBSD scans contain many colors and the color of individual grains do not have to have the same RGB value between slices. This means that an auto-segmentation function cannot be applied for the microstructure and manual segmentation tools were often required for assigning voxels from different slices to the same grain. Manual selection of the label field for the grains was aided by adding interpolated slices between the existing imported slices, which smoothed the edges of the microstructural features. This method of interpolation was found to lead to significant improvements to both the microstructure and damage reconstructions. The reconstruction process for the microstructure and the damage were initially done separately, and then later combined into one workflow for visualization purposes.

5.4 3-D X-ray Tomography Reconstruction and Analysis

Data acquired from the 3-D X-ray tomography experiments at LANL and ANL's APS were used to reconstruct the spall zone in several samples. All data sets underwent smoothing, segmentation, and thresholding procedures using the software package Avizo^{TM} in order to remove artifacts, such as two separate voids appearing as one due to close proximity. The thresholding technique used here was the same as that described in the previous section. The data from LANL was formatted in a way to be read directly into the reconstruction software, whereas the data from APS had to go through Python scripts to get 2-D tiff images that could be imported and reconstructed similar to that of the serial sectioned data, but at a very high resolution. As previously mentioned in Section 4.9.3, the voxel sizes of the data acquired from LANL and ANL are 2.24 μm and 0.65 μm, respectively.

It has been reported that one needs ~80 voxels in order to correctly measure the surface area of an object, ~120 for the volume, and ~1,000 for the 3-D Feret shape to maintain 10% or less absolute error [83]. The 3-D Feret shape is a number used to quantify the relationship between the minimum and maximum feature lengths in an object; as this number approaches 1 the object becomes spherical. Samples with a pixel size of 2.24 μm contain voxels 11.24 μm^3 in volume, which requires a minimum volume of 11,240 μm^3 for accurate 3D Feret shape measurements. For samples with a pixel size of 0.65 μm, making one voxel 0.275 μm^3, the corresponding minimum volume is 275 μm^3. For the purpose of this work it is important not only to capture the shape of voids for visual inspection, but also to maximize the number of voids analyzed for volume statistics.

Volumetric sieves were performed at 120 and 1,000 voxels for samples 20366 (FR) and 20375 (AR) to visualize how much information is lost as the minimum volume for a void is chosen. This process is shown for sample 20366 in Figure 30. For samples containing a 2.24 μm voxel size, the void minimum 120 voxel sieve (corresponding void radius of ~7 μm) was chosen for visual inspection of void shapes in this work since it is the number voxels required for accurate volume resolution while preserving many of the voids in the data set. A minimum volume of 120 voxels was also used for global statistics such as average void volume and void volume fraction because the shape is not of interest, but preserving the surface areas and void volumes are necessary. For shape fitting of the voids a minimum of 1,000 voxels (corresponding void radius of ~14 μm) was used to preserve the 3-D shape necessary for this process. Due to the better resolution obtained from the APS data, the 0.65 μm voxel size data sets have a minimum void radius of ~4 μm with the 1,000 voxel minimum, thus its sieve was conducted at this value and was used for both shape inspection and global statistics.

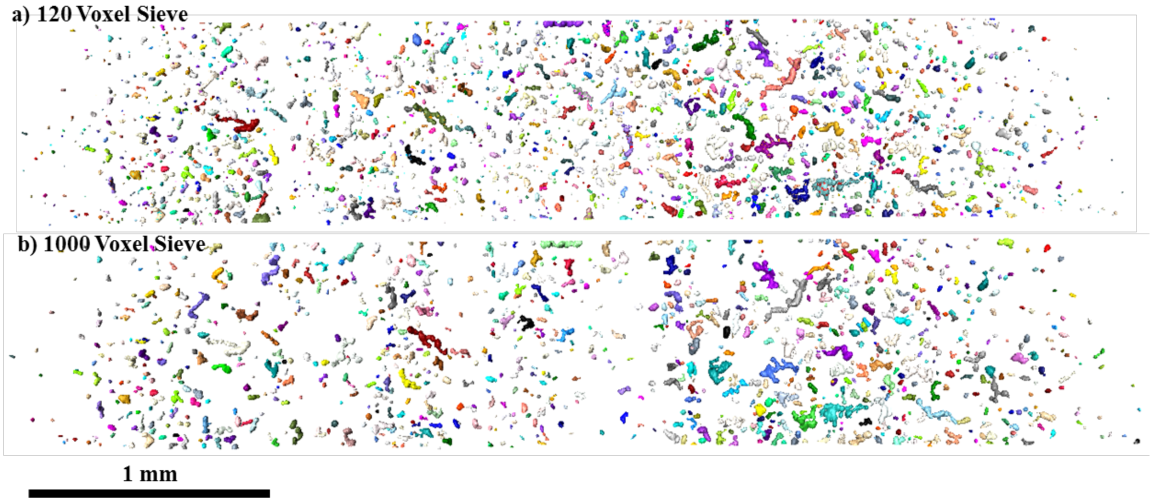

Figure 30: Volumetric sieving process for sample 20366 (FR). The minimum volume voids shown are: a) 120 voxels (1,348 μm^3) and b) 1,000 voxels at (5,018 μm^3). Void colors are random and for visual aide only.

For clarity and completeness, the process of obtaining full 3-D visualization and individual void statistics is as follows:

1. Import data or image stack with specified thickness
2. Crop to the desired region of interest for large data files to speed up rendering times and clean-up processes.

3. Segmentation of the spall damage and the bulk: apply threshold module and execute.
4. Apply the border kill module to rid of partially reconstructed voids at the boundaries of the data set.
5. Apply a label field module to uniquely identify each individual void.
6. Label analysis may be applied and statistics may be gathered and exported to Excel. This is when a sieve is applied to remove voids above or below desirable volumes.
7. Surface view module may be applied for a full 3-D rendering of the dataset. The data may be exported to many different formats and / or meshed.

5.5 Shape Fitting of Individual Voids

To gather information on the amount of inter- and transgranular damage present within shocked copper polycrystals of varying thermomechanical processing conditions, a criteria was established to relate the shape of the voids to a particular damage mode. It is known that transgranular damage should have the shape of an octahedron [18, 66] and it is suspected that intergranular damage should appear disk or sheet-like since they follow the GBs within the material, and coalesced damage regions should appear as disks or needles. Representative ellipsoids may be fit to individual voids as an attempt to characterize what damage mode they belong to from their shape.

5.5.1 Least Squares Ellipsoid Fitting Method

The spall zone data from 3-D X-ray tomography were exported as a mesh in order to obtain the x, y, and z spatial coordinates of the nodes on the mesh were obtained and stored in Excel files. The points were fitted to the equation of a quadric surface (eq. 14) using a least squares ellipsoid fitting method [84]. An algorithm was written in Matlab to import the data from comma space delimited (CSV) Excel files and perform an automated operation to find the best-fit ellipsoid for each individual void and give its semi-axes and aspect ratios. The code for this program is attached in the Appendix. Most generally, a quadric surface is defined as the locus of points such that their coordinates satisfy the most general equation of the second degree in three variables [84]:

$$ax^2 + by^2 + cz^2 + 2fyz + 2gxz + 2hxy + 2px + 2qy + 2rz + d = 0 \qquad (23)$$

Let,

$$I = a + b + c \qquad (24)$$

$$J = ab + bc + ac - f^2 - g^2 - h^2 \qquad (25)$$

$$K = \begin{vmatrix} a & h & g \\ h & b & f \\ g & f & c \end{vmatrix} \qquad (26)$$

then they are invariants under rotation and translation and equation 23 represents an ellipsoid if $J > 0$ and $I \times K > 0$ [84].

The constraint of αJ – $I^2 > 0$ on equation 23 is shown in [84] to represent an ellipsoid as long as $\alpha \geq 4$. To solve for an ellipsoid based on coordinates in 3-D the least squares fitting problem based on algebraic distance with constraint αJ – $I^2 > 0$ [84]:

$$min\|D\mathbf{v}\|^2 \quad \text{subject to} \quad \alpha J - I^2 = 1 \tag{27}$$

where D is a design matrix consisting of the spatial coordinates for each void in a $10 \times n$ system defined as $D = (\mathbf{X}_1, \mathbf{X}_2, \ldots, \mathbf{X}_n)$. Additionally, the term **v** contains the coefficients from equation 23:

$$\mathbf{X}_{\boldsymbol{i}} = (x_i^2, y_i^2, z_i^2, 2y_iz_i, 2x_iz_i, 2x_iy_i, 2x_i, 2y_i, 2z_i, 1)^T \tag{28}$$

$$\mathbf{v} = (a, b, c, f, g, h, p, q, r, d)^T \tag{29}$$

A 6 × 6 matrix matrix, C_1 is next established as:

$$C_1 = \begin{pmatrix} -1 & \frac{k}{2}-1 & \frac{k}{2}-1 & 0 & 0 & 0 \\ \frac{k}{2}-1 & -1 & \frac{k}{2}-1 & 0 & 0 & 0 \\ \frac{k}{2}-1 & \frac{k}{2}-1 & -1 & 0 & 0 & 0 \\ 0 & 0 & 0 & -k & 0 & 0 \\ 0 & 0 & 0 & 0 & -k & 0 \\ 0 & 0 & 0 & 0 & 0 & -k \end{pmatrix} \tag{30}$$

and define

$$C = \begin{pmatrix} C_1 & 0_{6\times4} \\ 0_{4\times6} & 0_{4\times4} \end{pmatrix} \tag{31}$$

$\alpha J - I^2 = 1$, is rewritten as $\mathbf{v}^T C\mathbf{v} = 1$ and combining this with the constraint minimization problem in equation 23 leads to the problem of solving a set of equations using the Lagrange multiplier method [84]:

$$DD^T\mathbf{v} = \boldsymbol{\lambda} C\mathbf{v} \tag{32}$$

$$\mathbf{v}^T C\mathbf{v} = 1 \tag{33}$$

Equation 32 is the eigenvalue system that needs to be solved to find the solution for equation 27 and completing the necessary steps to determine the major semi-axes of a best fit ellipsoid. For further detail on solving this eigen-value problem, refer to [84] and the Matlab code found in the Appendix of this work. Proof of concept for this algorithm is shown below in Figure 31.

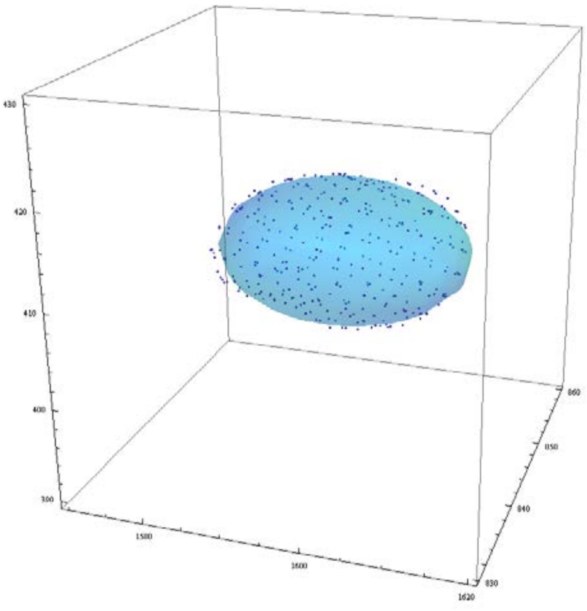

Figure 31: A best fit ellipsoid found from the least squares algorithm (in blue) to the surface nodes of a void exported from 3-D X-ray tomography data.

5.5.2 Inertia Fitting of Ellipsoid Method

The momentum of inertia is a term used to describe the capacity of a cross-section to resist bending [85]. The moments of inertia are mathematical properties that are determined by the shape and mass distribution in 2 or 3-D space with a set of reference axes. For convenience the reference axes are typically set to go through the center of mass of the object for which the moments of inertia describe. As an alternative method to finding a best fit ellipsoid for individual voids via shape fitting from the previous section, the moment of inertia tensor was acquired for each void from Avizo^{TM} and fitted to a representative ellipsoid.

Avizo^{TM} does not define the momentum of inertia of a solid body in the manner in which most are accustomed. For an ellipsoid in Cartesian coordinates, for example, one would expect the moment inertia about the z-axis, I_{33}, to be defined as a combination of the x and y-axes:

$$I_{33} = \int \rho(r) r^2 \, dV = \rho \int (x^2 + y^2) \, dxdydz \tag{34}$$

where $\rho(r)$ is the density of the object and r is the distance from a volume element to the axis of rotation. As a tensor, I_{jk} may be expressed by a 3 x 3 array and is in the form of what many would recognize as the moment of inertia tensor with the diagonal components containing distances from two axes, as with I_{33} in eq. 34. However, Avizo^{TM} does not define the inertia tensor in this manner. As per the user's manual, the second order moments are defined as the following for the discrete case; again using the z-axis as the reference [86]:

$$M_{2z} = \frac{1}{A(X)} \int (z - M_{1z})^2 dxdydz \tag{35}$$

where,

$$M_{1z} = \frac{1}{A(X)} \sum_X z_k \tag{36}$$

Having defined the moment of inertia about the z axis, one must transform this to spherical coordinates, transforming *V* into a unit sphere *V'*:

$$M_{2z} = \frac{1}{A(X)} \int (cz' - cM_{1z}{}')^2 |J| dx'dy'dz' \tag{37}$$

defining,

$$x' \equiv \frac{x}{a}\ , y' \equiv \frac{y}{b}\ , z' \equiv \frac{z}{c} \tag{38}$$

$$J = \left| \frac{\partial(x,y,z)}{\partial(x',y',z')} \right| = abc \tag{39}$$

where a, b, and c are the corresponding semi-axes of an ellipsoid along the x, y, and z-axes, respectively, and *J* is the Jacobian. Assuming the solid body is centered around its own origin and transforming eq. 37 to spherical coordinates, one obtains:

$$M_{2z} = abc \frac{1}{A(X)} \int_0^1 \int_0^{2\pi} \int_0^{\pi} c^2 r^4 \cos^2\varphi \sin\varphi d\varphi d\vartheta dr \tag{40}$$

$$M_{2z} = abc \frac{1}{A(X)} \frac{4\pi}{15} c^2 \tag{41}$$

substituting

$$\frac{1}{A(X)} = \frac{M}{\frac{4}{3}\pi abc} \tag{42}$$

where M is the mass of the object, yielding

$$M_{2z} = \frac{1}{5}Mc^2 \tag{43}$$

Due to symmetry, the other two axes have similar expressions for the moment of inertia about each axis and are taken as:

$$M_{2x} = \frac{1}{5}Ma^2 \tag{44}$$

$$M_{2y} = \frac{1}{5}Mb^2 \tag{45}$$

In comparison, this process done in the same manner using the conventional definition of the inertias about each axis as described by I_{33} in eq. 34 results in the familiar moment of inertia ellipsoidal form:

$$I_{11} = \frac{1}{5}M(b^2 + c^2) \tag{46}$$

$$I_{22} = \frac{1}{5}M(a^2 + c^2) \tag{47}$$

$$I_{33} = \frac{1}{5}M(a^2 + b^2) \tag{48}$$

It becomes very clear that the inertia tensor provided by Avizo$^{\text{TM}}$ using eqs. 43-45 is not the same, even though it is of similar form, as the classical principal inertia – ellipsoid semi-axes relationships in eq. 46-48. Defining the inertias provided by eqs. 43-45 as the principal moments of inertia yields the best solutions for representative ellipsoids for each void, as the ellipsoid is guaranteed to be fit along its major axes. Thus, the eigenvalues of the inertia tensor provided by the software were obtained for each void in the XRT data sets and taken as $M_{2x}> M_{2y}> M_{2z}$. Then, the ellipsoid semi-axes were calculated by rearranging eqs. 43-45:

$$a^2 = \frac{5}{M} M_{2x} \tag{49}$$

$$b^2 = \frac{5}{M} M_{2y} \tag{50}$$

$$c^2 = \frac{5}{M} M_{2z} \tag{51}$$

Thus, it is defined as a convention that the semi-axes of the best fit ellipsoids will always be represented as $c > b > a$. Taking the ratios a/c and b/c and plotting them against one another is a way to visualize the shape distribution of the voids present in each microstructure. Also, by taking these ratios there is no need for the mass (or volume) of the objects to be known as they become cancelled upon dividing. The analysis of how these ratios correspond to inter- vs. transgranular damage present within the samples is discussed in detail in the next chapter.

6. RESULTS AND DISCUSSION

6.1 2-D Statistical Damage Analysis of Polycrystals

Consecutive cross sectioning through the thickness of shocked copper polycrystals of three varying thermomechanical processing histories was performed along with EBSD to do statistical analysis of damaged boundaries: samples 20315, 20316, and 20324 were AR, 20357 was HT, and 20366 was FR. The average grain sizes of these samples (ranging from 50 – 150 μm) were well below the characteristic length scale of 985 μm suggested by Peralta [10] as the threshold above which only transgranular damage occurs. Visual inspection of the EBSD data indicates that mixed modes of trans- and intergranular damage exist for all the specimens, but with a noticeable preference for intergranular damage, especially in the AR microstructure. Figure 32 shows the defined spall zone along with an EBSD scan of AR sample 20315, showing intergranular damage preference. Refer to Figures 14 and 29 for comparable visual inspections between each microstructure.

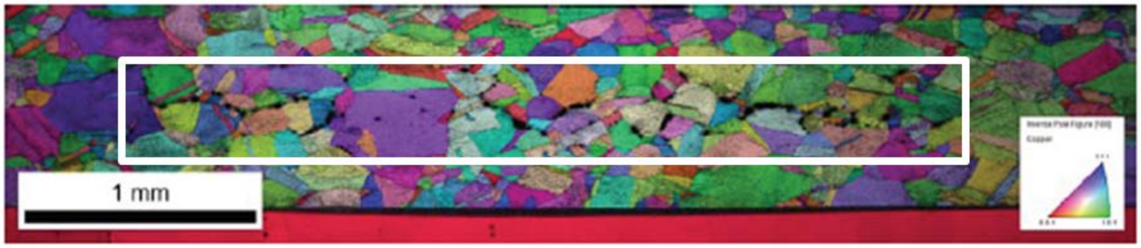

Figure 32: Inverse pole figure map of a cross section from sample 20315 showing predominant intergranular damage and the region probed for GB statistics highlighted in the white box.

The misorientation angles for all boundaries within the spall zone region were analyzed to examine any texture present in the specimens. The total number of cross sections and the total number of GBs probed for each microstructure are AR: 27, 50,438, HT: 10, 9,002, and FR: 6, 26,596, respectively. The AR specimens were the most incipiently spalled, requiring a larger number of cross sections across three samples to gain meaningful data on damaged boundaries. Counts of the misorientation angles for all boundaries in the spall plane were binned into groups with a 5° width and range from 10° to 65°. Misorientations less than 10° were discarded because the data cleanup process may split large grains into two or more grains of a similar orientation given the tolerance of ±5°, though this is rare. The numerical results, illustrated by a histogram of $P(\theta)$ in Figure 33, show a heavy skew towards the 55° to 60° for all three microstructures examined. This misorientation range is commonly indicative of $\Sigma 3$ twin boundaries, which have a 60° misorientation angle and infiltrate into the 50° to 55° and 60° to 65° as per the Brandon's criterion for special GBs [87].

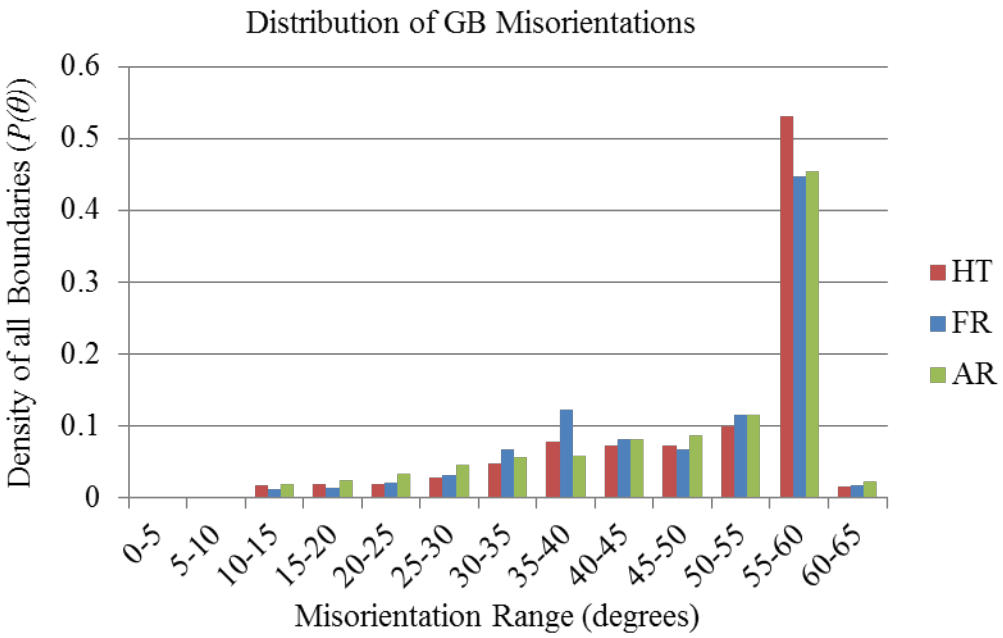

Figure 33: 2-D statistics of all boundaries within the spall zone, *P(θ)*, for each microstructure examined [23]. There is a horizontal error of ±5° for all data.

The HT specimen contained the highest percentage of GBs within the {111} Σ3 twin range, while the FR and AR specimens contained roughly the same counts within these misorientation ranges. However, it is noteworthy that the FR microstructure has a noticeable increase in the 35° to 40° misorientation range, which includes {110} Σ9s per Brandon’s criterion. It is expected to find {110} Σ9s at junctions containing two {111} Σ3s, which is often a result from annealing [88]. To compare the presence of these secondary annealing twins in all three samples, the total coincident site lattice (CSL) boundary fraction, Σ3 boundary fraction, and Σ9 boundary fraction were found for each sample; these results are shown below in Table 4.

Table 4: CSL Boundary Distribution for PC Specimens

Microstructure	CSL Fraction	Σ3 Fraction	Σ9 Fraction	Other CSLs
HT	0.608	0.536	0.052	0.020
FR	0.553	0.461	0.072	0.020
AR	0.392	0.355	0.008	0.029

The AR specimens had the lowest fraction of CSL boundaries and contained less than 1% fraction of Σ9 GBs, which confirms their presence in the HT and FR specimens comes from annealing twins. The HT specimen contained ~5% greater CSL fraction, but ~7% fraction more Σ3 boundaries than FR samples, however, this is "offset" by the 2% fraction increase in annealing Σ9 boundaries in the FR specimen. Since the grain size in the FR specimen is much smaller than that of the HT specimen there are more geometric opportunities for Σ9 annealing twins to occur from triple junctions. IPF plots showing the axis/angle pairs of GBs for specified ranges of misorientation angles were also created from each microstructure to aide in visualizing the texture present from these special boundaries, shown in Figure 34. Three sections were chosen at random for each microstructure to have enough data for clearly showing texture, while not oversaturating the IPFs with data points. The IPF plots confirm strong texture towards the axis/angle misorientations within Brandon's criterion for Σ3 and Σ9 twin ranges for the HT and FR specimens, while the AR specimens only show texture for the Σ3 twin range.

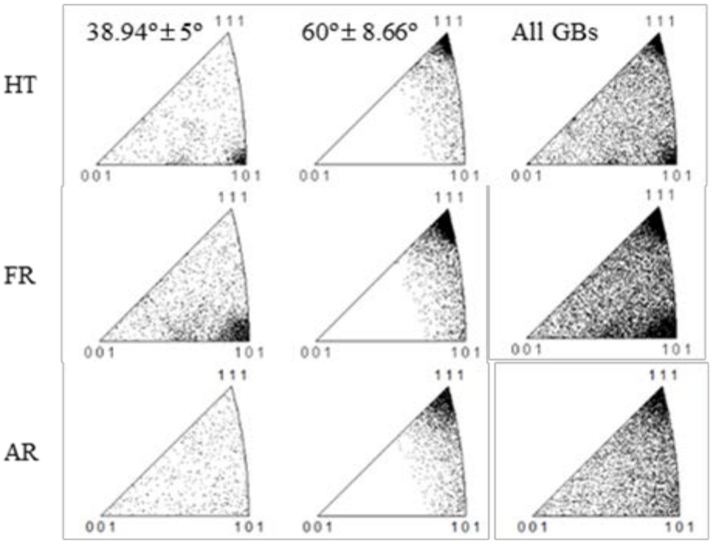

Figure 34: IPF plots of the axis/angle misorientations for 3 random sections for each microstructure, corresponding to (from left to right); Σ9 range, Σ3 range, and all boundaries [23]. The Σ9 and Σ3 misorientation ranges are from Brandon's criterion [87].

To further examine the texture in the specimens *P(θ)* was compared to the MacKenzie distribution [89] for a polycrystalline cubic material with a random crystallographic texture in Figure 35a. Note that the MacKenzie distribution itself peaks in the 45° to 50° misorientation bin and begins its descent to zero density thereafter, whereas the distribution of GBs in all samples lay well below the predictive MacKenzie curve until the large spike of the 55° to 65° range, indicative of Σ3 twin boundaries.

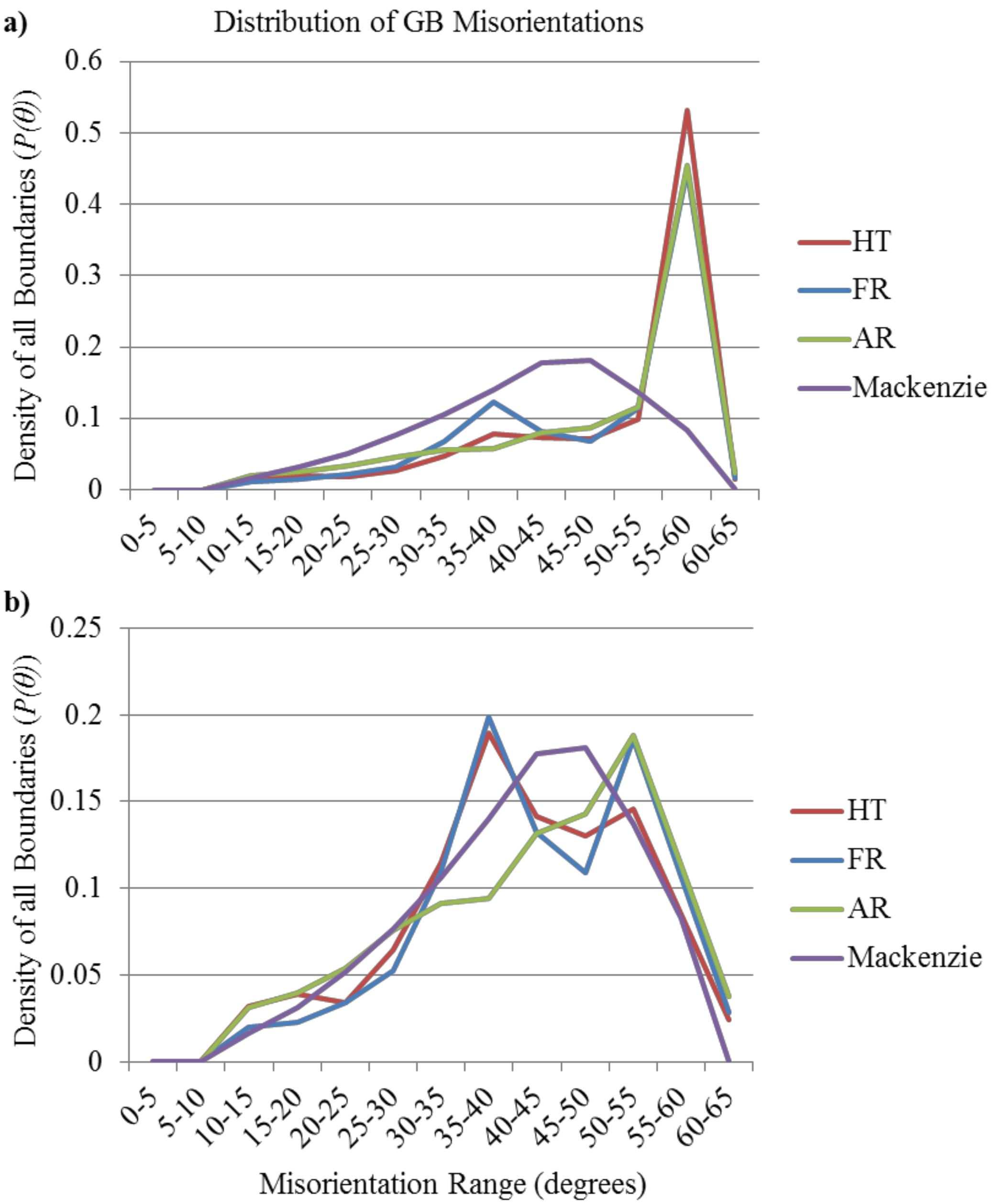

Figure 35: a) Distribution of all GBs for each microstructure compared to the MacKenzie distribution. b) Distribution of all GBs with the 55° to 60° removed, averaged and compared to the MacKenzie Distribution. There is a horizontal error of ±5° for all data.

Figure 35b shows how the crystallographic texture compares to the MacKenzie distribution when the 55° to 60° misorientation bin is taken as an average of the 50° to 55° and 60° to 65° bins to remove the influence of most the Σ3 twin boundaries. The AR specimens appears to show a random texture following the MacKenzie distribution with a slight shift to the right, indicating that the Σ3 boundaries present in the 50° to 55°, as allowed per Brandon's criterion, are still skewing the randomness of the texture. Both the FR and HT specimens show a similar spike in the 35° to 40° bin range due to the presence of Σ9 annealing twins. However, the FR specimen contains a similar spike as the AR specimens in the 50° to 55° Σ3 range, whereas the HT specimen appears to follow the MacKenzie distribution.

All three microstructures under-predict the presence of boundaries in the 40° to 50° range, corresponding to random high angle GB range and where the MacKenzie distributions peaks. This is likely due to the presence of the remaining Σ3 twin boundaries in the 50° to 55° range for the AR and FR specimens and the presence of Σ9 annealing twins in the HT and FR specimens. These results are similar to previous texture analysis results from statistical studies done by Hashemian [17] and Wayne [18]. Note that not all boundaries within these 60° misorientation ranges are necessarily twins or CSLs and may be random high angle GBs, but all twins are CSLs. It is also important to note that in Escobedo et al. [15], the overall CSL fraction of the specimens examined was ~0.7, much higher than the fractions reported here in Table 4. The reduction in texture presented in this work allows for more statistics to be gathered from the random high angle GBs to be compared to the well documented special GBs.

Once the crystallographic texture was determined the focus shifted to the primary goal of the statistical study: determining misorientation ranges containing damage and the probability to find damage given a misorientation angle. All boundaries that clearly contained damage were counted and placed into the same bins used using the same method as with *P(θ)*, which placed all GBs within the spall zone into bins. If damage existed at a triple junction, for example, then the misorientations across all three shared boundaries were counted. It is important to point out that with 2-D statistics it is impossible to determine the damage nucleation point, even when the damage is mostly smaller than the average grain size, because one may be probing the beginning or end of a void through the thickness. The only way to have the best possible idea of where a void nucleated within the microstructure is to have 3-D reconstructions of the microstructure and the spall plane, both of which are discussed later in this work, but not directly pertaining to GB damage statistics. Again, the purpose of this statistical study is to know the probability of finding damage at a GB of a given misorientation within the microstructure.

After collecting the misorientations of GBs containing damage and placing the data into their respective bins, each bin was divided by the total number of damaged boundaries to find $(\theta|X=1)$. $P(\theta|X=1)$ is the probability to have damage at a misorientation angle given that there is damage at the boundary, or, simply, the density of damaged boundaries. $P(\theta|X=1)$ is shown in Figure 36 for all three microstructures.

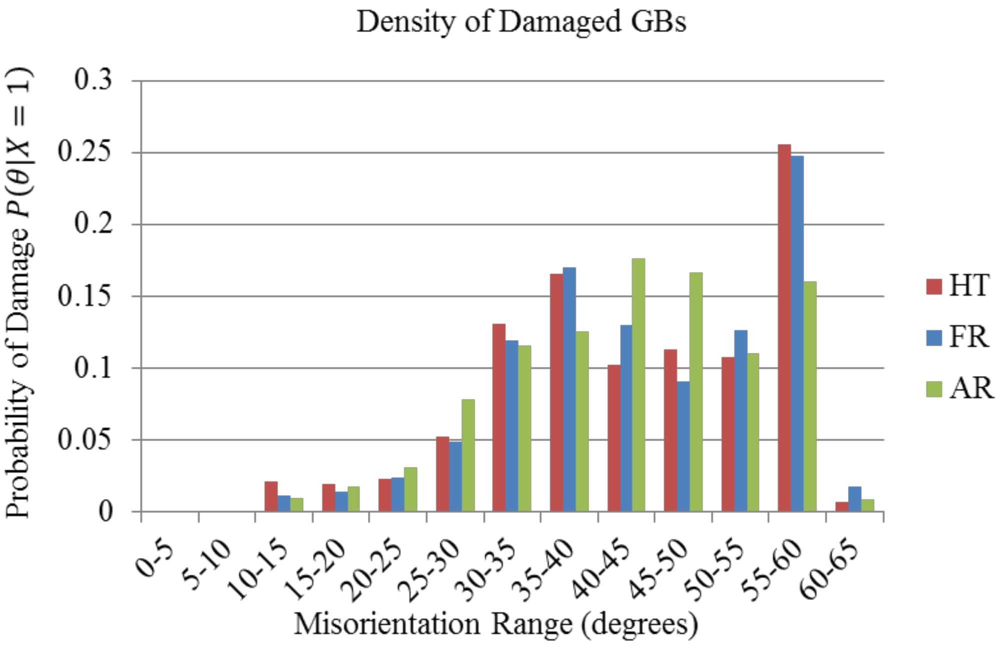

Figure 36: Density of damaged boundaries, $P(\theta|X = 1)$ [23]. There is a horizontal error of ±5° for all data.

Figure 36 shows an abundance of 60° misorientation GBs containing damage, which goes against the now common wisdom that Σ3 boundaries are strong due to their low energy configuration [90]. As it was pointed out earlier, some of these boundaries are likely to be random high angle boundaries, and with the texture of the materials being skewed towards this misorientation angle range there are bound to be many non Σ3 boundaries within this bin range that would not be particularly strong along with possible transgranular damage that grew or coalesced towards GBs. It can be seen from $P(\theta|X = 1)$ that the density of damage at boundaries in the {110} Σ9 annealing twin range is higher in the HT and FR specimens, where such boundaries were shown to be more prominent. The behaviors of all three microstructures also mimic the trends from the

MacKenzie plots in Figure 34; the AR specimen has the least amount of counts in the 55° to 60° Σ3 misorientation range and a higher number of counts of damage at random high energy boundaries in the 40° to 50° misorientation range. From all of the above observations it becomes obvious that taking into account the crystallographic texture of the specimens to correctly determine the probability of finding misorientation angle containing damage, $P(X=1|\theta)$, as shown previously in Section 5.2, eq. 21 and by Wayne [18, 20], is of paramount importance for meaningful conclusions on boundary strength.

To elaborate on GB strength, there exists a correlation between misorientation angle and the nucleation energy required for void formation at a boundary: the critical free energy change for void formation at a boundary decreases proportionally with increasing GB energy due to the fact that the total GB area decreases upon void growth [91]. Less nucleation energy is required for void formation at boundaries with higher misorientation angles because GB energy increases with misorientation angle [92]. It has been reported that 68 random high angle boundaries exist that have high boundary diffusivities and are considered mechanically weaker due to their higher interfacial energies [90, 93]. These boundaries are more disordered and contain more free volume, thus having higher diffusivities and energy association to them than a coherent twin boundary on the {111} plane which has a high misorientation (60°), but low diffusivity and low energy association because the atoms at the boundary are undistorted in the lattice [92-94]. Dislocation transmission and/or activation of secondary slip are satisfied by Σ3 boundaries, providing a mechanism to lessen stress concentrations at the boundary

[21]. Thus lies the explanation as to why the {111} Σ3 twin boundary is more resistant to damage and is supported by the data presented in this study.

Normalizing the data to the material's texture was performed by calculating $P(X = 1|\theta)$, conducting a shape distribution analysis, and applying propagation of error to find the total error of $P(X = 1|\theta)$. Figure 37 shows the corrected probability of finding a misorientation angle containing damage among all boundaries present in the spall region with vertical error bars for each microstructure analyzed. This figure indicates that the overall shape of the histograms peak around the 30° to 35° range in the HT and FR specimens, but other modal peaks between bins are suspect; however, the general trend even with the presence of the error bars indicates a preference to the 25° to 50° random high energy boundary range with the Σ3 twins and low angle GBs tending to be stronger, *i.e.*, they have a lower probability of having damage. The AR specimens have less error and possess a very pronounced peak between the 25° to 50° range, suggesting that these boundaries are microstructurally weaker than others, in full agreement with the quantitative and qualitative conclusions from [20, 22].

The magnitude of the probabilities to find damage in the HT microstructure is approximately doubled across every bin when compared to the FR and AR microstructures. The HT specimen, sample 20357, had the highest P_{max} of the analyzed samples, so this increase in global damage probability is to be expected. Given that there is a higher amount of damage in the sample, there appears to be little influence on the shape of the distribution in Figure 36 when compared to the fellow annealed FR sample.

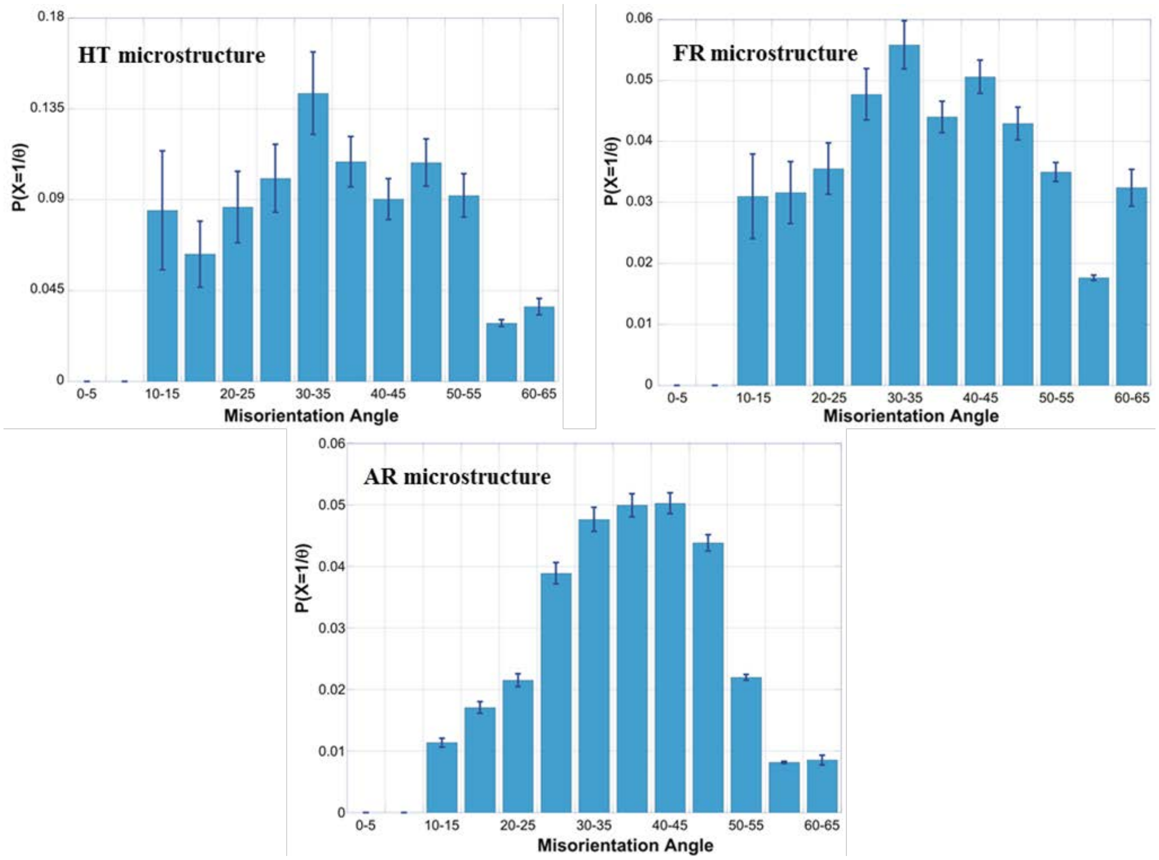

Figure 37: Probabilities of finding a misorientation angle, θ, containing damage among all boundaries in the selected spall region [23]. There is a horizontal error of ±5° for all data.

The removal of plastic deformation in the grains via heat treatments creates less of a preference toward intergranular void nucleation, and the results from Figure 37 indicate that misorientation angle also has a decreased influence on GB damage, but still with a higher probability towards finding damage at misorientations in the 25° to 50°. These observations strongly suggest that when heat treated copper PCs are subjected to shock loading finding damage along the spall plane has less regard of the local microstructure as compared to the pre-strained specimens, with the possible exception of

Σ3 twin boundaries, in agreement with [15, 20, 22]. The small grain size coupled with mixed modes of inter- and transgranular void nucleation is a likely explanation for the increased probability of damage found at GBs in the 60° to 65° range for the FR specimen. The other reason behind this spike, as well as the larger error bars and higher magnitude of damage in the low angle 10° to 15° range is that during the normalization process and error analysis there is a degree of uncertainty that arises with low counts of data points as compared to the rest of the data set. Misorientation angles less than 15° were the least common within the microstructure, $P(\theta)$, as well as the density of damaged boundaries, $P(\theta|X=1)$.

Escobedo et al. [15] claimed that voids did not nucleate at special Σ1 and Σ3 boundaries, in agreement with the overall trends reported earlier by Wayne et al. [20], later by Brown et al. et al. [22], and with the results here. However, the results here show that it is possible for voids to exist at low angle grain boundaries and Σ3 twin boundaries, although it is less likely than for other misorientation angles. This can be attributed to spall opening up within a grain and propagating towards a GB or from the material responding to a hydrostatic stress state high enough to open a free surface regardless of the local microstructure, the latter of which is suggested by the HT and FR data shown in Figure 37. Another point not mentioned in previous work [15], but reported by [20, 22] and found here, is that damage may occur at the tips of annealing twins, or, terminated twins. These boundaries are likely not {111}, resulting in a higher energy boundary as previously discussed, thus more susceptible to localizing damage.

It is important to reemphasize the methodology of counting all the GBs within the defined spall plane and its impact on the magnitudes of the final probabilities obtained to find a misorientation angle with damage. Referring back to Figure 9b in Chapter 2, it was seen in Wayne [20] that the highest probability misorientation bin to find damage was 35° to 40° with a probability of just over 45%. Reevaluating the same EBSD scans confirmed the 1,164 damage sites; however, only 730 GBs were previously used for the compilation of the global microstructure, $P(\theta)$ [20]. Having less counts for the representative microstructure than the damaged boundaries lead to a significant over prediction of the probability for a misorientation angle to contain damage due to the multiplication of $P(X = 1)$ in eq. 21 to find $P(X = 1|\theta)$. In the work presented here, the total number of GBs examined from the 27 through section EBSD scans cropped to show only the spall plane was 50,438. Thus, the actual probability of finding a misorientation angle with damage was found to be from 1% to 5%, as shown in Figure 37 for the AR microstructure, compared to ~10% to 45% in Wayne [20]. Note that the general shape of the distributions remain similar; damage is more likely for random high angle GBs in the misorientation range of 25° to 50°, confirming the previous work by Wayne [20] to hold as a proof of principle for the work presented here.

It has been established that 25° to 50° is the preferred misorientation range for GBs to contain damage regardless of the material’s thermomechanical history, but becomes more prevalent with an existing plastic pre-strain. Removal of this pre-strain via heat treatments changes the damage mode from primarily intergranular to a mixed mode of inter- and transgranular damage, lessening the preference for damage to occur at these random high angle GBs. Though 60° Σ3 twin boundaries remain statistically strong damage sites were found at these boundaries for the HT and FR specimens, further strengthening the argument that local microstructure has a lessened effect for these materials.

It is of interest to investigate the extent of inter- vs. transgranular damage presence for each microstructure to complement the data reported from 2-D statistics. Does the damage mode drastically change for each microstructure as expected? 3-D reconstructions of the spall plane were conducted to answer this question and are presented in the following sections.

6.2 3-D X-ray Tomography of Spall Damage in Polycrystals

Although 2-D studies are adequate for statistics on where damage is found within the microstructure, it is of interest to quantify the amount of inter- and transgranular damage present within the shock-loaded samples. 3-D data are needed to characterize the shapes of individual damage sites within the spall plane of samples with varying microstructures. The resolution obtained from mechanical polishing is too inconsistent to accurately reconstruct the proper shapes of voids found through the thickness, thus 3-D XRT was used for these studies. It is hypothesized that a strong distribution of spherical voids is indicative of dominant transgranular damage, as voids tend to open as octahedra in single crystals [66]. “Needle” and “sheet-like,” or, “disc-shaped” voids are hypothesized to be indicative of intergranular damage and/or coalescence. The more a void closely resembles a thin sheet, or disc, the more likely that void is following the curvature of a GB through the thickness of the material.

After going through smoothing, segmentation, thresholding, and volumetric sieving procedures, void volume statistics were analyzed from the from the 3-D XRT data. Table 5 shows these volumetric data for each sample analyzed. Note that the total void volume and the spall zone volume fraction listed in Table 5 are the only values that include voids that share nodes with the perimeter of the dataset to correctly account for all voids that meet the 120 and 1000 voxel minimums for accurate volume rendering for samples 20375 (AR), 20366 (FR), 20354 (HT), and 20355 (HT). Neither of the HT samples analyzed in detail here are the same sample analyzed for the 2-D sectioning, 20357, for a couple reasons: 20357 was largely destroyed in the process of collecting statistics and the exhumed section that was used for XRT was closer to the edge of the spall plane than anticipated. The outermost regions of the spall plane may contain voids unrepresentative of the uniform central spall region due to intrinsic momentum trap effects from the geometry of the impact experiment [19]. A benefit of using 20354 and 20355 for the XRT study was that the maximum pressures were more in line with the AR and FR samples analyzed (refer to Table 2).

Sample 20375 contained a high level of noise in the XRT data on half of the data set that was impossible to threshold out and sieve properly without affecting the volumetric statistics. Entries in Table 5 reflect the volumes from each dataset, which represent varying fractions of the total spall plane of each exhumed section, with the exception of 20366. Thus, the total void volume fraction and spall plane void volume fractions reflect the information available from the analyzed data sets, not the size of the entire sample or the entire spall plane within the sample. Due to the uniformity of the spall planes in all samples, it is an adequate assumption that these fractions are representative of the entire spall zones throughout the target plates. The nearest neighbor distance (NND) refers to the distance between the centroids of voids within the specimen.

Table 5: Volumetric void data obtained from 3-D XRT with a minimum volume of 120 voxels for samples 20375 and 20366 and 1000 voxels for samples 20354 and 20355.

Sample # / Microstructure	20375 / AR	20366 / FR	20354 / HT	20355 / HT
Number of Voids	817	2198	533	686
Total Void Volume	8.496×10^7	1.432×10^8	2.766×10^6	2.576×10^6
Av. Void Volume (μm^3)	1.039×10^5	6.513×10^4	5.189×10^3	3.754×10^3
Median Volume (μm^3)	1.481×10^4	1.917×10^4	2.372×10^3	2.473×10^3
Av. Equivalent Radius (μm)	19.73	19.49	9.609	9.316
Median Equiv. Radius (μm)	15.23	16.60	8.242	8.382
Average NND (μm)	106.2	83.24	40.11	44.89
Median NND (μm)	96.29	78.56	36.13	39.145
Minimum NND (μm)	32.39	25.59	17.78	16.25
Maximum NND (μm)	420.2	327.8	174.9	150.1
Spall Zone Volume (μm^3)	8.410×10^8	7.984×10^8	1.547×10^8	1.211×10^8
Total Section Volume (μm^3)	2.056×10^9	3.622×10^9	5.226×10^8	3.35×10^8
Spall Zone Vol. / Section Vol.	0.4091	0.2205	0.2960	0.3615
Total Void Volume Fraction	0.0413	0.0395	0.0053	0.0077
Spall Zone Void Vol. Fract.	0.1010	0.1793	0.0179	0.0213

The voids present in the HT specimens are the smallest on average of the three specimens and appear to be the most incipiently spalled, as the total volume fraction and the spall zone volume fraction voids are noticeably the smallest. Note that the equivalent void radii are simply the size of spheres fit to the volumes of the voids. The AR and FR specimens have similar average void sizes, but the AR specimen has a much thicker spall zone as compared to the FR specimen with spall zone volume fractions of 0.4091 and 0.2205, respectively. This spread in the presence of voids along the shock direction in the AR specimen indicates that voids are likely nucleating at mechanically weak locations within the microstructure, *i.e.*, GBs, rather than confined to nucleating within the approximately 1-D spall plane as with the FR and HT specimens. The large volume of the spall plane in the HT specimen, 20355, stems from noticeable individual voids decorating the outermost regions of the uniform spall plane with respect to the shock direction rather than the global thickness of the AR specimen. The AR specimen also has the largest average NND and a similar grain size to that of the HT specimens, which have a much lower value for NND. This suggests that the HT specimens contain predominantly transgranular damage while the AR specimen contains primarily intergranular damage.

Although the NND is a good indicator for inter- vs. transgranular damage when compared to the average grain size, the FR specimen shows that this has flaws. The NND for the FR specimen is larger than the average grain size by about 60%. Investigating the XRT renderings elucidates that the damage present in the FR specimen is largely coalesced, indicative of a large amount of long, needle-like voids as well as oblate and prolate ellipsoids. When many smaller voids coalesce to form larger volume damage sites there will be an increase in centroid distances between neighboring voids on average; before coalescence there would be many small NNDs, but after there would only be the distance between larger volume voids that are likely more spread out. Figures 38b and 39b show renderings of the spall plane in the FR specimen.

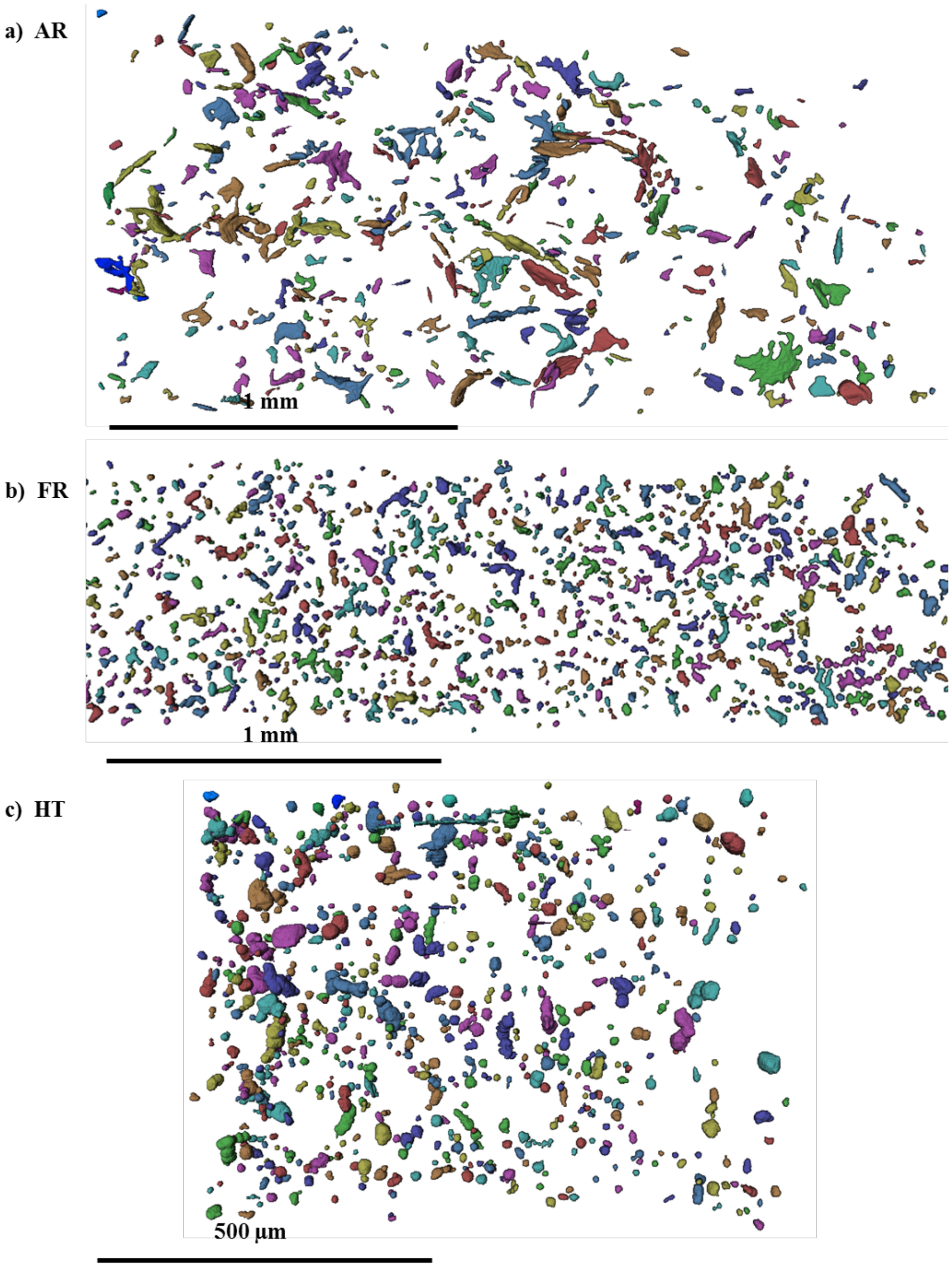

Figure 38: 3-D renderings of the spall planes with a 1,000 voxel sieve in the three studied microstructures, with the shock direction out of the plane. The sample shown in c) is 20354. Void colors are for visual aide only.

The volume statistics point towards predominant intergranular damage in the AR specimen, transgranular damage in the HT specimens, and mixed mode damage in the FR specimen, according to the hypotheses formulated above. Figure 38 shows a top-down view (shock direction out of the page) of the voids in each microstructure and Figures 39 and 40 show through-thickness views (shock indicated by the red arrows) of the voids in each sample for visual verification of the damage modes present.

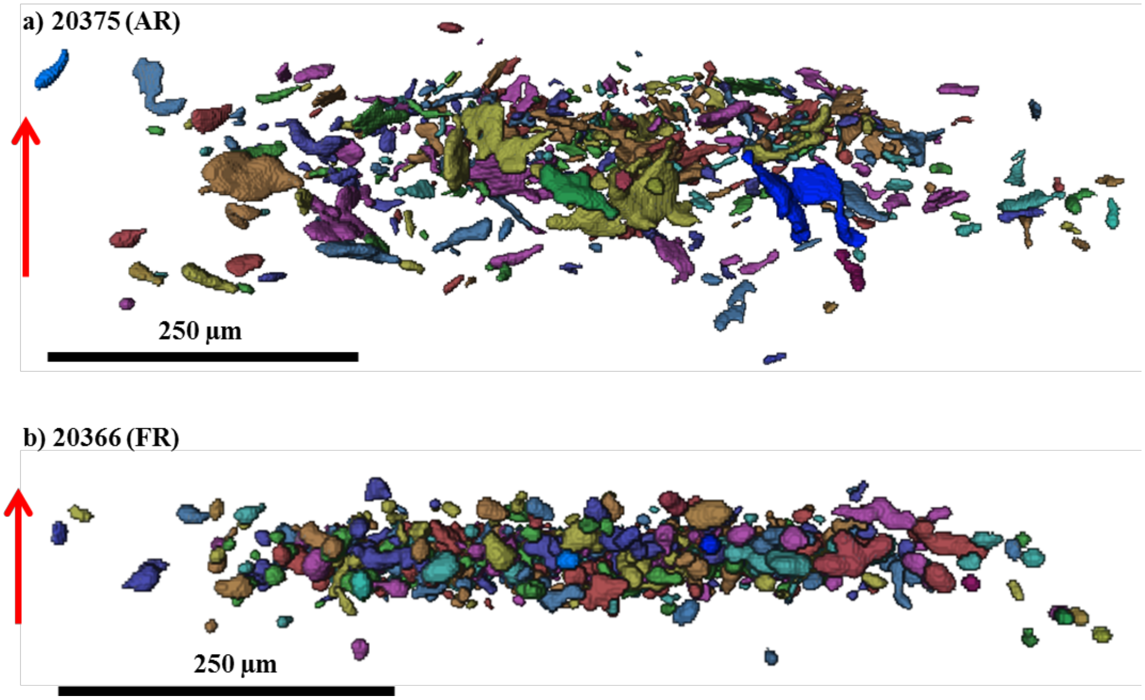

Figure 39: 3-D renderings of the spall planes with a 1,000 voxel sieve and the shock direction indicated by the red arrows in samples a) 20375 and b) 20355. Void colors are for visual aide only.

In Figure 38, drastic differences in the void shape distribution are seen for all three microstructures. Qualitatively, it can be seen that the AR sample in Figure 38a and 39a has a high concentration of disk- and needle-shaped voids, which is indicative of intergranular damage and void coalescence. Visual inspection of the spall plane in both 2-D and 3-D makes it clear that the majority of the voids appear to have curvature that would follow GBs through the thickness of the sample. The oblong, needle shaped density may have come from coalescence, but possibly from damage along triple junctions through the thickness.

In Figures 38b and 39b, there appears to be a larger spread of void shapes for the FR microstructure; however, they appear to be predominately needle and spherical-shaped voids with very few sheet-like voids. This indicates that there is mainly transgranular damage and coalescence present. Reviewing the 2-D and 3-D data sets, there is an apparent mixed mode of inter- and transgranular damage, but the FR microstructure has an average void size that approaches the average grain size of the material. This similarity in size between the grains and voids results in less clear definition between intergranular damage vs. damage that happens to be present at a boundary and making it known that the spall plane in this specimen is more coalesced than incipient, which must be considered when drawing conclusions from the 2-D statistics presented in the previous section.

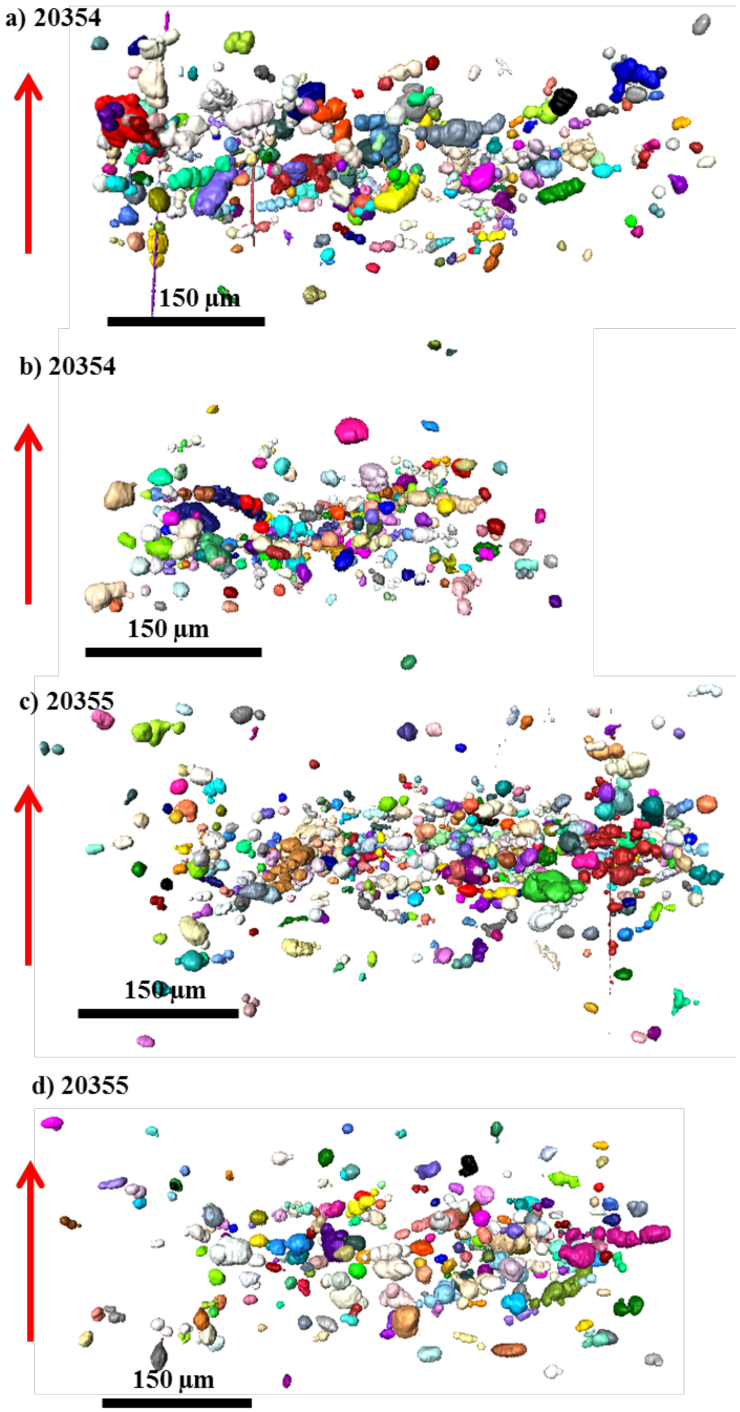

Figure 40: 3-D renderings of the spall planes in samples 20354 and 20355 with a 1,000 voxel sieve and the shock direction indicated by the red arrows. Void colors are for visual aide only.

Figures 38c and 40 shows there is a heavy skew towards spherical-shaped voids in the HT sample, matching 2-D OM and EBSD data showing transgranular damage scattered throughout the spall plane with few damage sites being blatantly intergranular. From the EBSD scans, many voids that were present at the boundaries appeared to be spherical or ellipsoidal, as opposed to elongated and flattened along the GB, indicative of the damage nucleating at that spot regardless of the local microstructure. In Figure 40 it is clear that the larger voids are typically elongated ellipsoids with a “beaded” surface texture, indicative of void coalescence, while the bulk of the voids appear to mimic spheres or octahedron, indicative of transgranular damage.

When comparing the qualitative 3-D renderings of the void shapes with the 2-D statistics of voids present at boundaries, it becomes clear that the AR microstructure not only has preferential nucleation of damage at GBs, but also has a pronounced preference to nucleate damage at weaker, random high angle, high energy GBs. The decrease in probability of finding damage at GBs of misorientations of 25° to 50° for the FR and HT microstructures is clearer upon seeing the heavily coalesced damage in the FR specimen and the largely spherical, transgranular shaped voids in the HT specimen from the 3-D XRT renderings. In order to produce more quantitative results on the amount of inter- vs. transgranular damage present in each microstructure it is necessary to fit individual voids in the spall plane to best fit ellipsoids, from which plots of the aspect ratios will provide insight into the concentrations of void shapes present.

6.2.1 Shape Fitting Voids to Ellipsoids from Surface Nodes

In an attempt to quantify the amount of inter vs. transgranular damage present within each sample an algorithm was written to solve for the semi-axes of the best fit ellipsoid for each void in a given dataset using surface nodes. After solving for the best-fit semi-axes the resulting ratios of a/c and b/c, where c ≥ b ≥ a, are plotted against each other to visualize the distribution of void shapes within the specimen, as shown below in Figure 41.

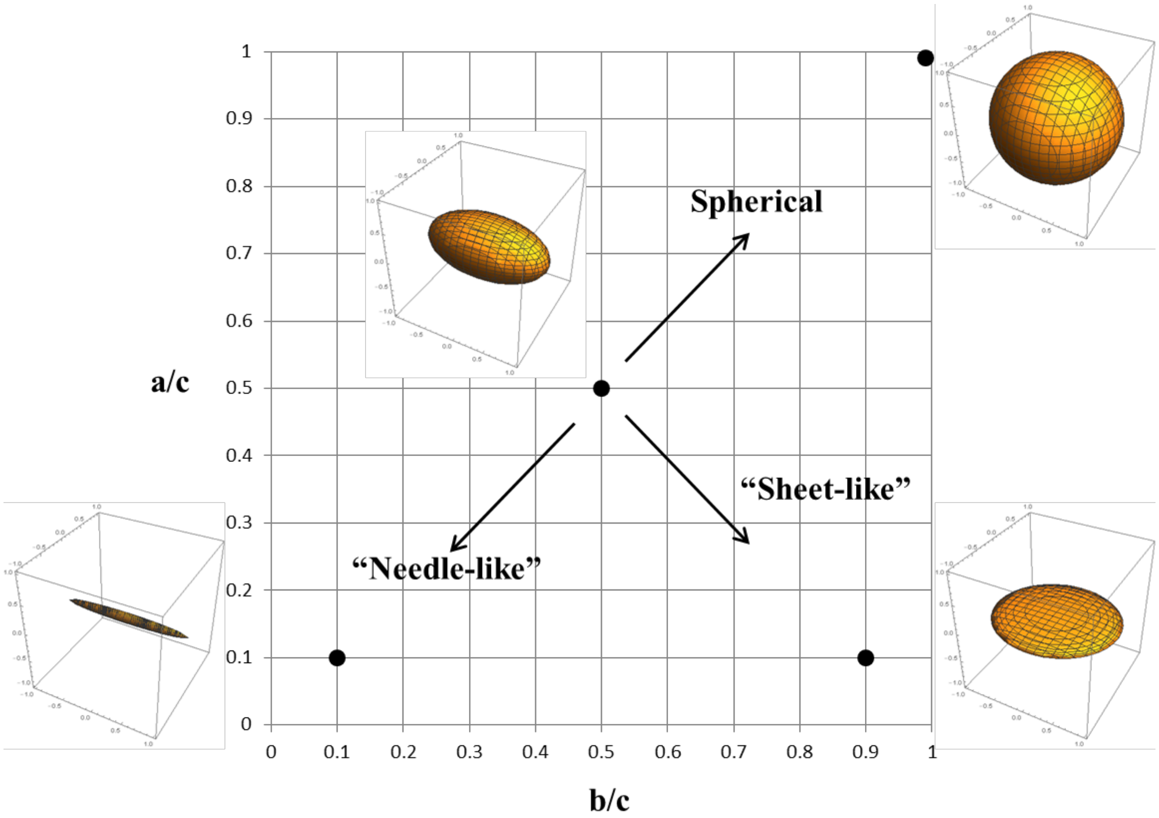

Figure 41: The shape domains are shown for the ratios of best-fit ellipsoid semi-axes a/c vs. b/c. The arrows indicate how the shape of the fitted ellipsoid changes with differing semi-axes ratios.

If a ≈ b ≈ c, the ellipsoid shape becomes spherical, if c >> b ≈ a, the ellipsoid shape becomes "needle-like," and when b ≈ c >> a, the ellipsoid becomes "sheet," or, "disc-like." Ellipsoids represented by oblate and prolate shapes vary at ratios near a/c ≈ b/c ≈ 0.5 are likely indicative of two coalesced voids and is indicated as a point of reference in Figure 41. As a/c and b/c approach 1 together from this point of reference, the probability of the ellipsoid representing an elongated, and eventually spherical, transgranular void increases. As a/c decreases and b/c increases it becomes likely the ellipsoid represents an intergranular damage site following a GB and as a/c and b/c decrease together towards 0, it becomes likely that the ellipsoid represents an increasing amount of coalesced voids or follows a triple point.

After testing the algorithm on individual voids representative of a spherical, needle-like, and a disc-like ellipsoid, it was run for every void in samples 20375 and 20366 with a sieve of 1,000 voxels for accurate volume representation. At this sieve 20375 contained 458 unique damage sites and 20366 contained 1,275 sites. Ellipsoidal solutions were found for 376 voids in sample 20375 (~82%) and 929 for sample 20366 (~73%). Solutions without a fit were obvious because one or more of the solved semi-axes contained an imaginary component. Many other void solutions contained three negative eigenvalues for the solution to the eigen problem in eq. 33, leading to incorrect values when solving for the semi-axes, where it is expected to find only two negative eigenvalues [84]. The resulting fits for the ellipsoidal semi-axes are plotted in Figure 42.

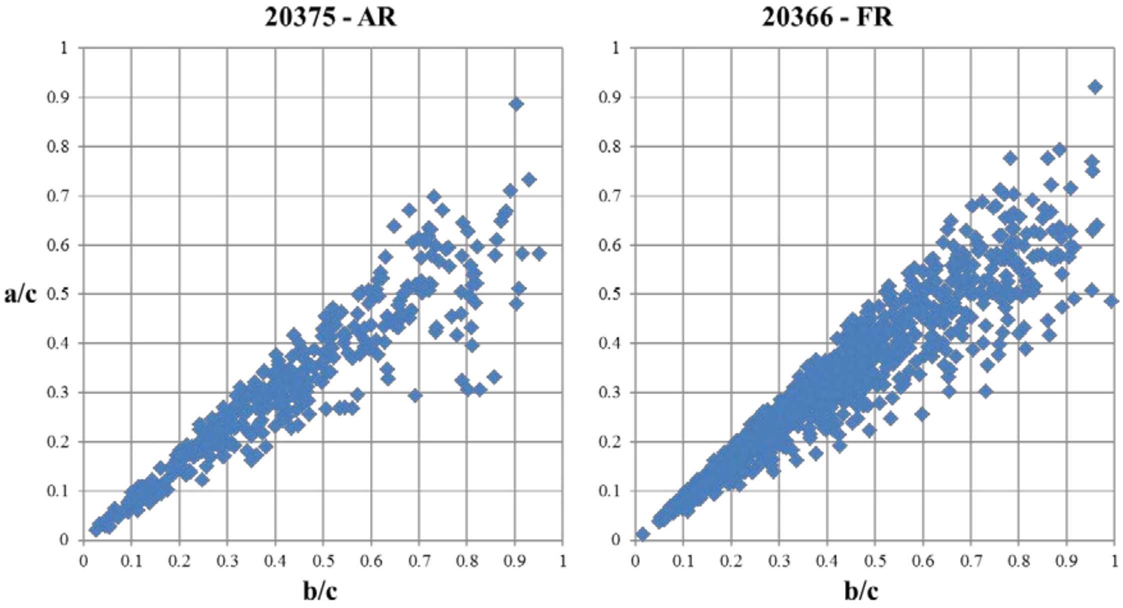

Figure 42: Plot of the best fit ellipsoid semi-axes ratios a/c vs. b/c where c > b > a for samples 20375 (left) and 20366 (right). Both plots show sparse data points where spherical and sheet-like ellipsoids would expect to be found and heavy concentrations of oblate to needle-shaped ellipsoids.

The data in Figure 41 suggests that there is dominant void coalescence and damage at triple boundaries within the spall plane for both microstructures. From visual inspection of the XRT renderings in Figures 37 and 38 it is expected that the aspect ratio plot would show a heavier lean towards sheet-like ellipsoids for the AR specimen, where intergranular damage is known to dominate. The coalescence dominance in the FR microstructure is not out of the question, but the convergence to the c >> b ≈ c, or, a/c ≈ b/c ≈ 0.1, region is intriguing. There shouldn't be many voids representative of such an oblong, needle-like structure, which would be unphysical even for many small voids coalesced. The divergent conic shape of the data from (0,0) to (1,1) is also of concern, as it appears the algorithm is failing at some point during the ellipsoidal family check process.

The algorithm works fine for individual voids that are spherical or slightly oblate or prolate in nature, refer to Figure 31, however, there is a breakdown in the ability to solve the governing constraint of $\alpha J - I^2 > 0$ to the generalized quadric surface represented in eq. 23 when coalesced or intergranular voids take on abnormal curvatures. A quadric may be fit to any set of 3-D nodes; however, this is not the case for an ellipsoid. There are many voids with curvature from either being intergranular damage or containing many coalesced voids that do not follow straight semi-axes, like the ones in an ellipsoid. Another method is needed to more accurately obtain the information required for obtaining globally correct fits from the XRT data.

A better solution for finding a best fit shape for a 3-D volumetric object is to probe not only the surface nodes, but also incremental volume elements radially from the centroid to the surface to account for irregular shapes and curvature. One way to do this is to use the inertia tensor of each void as a baseline for fitting an ellipsoid. Inertia takes into account the object's resistance to rotation along a specified direction. If the principal inertias are investigated then said axes will belong to the local coordinate system of each void providing the ability to fit each void without the constraints of the surface nodes. The results from using the inertias to fit voids to a representative ellipsoid are discussed in the next section.

6.2.2 Shape Fitting of Voids to Ellipsoids from Inertia Tensors

Using the inertia tensor of a 3-D object to fit an ellipsoid based on the principal moments of inertia of that object is a way to guarantee that the shape of the object is always fit with regards to that object's resistance to bending in each principal direction. The resulting ellipsoid will always have the same principal inertias as the physical object, thus the shapes of the fit and the object cannot drastically differ even if there is curvature involved in one or more directions. This is an inherent improvement from relying on the surface nodes to fit an object, as this method will always have a fitted solution for an object.

As described in Section 5.5.2, the method by which Avizo^{TM} determines the inertia tensor of an object is slightly different from what one might expect with the relationships between the principal inertias and an ellipsoid's semi-axes being dependent on only one term (eqs. 49-51). There is a mass term in these relationships that is unknown from the XRT data, and, of course, the voids themselves are massless. This becomes a nonissue, as the expressions of interest are the ratios of the ellipsoidal semi-axes, a/c and b/c. The ellipsoid fitting procedure was carried out for all the samples with XRT data and the results are plotted in Figure 43.

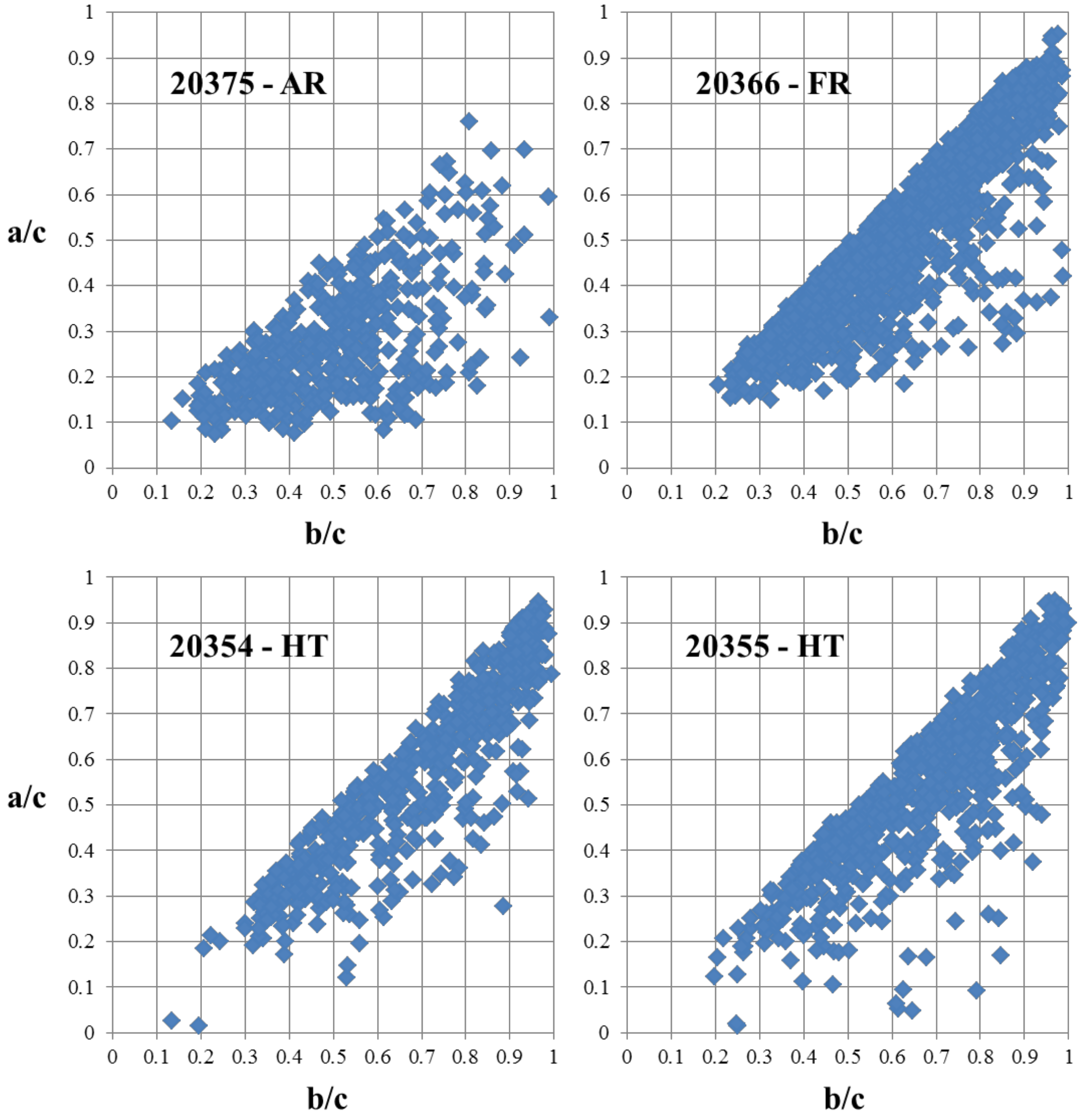

Figure 43: Plot of the best fit using inertia tensors for ellipsoid semi-axes ratios a/c vs. b/c where c > b > a for samples 20375, 20366, 20354, and 20355, clockwise from the top left.

The results in Figure 43 support the conclusions based on the qualitative shape analysis of the spall damage present in each microstructure. The AR specimen shows a concentration of voids representative of coalesced and sheet-like ellipsoids, the latter indicating intergranular damage, whereas the FR and HT specimens appear to have concentrations of voids in the coalescence and spherical regimes, indicative of transgranular damage. All the voids present in the 1,000 voxel sieve are captured in the data shown in Figure 43; however, it is difficult to tell where the clusters of data points maximize in count and the physical shapes of ellipsoids in these regions. Figures 44-46 aim to illustrate the physical shapes of voids with the highest count in each sample.

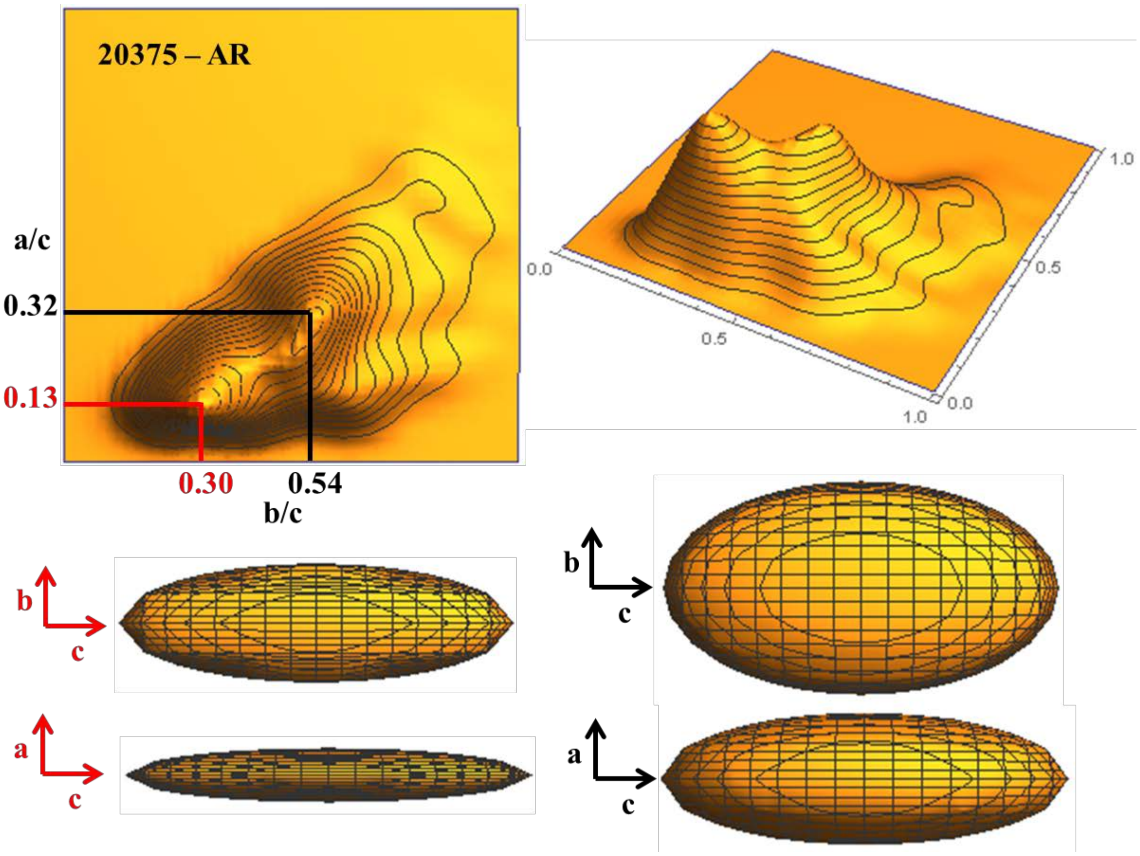

Figure 44: Contour plots of the best fit ellipsoid semi-axes ratios a/c vs. b/c where c > b > a for sample 20375. The colors of the maximum aspect ratio count peaks correspond to the fitted ellipsoids with semi-axes coordinate systems of the same color.

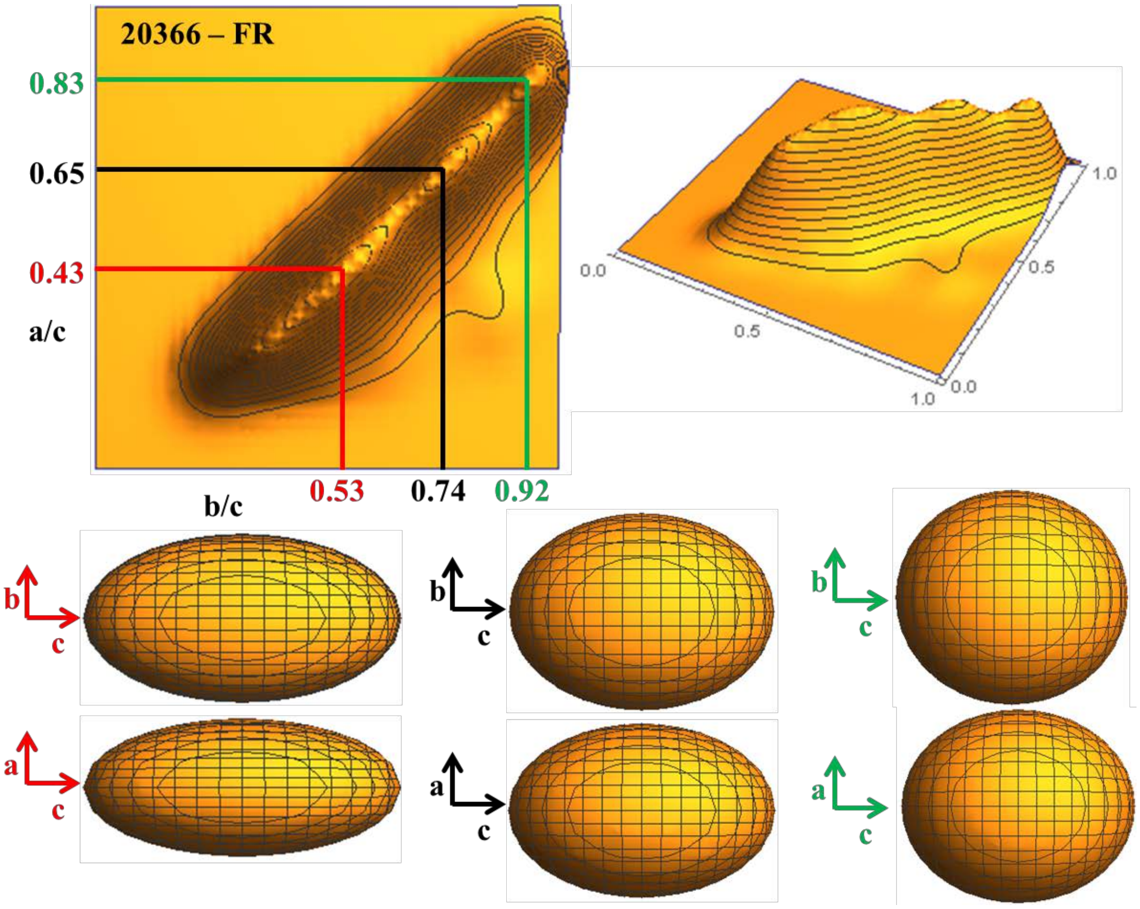

Figure 45: Contour plots of the best fit ellipsoid semi-axes ratios a/c vs. b/c where c > b > a for sample 20376. The colors of the maximum aspect ratio count peaks correspond to the fitted ellipsoids with semi-axes coordinate systems of the same color.

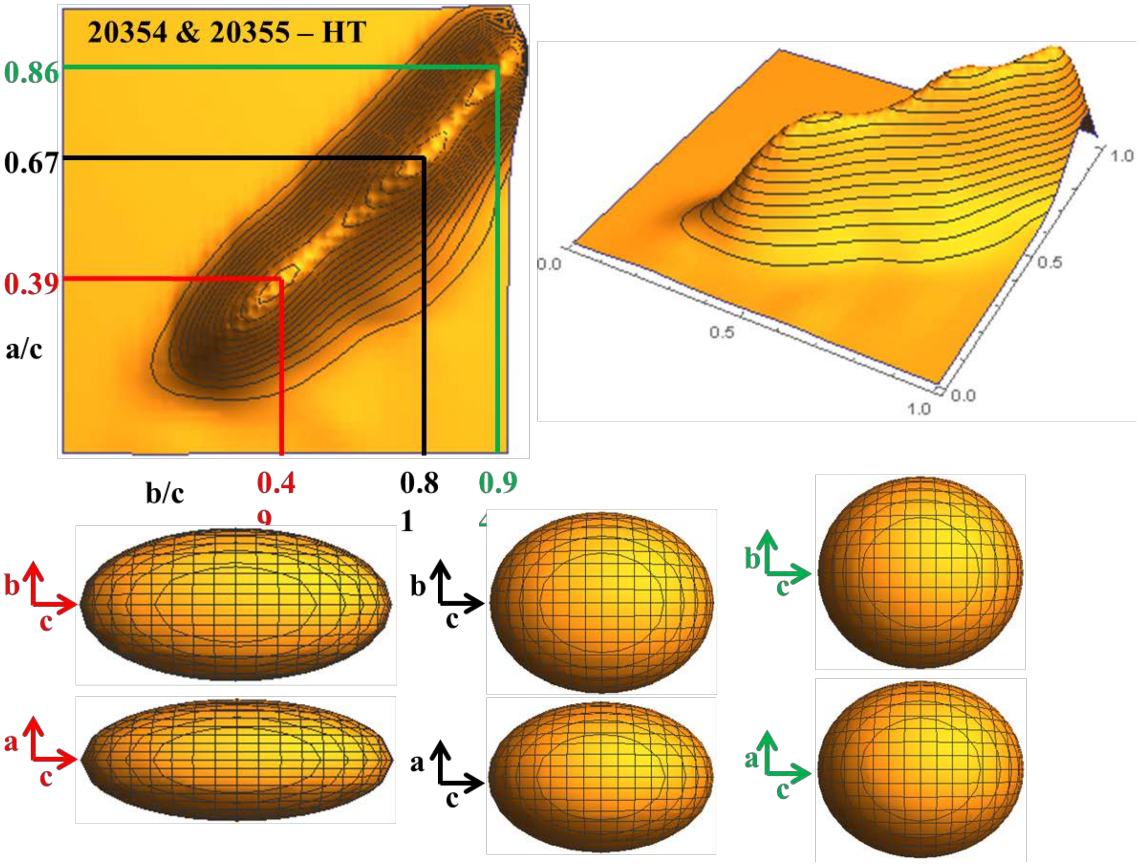

Figure 46: Contour plots of the best fit ellipsoid semi-axes ratios a/c vs. b/c where c > b > a for samples 20354 and 20355. The colors of the maximum aspect ratio count peaks correspond to the fitted ellipsoids with semi-axes coordinate systems of the same color.

In Figure 44 the AR microstructure clearly shows an almost complete lack of spherical shaped voids with high concentrations of ellipsoid shapes with aspect ratios of under 0.5 for both a/c and b/c. For aspect ratios of a/c and b/c both greater than 0.5, there are only 32 data points, or 7% of the total sample size. Under the hypotheses used here, it can be estimated that there is less than 7% transgranular damage present in the sample, with the actual value being less than this because there are regions in this zone that are likely two coalesced spherical shaped voids. There are peaks on the contour plots for a/c and b/c aspect ratios of 0.13 and 0.30 and 0.32 and 0.54, respectively. There are 158 data points in the area between these two points, $0.32 \geq a/c \geq 0.13$ and $0.54 \geq b/c \geq 0.30$, accounting for 34.6% of the voids in the dataset. Most of the voids in this region are going to be either coalesced or intergranular damage, indicative of the ellipsoid shape found at either bound of this area. The region defined by a/c less than 0.32 and b/c greater than 0.54 contains voids that are ideally sheet-like in structure for which there are 78 data points, accounting for 17.1% of the voids in the dataset. Regions for which ellipsoids are representative of intergranular damage (sheets) account for ~55% of the entire dataset, regions for which ellipsoids may be representative of two or more coalesced voids account for ~38% of the entire dataset, and regions indicative of transgranular damage account for ~7% of the dataset.

These estimates are based on regions bound by the shape of the ellipsoids from the maximum peaks and there likely exists overlap between the intergranular and coalesced regions, i.e., a data point in the coalesced region may actually be a damage site along a triple junction or a short intergranular void through the thickness and a data point in the intergranular region may in fact be coalesced voids. However, this is the best indicator short of determining definite bounds of a/c and b/c for each mode of damage, which is impossible without comparing each void to the actual microstructure. The entire point of this exercise is to predict the approximate amount of damage present within the specimen for each damage mode in a nondestructive manner.

Figure 45 shows the FR microstructure's distribution of void shapes with three modal peaks at a/c and b/c values of 0.43 and 0.53, 0.65 and 0.74, and 0.83 and 0.92, respectively. The total number of transgranular voids present in the sample represented by the regions $1 \geq a/c \geq 0.65$ and $1 \geq b/c \geq 0$ and $0.65 \geq a/c \geq 0.50$ and $1 \geq b/c \geq 0.74$, is 442, accounting for ~35% of the dataset. The number of intergranular damage sites within the sample, bounded by $0.32 \geq a/c \geq 0$ and $1 \geq b/c \geq 0.3$ is 191, accounting for ~15% of the dataset. This leaves ~50% of the voids to fall within regions indicative of coalesced damage. Again, the shape regions used for damage mode fitting are based on the regions bound by the shape of the ellipsoids from the maximum peaks in the contour plots in Figures 43-45. Take the region bounded by $1 \geq a/c \geq 0.65$ and $1 \geq b/c \geq 0$, for example: the a/c range of $1 \geq a/c \geq 0.65$ describes data of dominate transgranular, thus the $1 \geq b/c \geq 0$ range simply sweeps all aspect ratio pairs within a region that must contain dominate transgranular damage due to the stipulation of $a > b > c$. These results are consistent with the XRT renderings, which showed a large amount of elongated ellipsoidal voids indicative of coalescence and spherical transgranular voids.

Figure 46 shows the HT microstructure's distribution of void shapes from samples 20354 and 20355 again with three modal peaks along a ridgeline. Before investigating the counts it is noticeable that the height of the modal peaks starts with the lowest of the three along the ridgeline, increasing to the highest as a/c and b/c go to 1. The opposite was the case for the FR specimen, thus right away there is an expectation that transgranular damage is the dominant mode within the HT specimens. For the same transgranular and intergranular regions defined for the FR sample there are 250 and 63 data points, accounting for ~47% and ~12% of the dataset, respectively. This leaves ~41% of the dataset for possible coalesced damage sites. Although a greater percentage of transgranular defined voids was expected it is nonetheless the largest bin for the specimens analyzed while the intergranular damage fraction is the least of any dataset, as expected from the XRT renderings.

The methodology and analysis for fitting individual voids to ellipsoids from their principal inertias proved able to predict the percentage of damage modes found within shocked copper polycrystals of varying microstructures. It has been determined that AR copper contained greater than or equal to 55% intergranular damage and from 2-D GB statistics it is the microstructure most sensitive to misorientation angle for the probability of finding damage at a GB. Since the GBs are the weakest feature in the material, due to strengthening of the grain bulks due to the pre-existing plastic, damage is forced to the GBs and the GB strength has an increased role for damage nucleation. It was found that the FR specimen was the most coalesced and least incipient with ~50% of all damage found indicative of coalescence and having the largest average void size compared to the average grain size of the material. The dominant damage mode within the FR structure is transgranular damage, since coalesced voids likely nucleated transgranularly before coming together. The HT specimens contained the least amount of intergranular damage and also contained the largest amount of transgranular damage at ~47%. As with the FR specimen, the HT specimens had a lessened dependence on GB misorientation angle for finding damage at a boundary. This is due to the large amount of coalesced and transgranular voids that may have coincidence with a GB on a 2-D section and are only present at the boundary because they have grown towards it or have coalesced with a void that nucleated there, but there is still an increased probability for damage in the 25° to 50° misorientation range. The next section aims to look beyond misorientation angle and GB energy to build upon the knowledge of what makes some GBs more favorable for containing intergranular damage than others.

6.3 3-D Reconstructions of Multicrystals and Damage

Copper multicrystal targets were chosen for this experiment to single out large volume intergranular damage sites, which are representative of microstructural weak links. Copper polycrystal targets are more useful when studying the statistics of damage sites [20, 22, 23], but the smaller average grain size makes it more difficult to determine where large volume damage sites nucleate as they can be on the same length scale as a single grain. Determining the weak links within a microstructure is of paramount importance for further improving the damage predicting capabilities of simulation work.

3-D reconstructions from serial sectioning revealed a uniform spall zone with the presence of several larger volume damage sites. Some of these sites were found along the outer region of the spall zone where one would expect to find the effects of the “intrinsic” momentum trap from the geometry of the experimental setup; hence, they were ignored [19]. The large volume damage sites chosen for analysis within the uniform damage region had linear dimensions along the serial sectioning direction such that at least ten slices contained them, for appropriate resolution, and are shown in Figure 47. It is important to verify that these large volume damage sites were present at GB interfaces, thus 3-D reconstructions of the microstructure were superimposed to the reconstructed spall zone to determine if the sites were indeed intergranular. The mechanical sectioning and polishing as well as the SEM and EBSD scans for these two MC specimens were done previously by Wayne [18]. The superposition of the spall zone and the microstructure is shown in Figure 48.

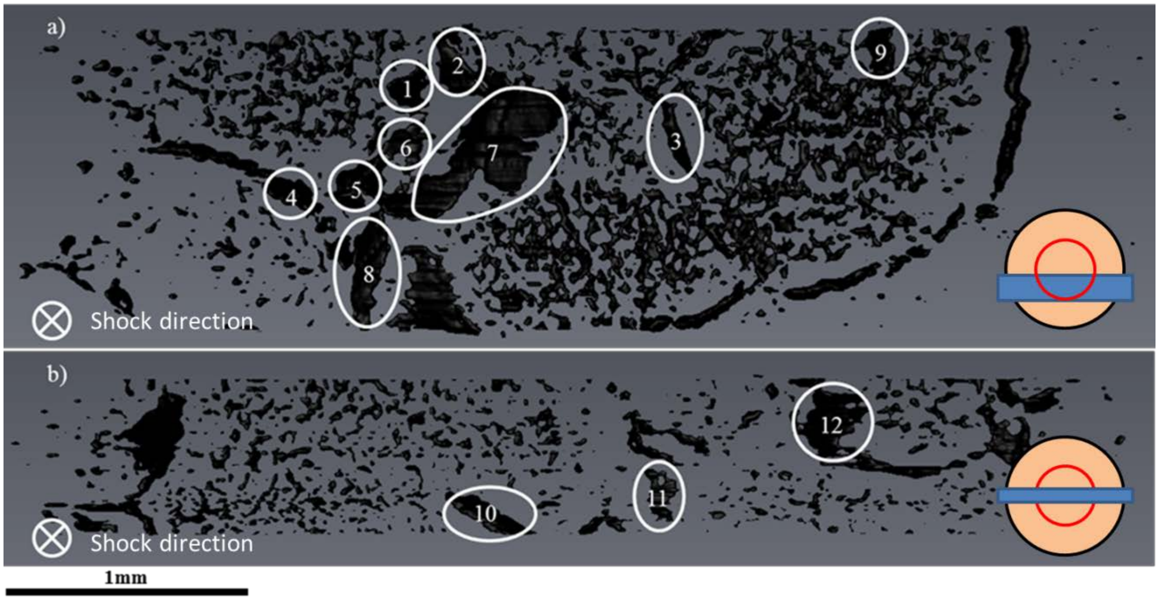

Figure 47: Large volume damage sites chosen for microstructural analysis from a) sample 19804 and b) 19803.

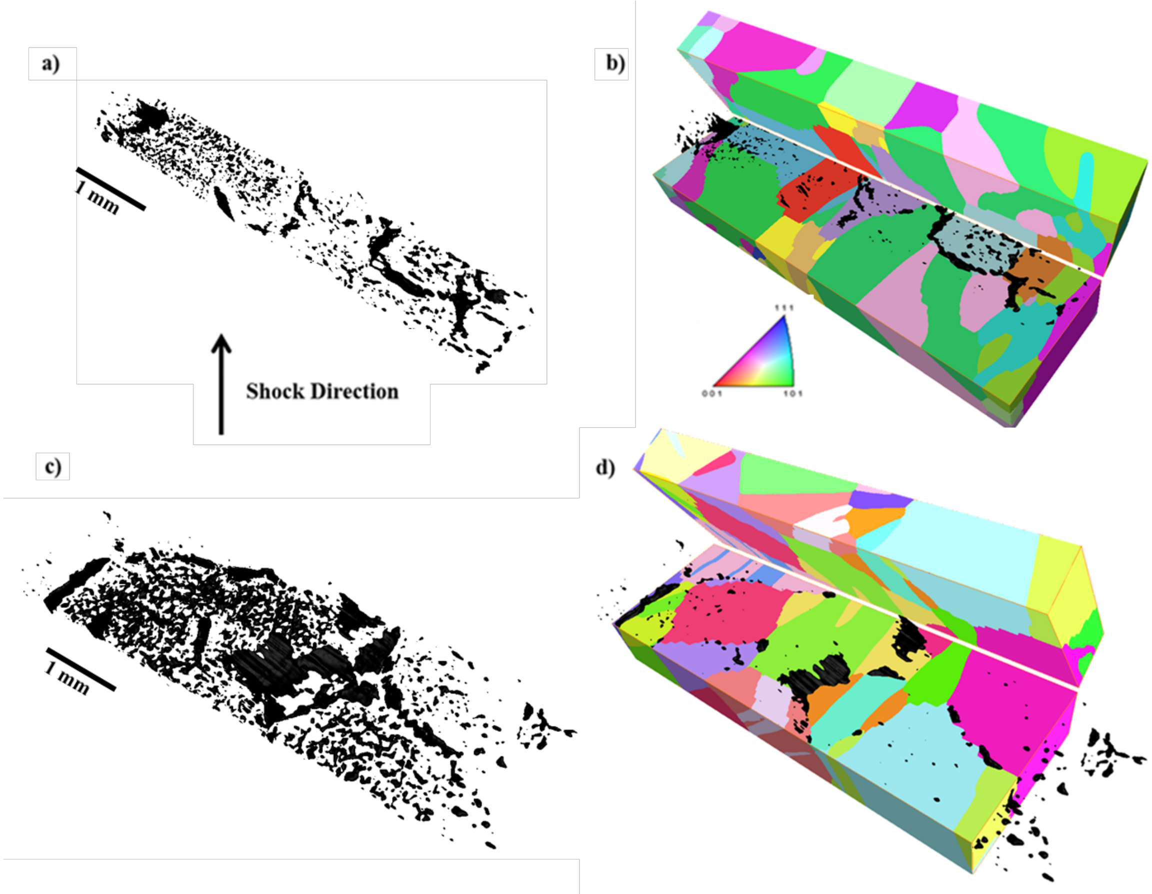

Figure 48: a) Spall zone in sample 19803, b) spall zone with superimposed microstructure of sample 19803, c) spall zone in sample 19804, d) spall zone with superimposed microstructure of sample 19804. Colors in (b) and (d) represent crystallographic directions parallel to the shock in each grain, as per the standard stereographic triangle in the inset.

Further visual inspection was done in these reconstructions to single out individual damage sites to study how the microstructure changes through the thickness in relation to the void's position. Figure 49 shows the evolution of the microstructure through the thickness surrounding damage site #1. The damage appears to be at a GB where a twin (labeled grain #1 and circled) terminates at a GB. As one goes through the thickness this twin stops at the boundary and another grain fills the space (labeled grain #2 and circled in black). It appears as though the damage nucleated at the tip of the twin (grain #1) and grew through thickness until it reached the interface of grain #2. Note that the normal to the plane of the slice in this cut-away is along the physical normal of the damage site along the GB. Each side of the cut-away is near its respective outer-edge of the void.

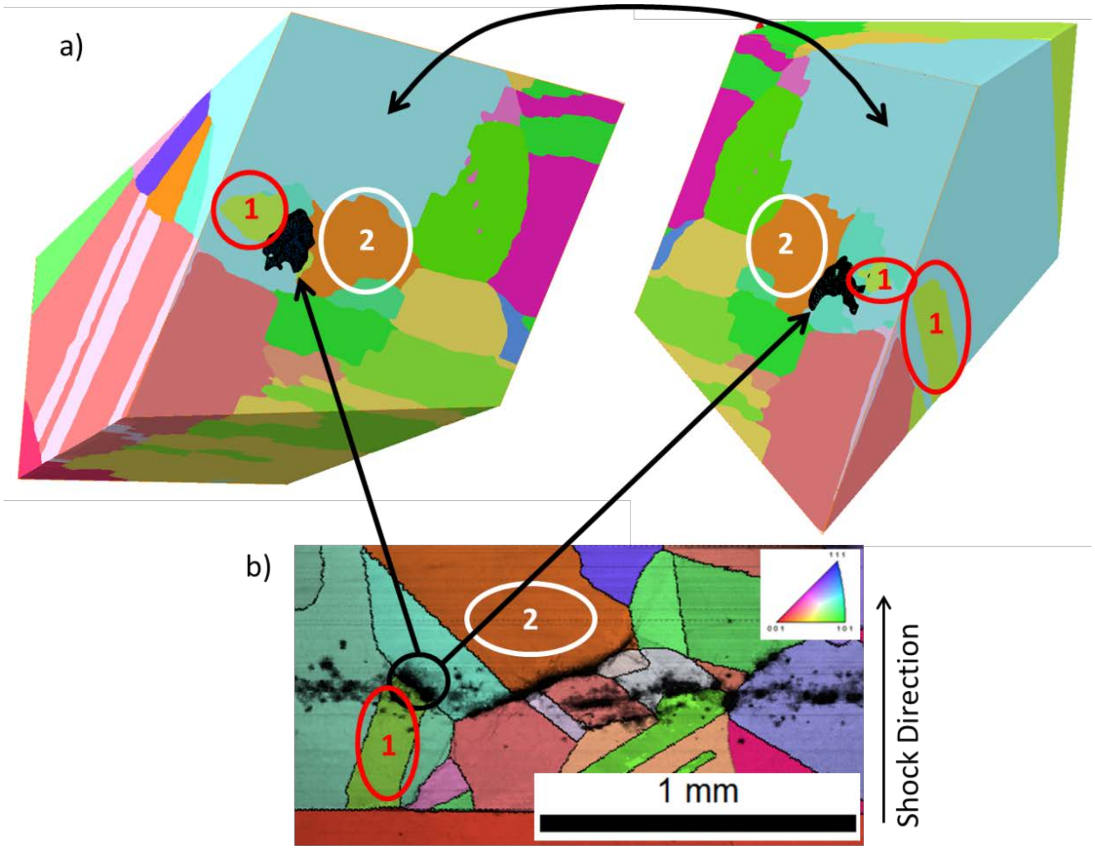

Figure 49: Through-thickness inspection of the microstructure surrounding damage site #1 (circled in black on the EBSD map). The damage site is present along a GB at the tip of the twin labeled grain #1 and grows until arriving at grain #2 through the thickness.

Each GB with a large-volume damage site was characterized by obtaining the crystallographic orientations of adjacent grains along the shock direction and parallel to the physical GB normal, as well as the axis of rotation and misorientation angle of the boundary. These are the 5 parameters necessary to fully characterize the GBs with the physical GB normal only obtainable from 3-D data, which is unique to the work presented here and the existing characterization in the literature. The inverse pole figures (IPFs) characterizing the large damage sites studied here are shown in Table 6 and 7 it is noticeable that the differences in orientation across the boundary differ from case to case. This evidence suggests that the mismatch in crystal orientation, and consequently mechanical behavior (due to anisotropy), can be high or low in either or both the shock direction and crystallographic GB normal and still obtain damage.

Table 6: IPF plots of orientations along the shock direction, along the crystallographic GB normal, and the axis/angle of misorientation of adjacent grains with large volume damage sites at the boundaries. Damage sites 3 and 6 nucleated along grains that share its boundary with two other grains along the width of the damage.

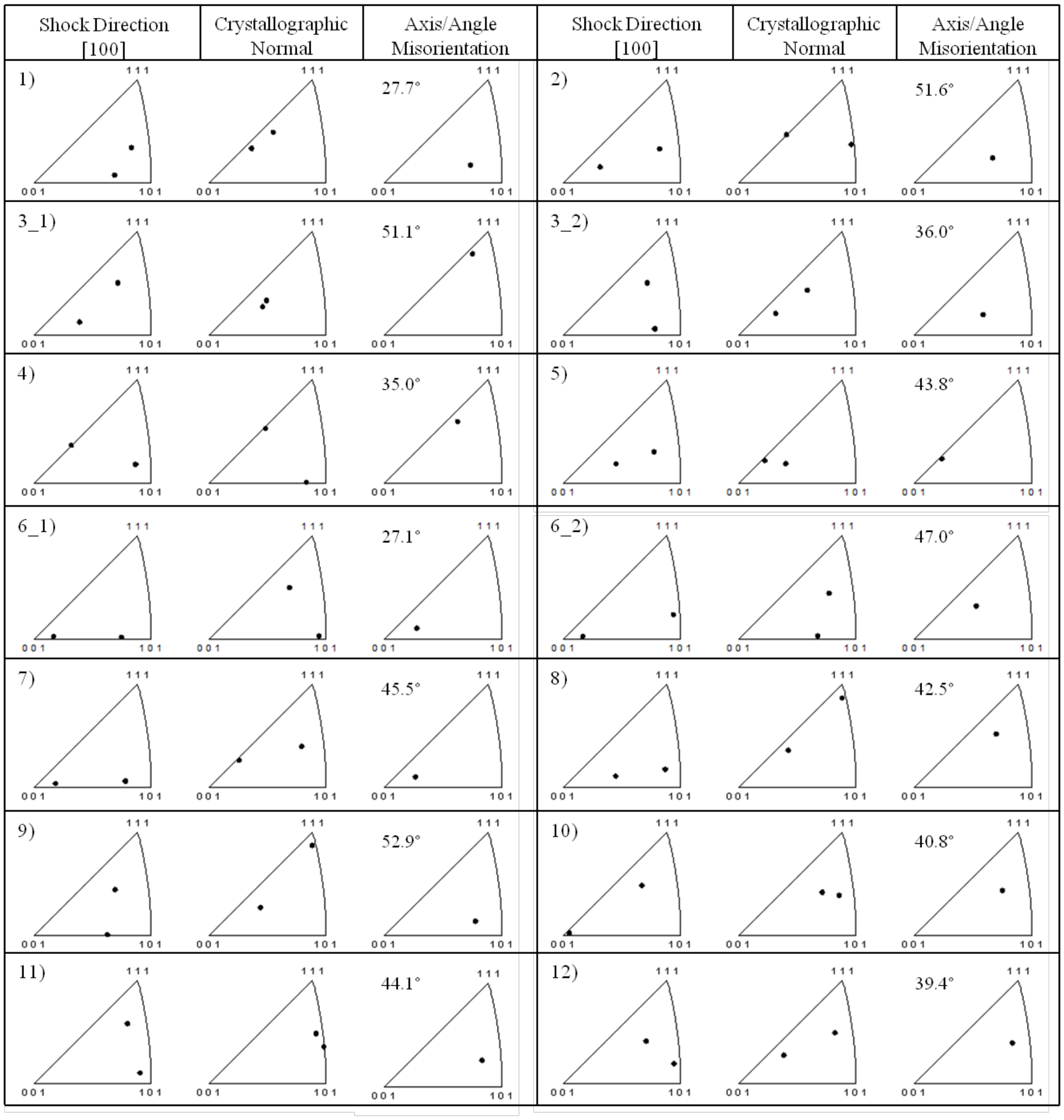

Shock Direction [100]	Crystallographic Normal	Axis/Angle Misorientation	Shock Direction [100]	Crystallographic Normal	Axis/Angle Misorientation
1)		27.7°	2)		51.6°
3_1)		51.1°	3_2)		36.0°
4)		35.0°	5)		43.8°
6_1)		27.1°	6_2)		47.0°
7)		45.5°	8)		42.5°
9)		52.9°	10)		40.8°
11)		44.1°	12)		39.4°

Table 7: Crystallographic data for each intergranular damage site listed in order from the largest to smallest volume damage site, site 7 with the largest volume of 4.94 x 10^6 μm^3.

Damage Site #	Normalized Volume	Misorientation Angle (deg)	Shock / GB Normal Angle (deg)	Taylor Factors GB Normal	Taylor Factors Shock Direction
7	1.00	45.5	29.5	3.25 / 3.30	2.40 / 3.48
8	0.512	42.5	39.4	2.49 / 3.47	2.58 / 3.55
3_1	0.404	36.0	84.8	3.19 / 3.26	3.48 / 3.10
3_2	0.404	51.1	81.3	2.68 / 3.15	2.54 / 3.10
10	0.294	40.8	42.3	3.16 / 3.56	2.43 / 3.00
12	0.267	39.4	43.6	2.62 / 3.10	3.60 / 3.10
9	0.247	52.9	73.4	2.62 / 3.55	3.10 / 3.08
5	0.213	43.8	36.2	3.35 / 3.48	2.60 / 3.35
4	0.196	42.4	71.3	2.79 / 3.55	2.77 / 3.37
2	0.182	51.6	37.7	2.96 / 3.27	2.48 / 3.40
1	0.145	27.7	49.1	2.81 / 2.55	3.30 / 3.40
6_1	0.118	27.1	29.4	3.06 / 3.21	2.40 / 3.40
6_2	0.118	47.0	6.30	2.41 / 3.61	2.40 / 3.55
11	0.072	44.1	8.40	3.62 / 3.30	3.62 / 3.30

The Taylor factors for each of these directions (both shock and GB normal) were obtained using results from [95] by superimposing the IPF Taylor factor contour plots and the data points from the mismatches across the GBs from the IPF plots shown in Table 6. A high mismatch in the Taylor factor should indicate stress localization, but a high mismatch on this variable along the shock direction alone does not seem to be enough to insure that there is an increased likelihood of damage at the boundary, according to [15]; hence, the mismatch in Taylor factor along the GB normal has been added as an additional variable for analysis. Table 7 shows data extracted from a comprehensive microstructural study around each large volume damage site.

An analysis of the data presented in Table 7 suggests that multiple mechanisms are likely driving the localization of damage at the GBs. The two largest volume sites have large Taylor factor mismatch pairs along the shock direction and occur at GB misorientations among the highest probability bins found from the 2-D damage statistics, in the 40° to 45° range. Though these results are from statistical analysis of a copper polycrystals, the correlation between misorientation and the probability for finding damage localization at a GB obtained from those samples seems to hold in the multicrystalline samples studied here. Note that all the damage sites in Table 7 fall within the statistically weak 25° to 50° range from the 2-D polycrystal studies, implying that the distribution of probability of spall damage at a GB within this misorientation angle range is characteristic of the material.

The data suggests that the largest mismatches in the Taylor factor along the shock direction can lead to the growth of large volume voids, likely due to strain localization next to the boundary induced by plastic mismatch. Damage site 6 has one of the lowest volumes in the entire dataset and occurs at a triple junction; one of the GB interfaces has a high mismatch in Taylor factor with respect to the crystallographic GB normal, while both have a high mismatch in Taylor factors along the shock direction. The boundary 6_1 has a misorientation that is statistically less favorable for containing damage as compared to the boundary 6_2. Based on the higher Taylor factor mismatches and more favorable misorientation angle for damage nucleation at GB interface 6_2 it is likely that the void nucleated at this interface and the boundary at 6_1 prohibited further growth of the void. It is reported by Escobedo et al. [15] that sites with the largest differences in Taylor factors between adjacent grains seemed to be resistant to void nucleation at the boundaries; however, their results suggest that voids were nucleating at boundaries with similar differences nearby. This may be due to the geometric orientation of the grain boundary and/or the contribution of the grain boundary strength, which play roles alongside the plasticity effects to determine where damage nucleates in the microstructure.

The results collected here also suggest that damage sites with low mismatches in the Taylor factor along the crystallographic GB normal are present due to a weak GB, either from incoherent twins or from falling within the statistically weak misorientation angle range. In that regard, damage site 3_2 is actually close to a ∑3: the rotation axis is close to <111>, and the misorientation angle is just within the measurement error of the deviation allowed by the Brandon criterion [87], which is about 60±8.7° for a ∑3. The GB normal for that site, which is close to being the same for both grains, is not {111}, and it is closer to {211}, which indicates that site 3_2 is close to an incoherent twin. Notice that damage site 3 is ranked 3rd in terms of damage volume. Another interesting site is number 11: the rotation axis is close to <110> and the misorientation angle is 44.1°, which also within measurement error of the misorientation angle range allowed for a ∑9, in this case 38.94±5°. The GB plane, is also the same for both grains and close to the {221} twinning plane for ∑9, suggesting that the boundary might have special properties. Damage site 11 ranked last in terms of damage volume for all sites studied, but the Taylor factor mismatches were low, and this actually suggests that this boundary was intrinsically weak, as it presented significant damage despite having a lower mismatch in plastic behavior along the shock and the GB normal. Note that the misorientation angle is again close to 45°, suggesting a weak GB in this case.

Another interesting observation is that, if one takes a value of 3.06 for the Taylor factor, the result for a random FCC polycrystal [95], all the sites selected have at least one of the Taylor factor mismatches as high as 10% of that value, except for site #1, which comes close nonetheless. This suggests that mismatch in plastic behavior across the boundary induced by material anisotropy is indeed important on damage localization, provided it is quantified in 3-D.

Related work published in the open literature has reported that for all Σ1 and Σ3 boundary types in copper polycrystals there is no void nucleation [15]. This seems to be accurate for the low angle misorientations represented by the Σ1 boundaries, but it is seen here, and by [20, 22, 23], that Σ3 boundaries that do not have {111} GB planes, e.g., incoherent twins, can be susceptible to damage, although it was observed here that not every incoherent or terminated twin close to the spall plane resulted in damage localization, which is consistent with the results presented in [21], where a GB with a 50° misorientation was shown to localize much more spall damage than a what seems to be an asymmetric ∑3 GB, based on the crystallographic information provided. It can be difficult to confirm where void nucleation takes place within the microstructure when the average void diameter approaches the average grain size as was the case for several of the microstructures studied in [15].

It is also important to consider how the voids evolve through the thickness via serial sectioning or X-ray tomography techniques because a 2-D cross-section is not enough to tell if the center, or place of largest girth, is being analyzed. If it is not near the center, then the void may be larger through the thickness, and, since the microstructure also changes through the thickness, one cannot pinpoint where that specific void most likely nucleated, particularly if triple junctions are involved. The aforementioned factors make it especially difficult to tell if a void has nucleated at the tip of an incoherent twin boundary in microstructures similar to those presented in [15]. By sampling smaller voids as in [15] one inadvertently might create a bias towards stronger boundaries. The opposite is also true in the work in [20, 22, 23], and the results presented here. In the former case, the use of copper samples in the half-hard condition might have biased damage to the GBs, by making the bulk stronger, allowing for better differentiation of the GB tendencies for damage localization as a function of misorientation, and in the work presented here the selection of the largest damage sites implies a definite bias towards the weak locations, which, given the large volume of the grains, are likely to be the GBs. Furthermore, the number of voids sampled in [15] is lower than the number used in [20. 22, 23] and this work, and there is no indication of whether or not the bias of the initial misorientation distribution was taken into account as was done here and in [20, 22, 23]. All these issues are likely to contribute to the differences in conclusions found in the literature.

Another important geometrical aspect of this problem is the relationship between the GB physical normal and the shock direction described in 3-D. As this value approaches 90° the GB aligns with the shock direction. When analyzing the volume of each void with the corresponding angle between the shock direction and the GB physical normal, one finds that there are more larger volume sites present in the 0°-45° range, shown in Figure 50.

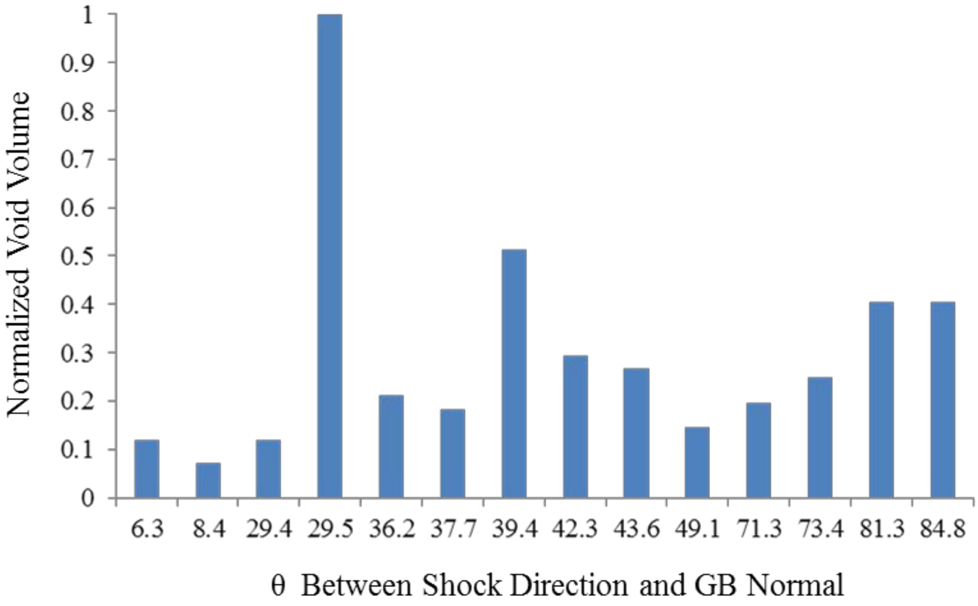

Figure 50: The normalized volume of each damage site along with the respective angle between the shock direction and the GB physical normal.

The two voids occurring at triple junctions, voids 3 and 6, have angles of 84.8° and 81.3° and 6.3° and 29.4°, respectively. Note that these two sites account for two data points that are the smallest in the lower bin of 0°-45° and the largest in the higher bin of 45°-90°. Considering these special triple junctions as one data point each, there are 4 damage sites in the 0°-45° range with a larger volume than the largest damage site in the 45°-90° range. When analyzing the distribution of data points, there are 8 damage sites present in the 30°-50° range, if the 29.4° and 29.5° angles are counted, making up 67% of all unique damage sites analyzed. If void volume is included into this binning analysis it appears that there is a preference around the 40°-50° range, which suggests that the shear component of the overall stress state, the deviatoric component of which is ideally identical to that produced by a uniaxial stress parallel to the shock direction at the moment right before nucleation, may play a role in nucleating damage at the GBs.

Fensin et al. [100] conducted a statistical analysis of the angles of GBs containing damage between the shock direction and 2-D inclination of GBs. It was determined that GBs with inclinations perpendicular to the shock direction (67.5°-90°) were an order of magnitude more likely to nucleate a void compared to boundaries parallel to the shock direction [100]. The average grain size of the PC target specimen analyzed was ~60 µm in diameter with voids present in the material approaching this size making it impossible to determine if the void nucleated at the boundary or rather exists there due to growth, whereas there is no doubt the large volume damage sites presented in this work exist at GBs. MD simulations were also conducted showing the shear stresses from GBs perpendicular to the shock direction showing an absence in shear stress, reducing plastic deformation and, thus, leading to lower stresses for void nucleation [100].

When comparing the results from Fensin et al [100] to those presented in this work, there are differences to consider. Firstly, the results from Fensin concentrate on the effects the inclination angle between GBs and the shock direction have on void nucleation in copper PCs, whereas the results presented here concentrate on studying the relationship between said inclination angle and the presence of large volume damage sites at clear GBs in copper MCs. Although GBs perpendicular to the shock direction are statistically likely to nucleate damage according [100], it is entirely plausible that voids nucleating at GBs inclined 30°-50° from the shock direction are more likely to experience growth due to higher shear stresses producing plastic deformation, which is the primary mechanism that drives void growth. Additional data for large volume damage sites at GBs are needed in order to confirm this hypothesis.

It is interesting that the largest volume site occurred for a GB with a normal at ≈ 30° from the shock direction. This suggests that a significant fraction of the stress at the moment of nucleation, about 70%, was acting to open the GB. It is noteworthy, however, that damage site 7 was present at a boundary between two of the largest grains in sample 19804. Upon damage nucleation there may not have been any coincident grains or triple junctions to prevent it from growing along the entire GB of the large grains. To confirm that GB normals inclined less than 45°, or in the 40°-50° range, are preferential to larger volume void nucleation and growth one needs more statistical sampling. The same holds true for some of the other trends discussed in this section. However, the use of simulations can provide further insight into the mechanisms at play, and initial simulations by Krishnan [19, 24] have done as much.

By comparing the crystallographic and volumetric data obtained in this work and the simulation work in [19, 24] it was found that the nucleation of large volume damage sites within the uniform damage zone is due to several contributing factors, including: the mismatches in the Taylor factor with respect to the shock direction and the crystallographic GB normal, the misorientation across adjacent grains, and the presence of an incoherent twin boundary or a terminated twin at a GB. Large Taylor factor mismatches are favorable for void nucleation and growth, but this can be kept in check by a GB with high interfacial strength, assuming the void nucleates at the boundary and not beside of the boundary due to strain localization which has been seen in various computational works [19, 24, 19, 71]. It is also observed that GBs that are likely to have intrinsically low strengths are favorable for void nucleation and growth, resulting in very large volume damage sites when coupled with large Taylor factor mismatches.

When combining all three, non-independent variables, it appears that a high Taylor factor mismatch along the shock direction is favorable for nucleating damage at a GB, whereas the Taylor Factor along the GB normal typically also requires to be coupled with a GB of low strength for void nucleation. From simulations by K. Krishnan [19, 24] it was found that a large mismatch in the Taylor factor along the GB normal resulted in high stress and strain states that resulted in damage growth along a boundary, whereas a low Taylor factor along the shock direction of an adjacent grain with damage at the boundary seemed to be responsible for void growth perpendicular to the boundary. These conclusions on void growth direction are supported by the experimental data, as the voids tend to be thicker towards grains of a lower Taylor factor.

A preliminary analysis of the geometrical effects of GB orientation in 3-D with respect to the shock direction was also conducted, and suggests that when the angle between the shock direction and the GB physical normal ranges from 0° to 45°, more specifically the 30°-45°, range the presence of shear stresses combined with opening tractions perpendicular to the GB tend to encourage plastically driven higher volume void growth. When coupled with the results from Fensin et al. [100] it becomes clear that void nucleation may statistically prefer GBs perpendicular with the shock direction, but large volume void growth is more likely to occur at boundaries close to 45° due to plastic deformation from high shear stress states.

6.4 3-D Analysis of Partial Voids and Surrounding Microstructure

Focused ion beam sectioning of individual voids at the edge of a polished cross-section from shocked MC copper specimens was performed with the goal of characterizing the plastic deformation surrounding inter- and transgranular damage sites. All damage sites characterized in this work come from cross sections into the spall plane of sample 19808. The first volumetric data set from FIB sectioning processes was taken at ASU and has an in plane resolution of 0.75µm and a 2µm distance between slices through the thickness. Figure 51 shows the IPF maps of several sections from the complete dataset of 8 sections total.

Figure 51 shows three damage sites of interest in this section. It is important to first obtain the orientation of each grain away from the effects of the plastic zones surrounding the damage sites. The upper and lower grains on the IPF maps are of orientations parallel to the shock of <1 1 2> and <1 2 20>, respectively, and the latter is ~6° from <0 0 1>. These two grains have a high mismatch in Taylor factors across the boundary along the shock direction since <1 1 2> has a high Taylor factor and <0 0 1> has a low Taylor factor. According to the results from the MC study, this mismatch in the Taylor factor should promote damage nucleation and growth.

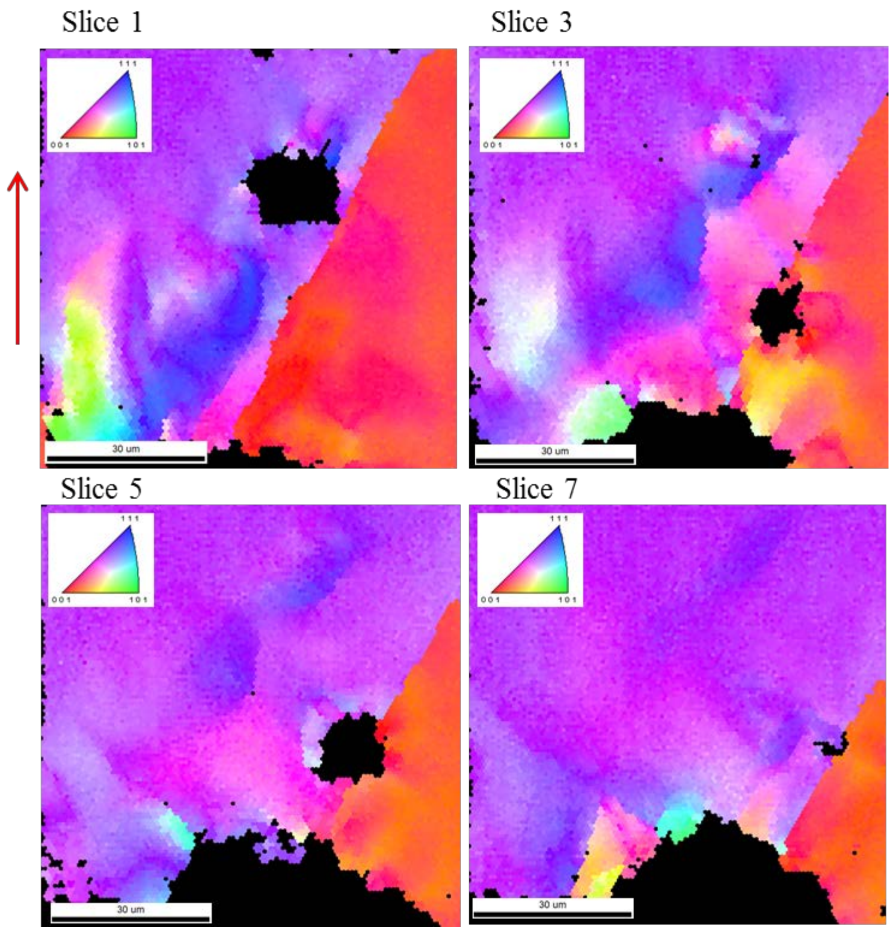

Figure 51: IPF maps of a serial sectioned void with the red arrow indicating the shock direction. The large damage site at the bottom of the datasets remains through all 8 slices taken. Two smaller voids appear and disappear through the thickness as seen clockwise from the top left.

Two graphical functions available in the EBSD analysis software to examine the plasticity present within the material are the average misorientation (LAM) and grain reference orientation deviation-angle (GROD) maps. The LAM map takes the center point of a user-defined kernel, in this case 3 points, and colors in the map are assigned according to the average misorientation that all points in the kernel make with their neighbors [79]. This is useful to visualize changes in orientations on a local level. The GROD map takes each point and colors it according to its angular deviation to a reference orientation for the grain in which it belongs, which may become inaccurate for heavy plastically deformed data sets like the ones presented here. Hence, LAM maps were analyzed first and the corresponding results for each slice analyzed are shown in Figure 52.

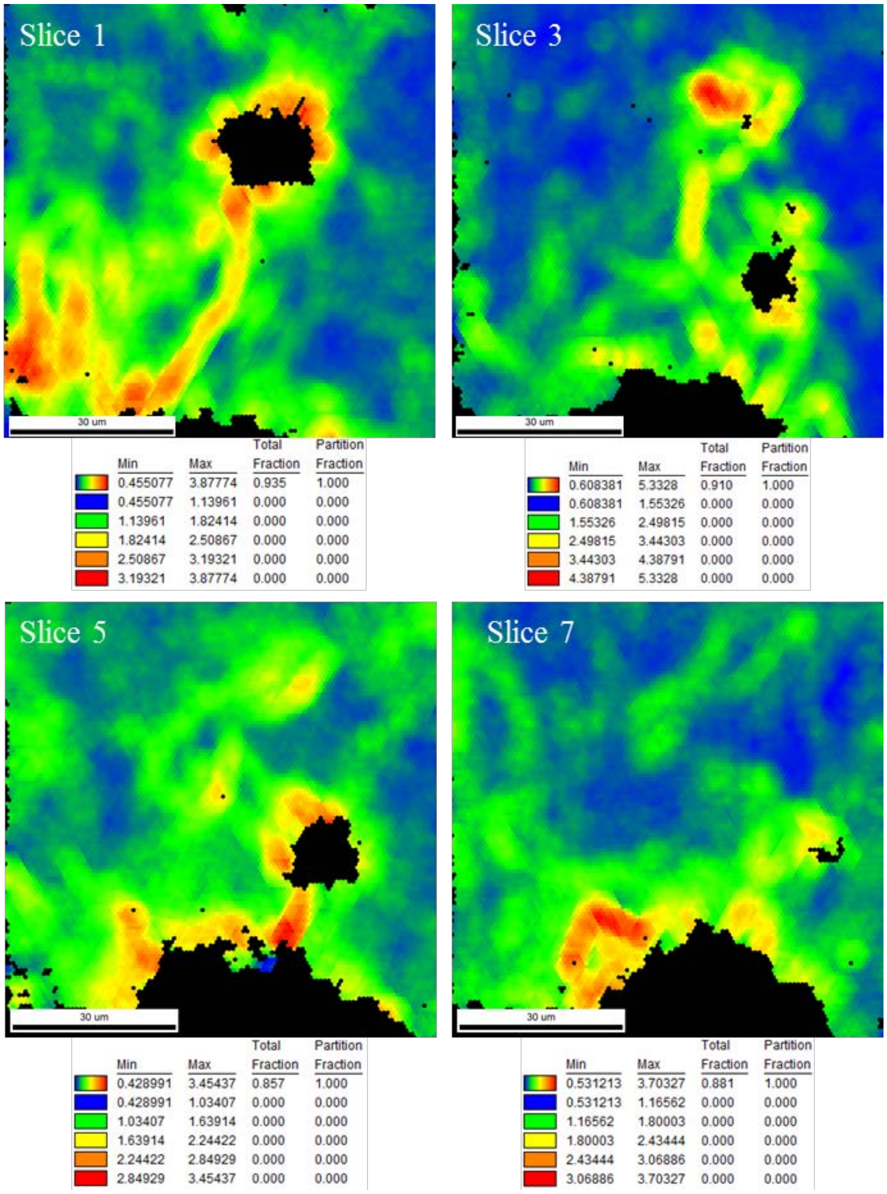

Figure 52: LAM maps the four slices shown in Figure 50. Note the interconnectivity between the voids indicated by ligaments with high misorientations.

From Figure 52 it is clear that there are interactions between the voids in the form of regions with high misorientations, which is indicative of localized plastic deformation. The distance between the surface of the large void at the bottom of slice 1 and the smaller void is 41 µm. The diameter of the smaller void is ~18 µm and the plastic zone surrounding the void has minimum and maximum distances of 28 µm and 32 µm, respectively. This corresponds to an average plastic zone extending 5 to 7 µm from the surface of the void in the plane, or, ~33% the size of the void diameter. This is the contribution to the deformation in the material caused by the presence of this individual void as there is full connectivity between the plastic zones with the large void at a distance of 41 µm. The void disappears on slice 3 and the through thickness plastic zone of the void extends until slice 7, a distance of 8 µm, similar to the in plane size of the plastic zone, indicative of uniformity in the void's affected regions.

A second small void appears on slice 3 of the sectioning process at the GB and begins to disappear on the last data set, slice 7. From slice 3 it is measured that the distance between the edge of the remaining plastic zone from the previous void and the second void's surface is ~20 µm. The void is ~14µm in diameter at its largest size in the data in slice 5, from which the void is ~9 µm from the surface of the large volume damage site at the bottom of the dataset. The minimum and maximum distances of the plastic zone around the second void on slice 5 are 21 µm and 28 µm, respectively. This corresponds to an average plastic zone extending 3.5 to 7 µm from the surface of the void, or, from 25% to 50% the size of the void diameter. What is intriguing is that in slice 1 there is no indication of another void hidden below the surface of the material via misorientation spread, yet the void appears in slice 3. Slice 2 shows faint traces of misorientation spread, however, this puts the through thickness plastic zone at a maximum of 2-3 µm, less than the in-plane size.

The large volume intergranular damage site shown near the bottom of Figures 51 and 52 has an affected plastic zone that fluctuates in size through the thickness of the material. The ligaments seen from the LAM maps in Figure 52 show indicate a larger spread in lattice rotations within the <1 1 2> grain, which is the grain with a higher Taylor factor association with the shock direction. This supports the theory presented here and in Krishnan [19] that the adjacent grain at a GB containing damage with the higher Taylor factor promotes plastically driven growth. Further investigation into the 3-D lattice rotation around intergranular sites is needed for additional existing data sets.

The next two serial sectioning experiments were conducted at LANL at higher resolutions than the previous data. The second sectioning data set is of a transgranular void within a grain orientation parallel to the shock direction of <6 7 13>, which is ~2.5° from <1 1 2> as seen in the IPF maps shown in Figure 53. The <1 1 2> direction has a high Taylor factor associated with it, which would be less likely for transgranular void growth according to the results found in this work and simulations by K. Krishnan [19]. As seen in Figure 51, the void in question did not grow to a large volume, as its average diameter is 10.5µm.

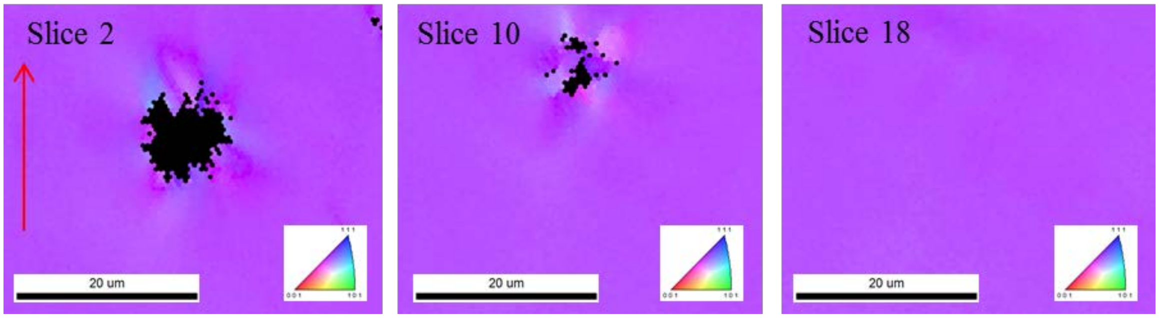

Figure 53: IPF maps of a serial sectioned void with the red arrow indicating the shock direction. The void disappears as the slice number increases, from left to right, until the void's misorientation field dissipates in slice 18. Data was acquired for 25 slices total.

Each slice for this FIB section was conducted at a depth of 0.5 µm, the same as the in-plane resolution of the EBSD scan. From the SEM images slice 13 appears to be the last section for which the void is visible. Slice 18 was the first section with no discernable misorientation influence from the presence of the void and was taken as the last section for profiling the plastic deformation field's influence through the thickness of the material, which was ~2.5 µm from the end of the void through the thickness of the material, which is ~1/4 of the void's diameter. The red lines present on the LAM and GROD maps in Figure 54 show where measurements were taken at the minimum and maximum distances of the plastic zone surrounding the void. For slice 2 the plastic zone's minimum and maximum distance for the LAM and GROD maps, respectively, are: 13.3 µm and 17.2 µm, and, 13.5 µm and 22 µm. Taking into account the void's diameter and approximating the region of influence to be uniform on either side of the void for each measurement, one obtains a plastic zone ranging from 1.65 to 6 µm from the surface of the void. Repeating these distance measurements for the LAM and GROD in slice 10, one obtains: 10.5 and 15.2 µm, and, 18 and 18.5 µm. Taking into account the average diameter of the void in this slice is 7 µm these correspond to a plastic zone size ranging from 1.75 to 5.75 µm from the surface of the void. These values being similar to those found in slice 2 indicate uniformity in the plastic zone surrounding the void.

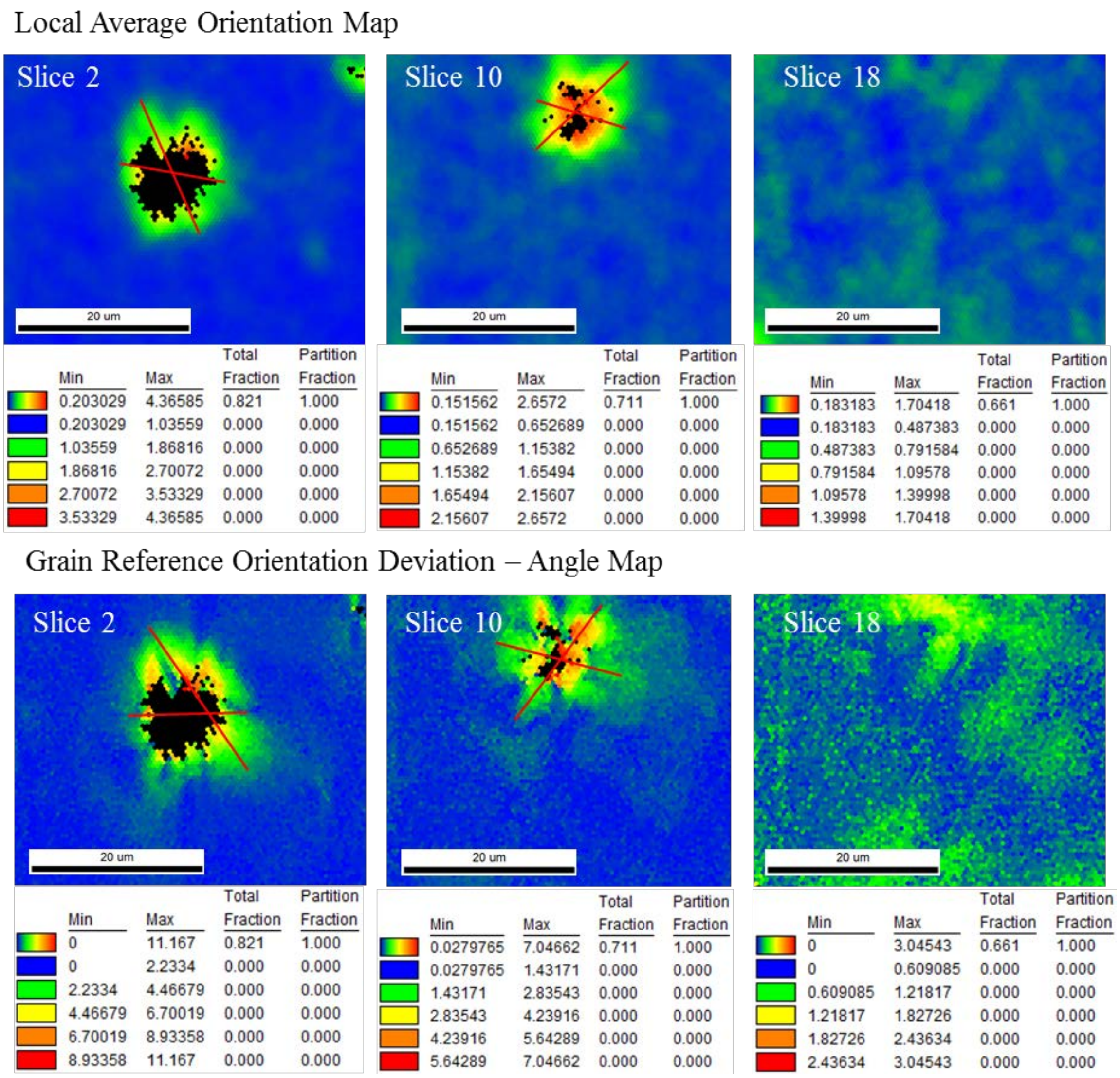

Local Average Orientation Map – Slice 2

	Min	Max	Total Fraction	Partition Fraction
🌈	0.203029	4.36585	0.821	1.000
🟦	0.203029	1.03559	0.000	0.000
🟩	1.03559	1.86816	0.000	0.000
🟨	1.86816	2.70072	0.000	0.000
🟧	2.70072	3.53329	0.000	0.000
🟥	3.53329	4.36585	0.000	0.000

Local Average Orientation Map – Slice 10

	Min	Max	Total Fraction	Partition Fraction
🌈	0.151562	2.6572	0.711	1.000
🟦	0.151562	0.652689	0.000	0.000
🟩	0.652689	1.15382	0.000	0.000
🟨	1.15382	1.65494	0.000	0.000
🟧	1.65494	2.15607	0.000	0.000
🟥	2.15607	2.6572	0.000	0.000

Local Average Orientation Map – Slice 18

	Min	Max	Total Fraction	Partition Fraction
🌈	0.183183	1.70418	0.661	1.000
🟦	0.183183	0.487383	0.000	0.000
🟩	0.487383	0.791584	0.000	0.000
🟨	0.791584	1.09578	0.000	0.000
🟧	1.09578	1.39998	0.000	0.000
🟥	1.39998	1.70418	0.000	0.000

Grain Reference Orientation Deviation – Angle Map – Slice 2

	Min	Max	Total Fraction	Partition Fraction
🌈	0	11.167	0.821	1.000
🟦	0	2.2334	0.000	0.000
🟩	2.2334	4.46679	0.000	0.000
🟨	4.46679	6.70019	0.000	0.000
🟧	6.70019	8.93358	0.000	0.000
🟥	8.93358	11.167	0.000	0.000

Grain Reference Orientation Deviation – Angle Map – Slice 10

	Min	Max	Total Fraction	Partition Fraction
🌈	0.0279765	7.04662	0.711	1.000
🟦	0.0279765	1.43171	0.000	0.000
🟩	1.43171	2.83543	0.000	0.000
🟨	2.83543	4.23916	0.000	0.000
🟧	4.23916	5.64289	0.000	0.000
🟥	5.64289	7.04662	0.000	0.000

Grain Reference Orientation Deviation – Angle Map – Slice 18

	Min	Max	Total Fraction	Partition Fraction
🌈	0	3.04543	0.661	1.000
🟦	0	0.609085	0.000	0.000
🟩	0.609085	1.21817	0.000	0.000
🟨	1.21817	1.82726	0.000	0.000
🟧	1.82726	2.43634	0.000	0.000
🟥	2.43634	3.04543	0.000	0.000

Figure 54: LAM maps and GROD maps for three slices of the sectioning process. The red lines indicate measurements taken of the misorientation fields surrounding the voids, indicative of a plastic zone.

It was found that the minimum values for the influence of the plastic zone around the void were approximately along crystal directions following <1 3 3> and <1 6 11> and the maximum values along <1 2 5>, <1 1 5>, and <1 3 7>. Regarding the Taylor factors of these directions, <1 3 3> has a high Taylor factor, <1 6 11> has a moderate Taylor factor, <1 2 5> has a high Taylor Factor, <1 1 5> has a low Taylor factor, and <1 3 7> has a high Taylor Factor. There appears to be little to no correlation between Taylor factor along these directions and the size of the plastic zone surrounding the void as there are high Taylor factor orientations present in both the minimum and maximum dimensions of the plastic zone. These directions of the plastic strain lobes are 2-D projections, thus further data analysis of full 3-D data sets may provide more insight of the Taylor factors along 3-D directions of the plastic strain lobes. The average size of the plastic zone from the surface of the void is 3.75 and 3.825 µm in slices 2 and 10, respectively, roughly 1.5 times the size of the 2.5 µm distance through extending through the thickness. It is shown that the influence of the plastic zone surrounding the void is non-uniform, and on average extends from 25% to 38% the overall diameter of the void into the material in all directions.

The final data set analyzed from FIB reconstructions around spall damage revolves around a large volume damage site at a GB with a smaller transgranular damage site emerging through the thickness of the sectioning process. The step size for the EBSD mapping was 0.5 µm in the plane with a section depth of 0.5714 µm through the thickness. The upper and lower grains shown in Figure 55 are oriented parallel with the shock direction at <1 4 5> and <2 7 8>, which is ~4° from <1 4 4>, respectively. Although the grains are of similar orientation parallel to the shock direction, the GB itself is misoriented at ~50°.

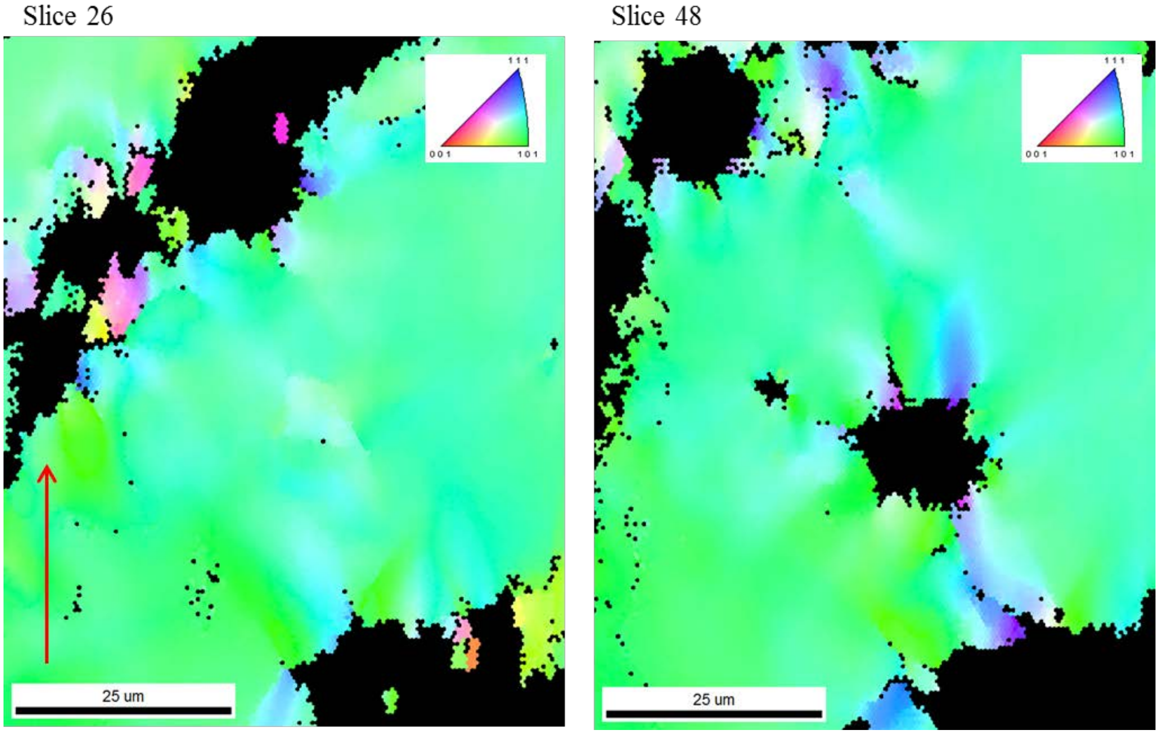
Slice 26

Slice 48

Figure 55: IPF maps of serial sectioned damage sites along a GB (left) which later reveals the presence of a transgranular damage site (right). The red arrow indicates the shock direction.

The presence of the hidden void began to show on slice 26 with faint misorientation changes appearing, as seen in the LAM map in Figure 56. By slice 32 there were linear patterns of misorientation fields surrounded by lesser intensity ones, indicative of dislocation loops and subgrains. In slice 26 the incipient stages of the main cell walls were within 4° from the following crystal directions following: <0 1 1>, <1 2 2>, and <1 1 3>, all of which have high Taylor factors. By slice 39 a quadrilateral shape had taken form with all four sides representative of <1 2 2>. This orientation has a high Taylor factor which are typically more resistant to deformation than directions with lower Taylor factors, such as <0 0 1>, for example.

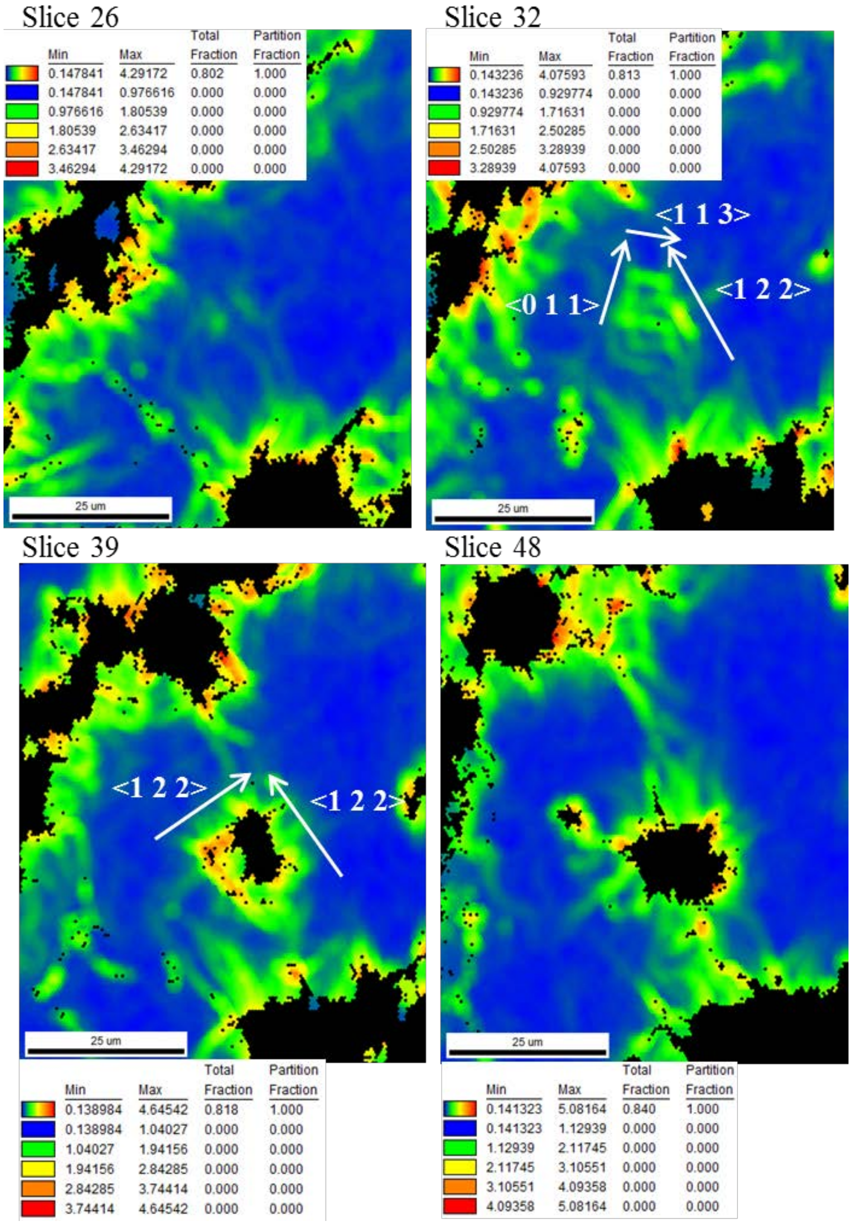

Slice 26

	Min	Max	Total Fraction	Partition Fraction
▨	0.147841	4.29172	0.802	1.000
🟦	0.147841	0.976616	0.000	0.000
🟩	0.976616	1.80539	0.000	0.000
🟨	1.80539	2.63417	0.000	0.000
🟧	2.63417	3.46294	0.000	0.000
🟥	3.46294	4.29172	0.000	0.000

Slice 32

	Min	Max	Total Fraction	Partition Fraction
▨	0.143236	4.07593	0.813	1.000
🟦	0.143236	0.929774	0.000	0.000
🟩	0.929774	1.71631	0.000	0.000
🟨	1.71631	2.50285	0.000	0.000
🟧	2.50285	3.28939	0.000	0.000
🟥	3.28939	4.07593	0.000	0.000

Slice 39

	Min	Max	Total Fraction	Partition Fraction
▨	0.138984	4.64542	0.818	1.000
🟦	0.138984	1.04027	0.000	0.000
🟩	1.04027	1.94156	0.000	0.000
🟨	1.94156	2.84285	0.000	0.000
🟧	2.84285	3.74414	0.000	0.000
🟥	3.74414	4.64542	0.000	0.000

Slice 48

	Min	Max	Total Fraction	Partition Fraction
▨	0.141323	5.08164	0.840	1.000
🟦	0.141323	1.12939	0.000	0.000
🟩	1.12939	2.11745	0.000	0.000
🟨	2.11745	3.10551	0.000	0.000
🟧	3.10551	4.09358	0.000	0.000
🟥	4.09358	5.08164	0.000	0.000

Figure 56: LAM maps for various slices of interest from FIB sectioning data, beginning with faint traces of misorientations from the buried void in slice 26 to full exposure at maximum diameter of the void in slice 48.

The size of the plastic zone around the transgranular void through the thickness extends from slice 26 to slice 39, where the void first comes to the surface. The sectioning step size of 0.5714 µm over these 12 slices gave a through thickness plastic zone of 6.86 µm, ~50% of the 14 µm diameter of the void at its largest in slice 48. The plastic zone was approximated by a rectangle from slice 39 with edges of 19.5 µm and 21 µm with the size of the void measured to be 6 µm by 12.5 µm, meaning that the plastic zone extends from the surface of the void 6.75 µm along the 6 µm void dimension and 4.25 µm along the 12.5 µm void dimension. The void reached its maximum size on slice 48 with an approximate circular diameter of 14 µm. The minimum and maximum sizes of the plastic zone were 25.2 and 34.3 µm, excluding the coalesced misorientation with the large damage site at the bottom of the scan. The plastic zone for this slice extended from the void surface between 5.6 and 10.15 µm. The average plastic zone around the surface of the void in the plane of the scan was 6.69 µm, almost the same as the reported 6.86µm through the thickness of the material, indicating an approximately uniform plastic zone ~48% the size of the diameter extending in three dimensions.

Results from all three data sets indicate that incipient damage sites of diameters between 10 to 20 µm have approximately uniform plastic zones in three dimensions extending outwards from the void surface for distances of 25% to 50% the diameter of the void itself. It was also found that the smaller, incipient damage was present within grains of high Taylor factors along the shock direction for all cases. This correlates well with computational results from Krishnan [19] that show tendencies for void growth in grains with low Taylor factors along the shock directions due to their ability to more easily accommodate plastic deformation, which is drives void growth. It is also noteworthy that Minich et al. found higher spall strength in single crystal Cu oriented at <0 0 1> with the shock direction than in <1 0 1> or <1 1 1> [5]. The results here seem to reflect this heirarchy of spall strength as <1 0 1> and <1 1 1> have high Taylor factors and had transgranular voids present, whereas no <0 0 1> or other orientations with low Taylor factors were found to nucleate damage. All of these observations suggest that there may be differences in the behavior of damage nucleation vs. growth for grains of high and low Taylor factors along the shock direction and requires further experimental and computational investigations.

6.5 Post Mortem Analysis of Surface Perturbation Samples

It was seen by Krishnan [19] that strain localized next to GBs in the spall plane correlate quite well with nucleated damage at the same site. It is of interest to analyze how strain localizes at and next to GBs away from the spall plane to study strain hardening effects from the shock loading process. Adding a step function, or sinusoidal ripples, to the diagnostic free surface provides insight into how this strain localization occurs. Take the case of a sinusoidal ripple for example: it is theorized that once the shock wave reaches the free surface the shock front will deform the material while traction free conditions are met at the free surface. During this process it is expected from Richtmyer-Meshkov (RM) instability simulations [96] that for a perfectly elastic system the sinusoidal profile would become shifted by $\pi/2$ (become a cosine profile) and what were previously valleys become peaks as the wave was traveling to the free surface before reflecting. It is of interest to see how changes in amplitude of the surface perturbations are affected by anisotropy, which would provide insight to how grain orientation affects interactions of wave reflection at the interface with and without PMMA windows and what directions are more and less resistant to deformation.

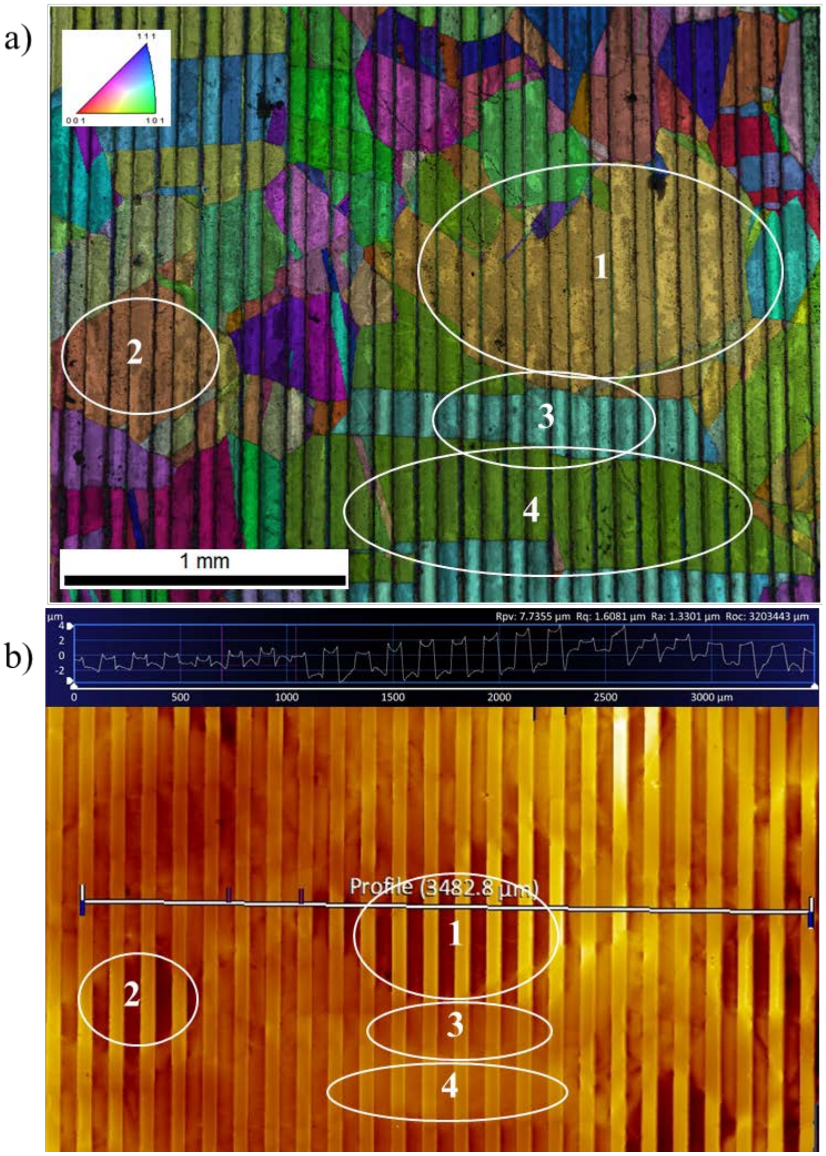

Figure 57: (a) IPF map and b) optical profilometry views of the diagnostic surface of a shocked Cu MC with surface perturbations. Numbered and circled grains in the IPF map correspond to the regions of the same number in the profilometry data.

Sample 23957, shown in Figure 57, is a quasi-columnar copper MC specimen with an average grain size of 800μm and a square wave on the diagnostic surface of a 150 μm wavelength and original uniform height of 10 μm, or, amplitude of 5μm. The orientations of grains 1, 2, 3, and 4 parallel to the shock direction were found to be close to: <0 1 3>, <0 1 3>, <0 3 5>, and <1 3 3>, respectively. The <0 1 3> direction is ~22° from <0 0 1> along the <0 0 1>-<1 0 1> edge of the standard triagle and <0 3 5> and <1 3 3> are ~15° from <1 0 1>. The Taylor factors along the <0 0 1> and similar directions are low while the Taylor factors along the <1 0 1> and similar directions are high. The residual amplitudes of the square wave were determined via optical profilometry and are plotted in Figure 58 for all four grains. It was found that grains 1 and 2 had residual amplitudes of 2.5 μm, whereas grains 3 and 4 had residual amplitudes of 1.5 μm.

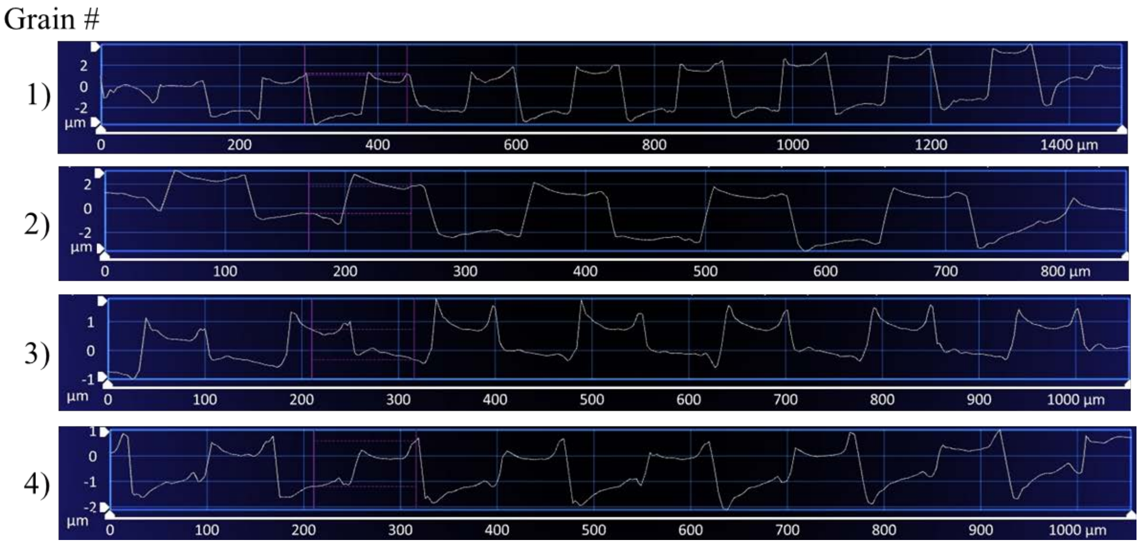

Figure 58: Residual amplitudes of square waves across four grains of interest.

It was shown by Peralta et al [97] that the yield stresses associated with amplitude changes similar to that of the <0 0 1> and <1 0 1> grains analyzed here were 200 MPa for the largest residual amplitude and 120 MPa for the smallest one, corresponding to the approximate yield strength values measures for <1 0 0> and <1 1 1>/<1 0 1> Cu single crystals, respectively [98]. The finite element simulations indicate that the presence of a PMMA window against the diagnostic surface leads to enhanced pressure gradients that amplify the RM instability at low pressures by an order of magnitude, and at low pressures the deformation is likely to be more sensitive to anisotropy and plasticity.

Sample 23944 was another shocked MC containing surface perturbations of the same wavelength and amplitude of sample 23957. Sample 23944 was cross-sectioned to inspect possible changes in crystallographic orientations near the diagnostic surface containing the square wave profile and to analyze spall damage within the material. Figure 59 shows a through-thickness cross-section with regions of interest highlighted for crystallographic analysis. Note that there is no spall damage present in the specimen though MC and PC specimens shot at similar pressures did show spall damage.

Figure: 59: IPF map of shocked sample 23944 with surface perturbations on the diagnostic surface with areas of interest for crystallographic analysis circled in black.

The orientations parallel to the shock direction for each section highlighted in Figure 59, from left to right, are: <1 1 3>, <1 13 14>, <11 16 19> and <6 7 10>, and <3 8 29>. Each region was scanned at a resolution of 1 µm step size as compared to 4µm for the overall scan of the cross-section. These scans are shown in Figures 60-63 along with the plane traces for the {1 1 1} planes and {1 1 0} planes to elucidate the presence of misorientation bands indicative of activated slip. The length of the lines showing the plane traces are proportional to the inclination of the plane; the more inclined the plane relative to the same surface the longer the trace is drawn by the software [79].

a) {1 1 1} Plane Traces

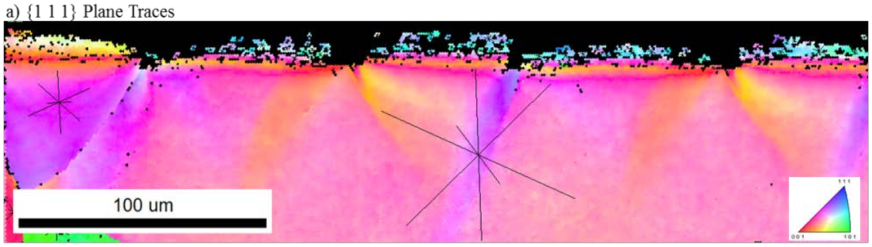

b) {1 1 0} Plane Traces

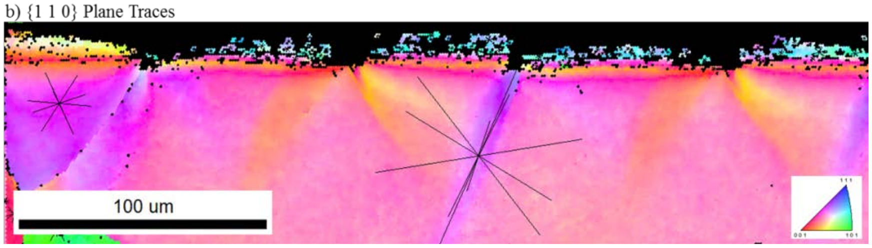

Figure 60: IPF map of the <1 1 3> oriented grain showing plastic deformation following the periodicity of the surface perturbations.

Figure 60 shows the IPF map of the <1 1 3> oriented grain, which presents regions of misorientations aligning with {1 1 0} plane traces. Slip bands would be expected to follow the {1 1 1} plane trace in FCC materials, however they do not align with the misorientated regions. It is possible to have slip along {1 1 0} in FCC materials subject to high strain rate deformation, such as shock loading, but this would be an unexpected discovery for the low pressure conditions this sample was shot. The reason behind not ruling this out without further investigation is the RM instability interactions at the surface with a PMMA window producing enhanced pressure gradients may lead to non-octahedral glide within the material [99].

a) {1 1 1} Plane Traces

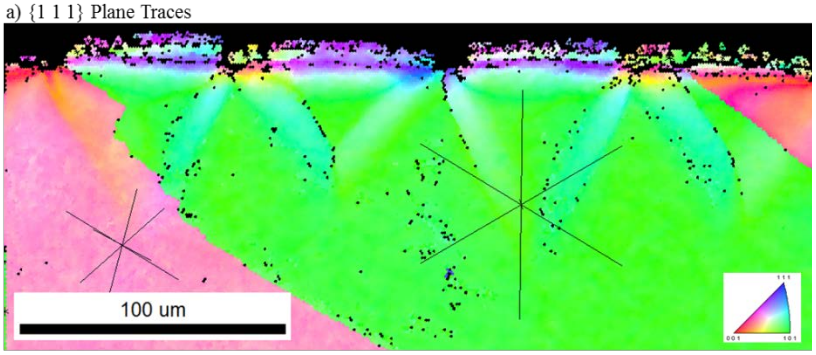

b) {1 1 0} Plane Traces

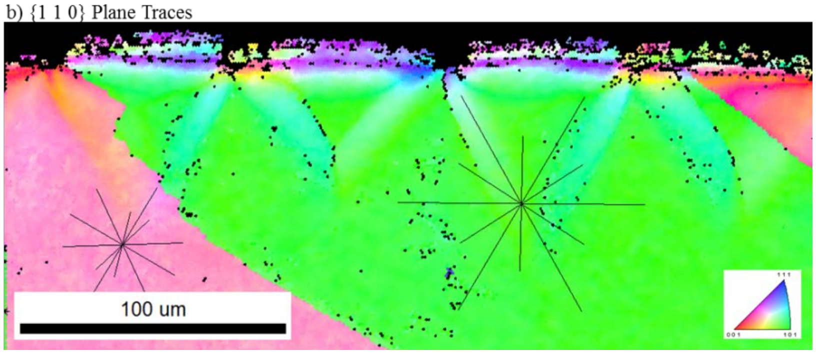

Figure 61: IPF map of the <1 13 14> oriented grain showing plastic deformation following the periodicity of the surface perturbations.

Figure 61 shows the IPF plot of the near <0 1 1> orientation twin grain. Once again, the lattice rotation bands follow plane traces follow {1 1 0} and show no resemblance to the {1 1 1} plane traces. Figure 62 again shows the <11 16 19> and <6 7 10> oriented grains, both close to <1 1 1>, aligning the misoriented regions with {1 1 0} plane traces. Only in Figure 63 for the <3 8 29> oriented grain, ~16° from <0 0 1>, do the plane traces of the {1 1 1} plane traces remotely resemble the alignment of the lattice rotation bands, though it seems that there are {1 1 0} plane traces that better fit each instance.

a) {1 1 1} Plane Traces

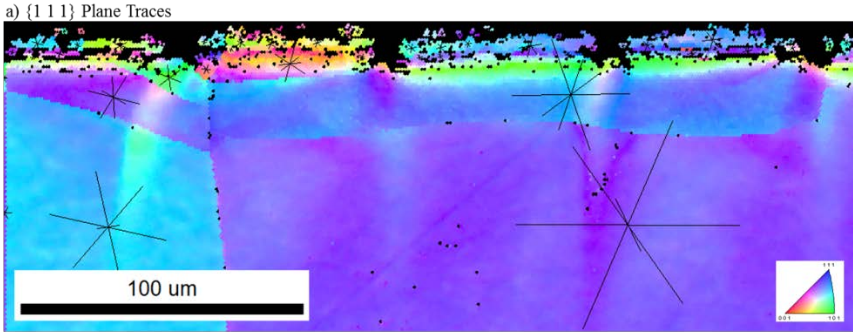

b) {1 1 0} Plane Traces

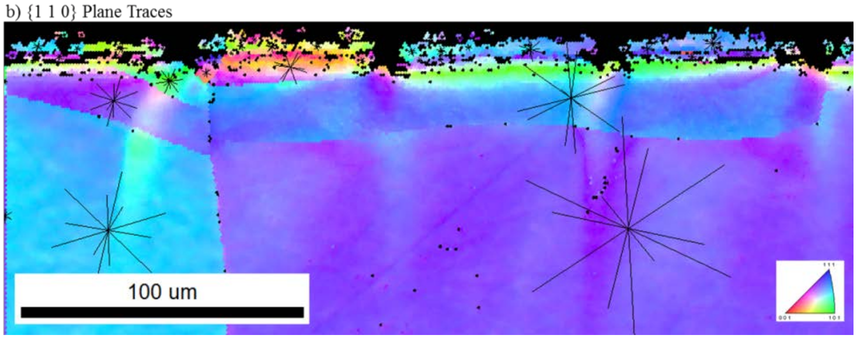

Figure 62: IPF map of the <11 16 19> and <6 7 10> oriented grains showing plastic deformation following the periodicity of the surface perturbations.

a) {1 1 1} Plane Traces

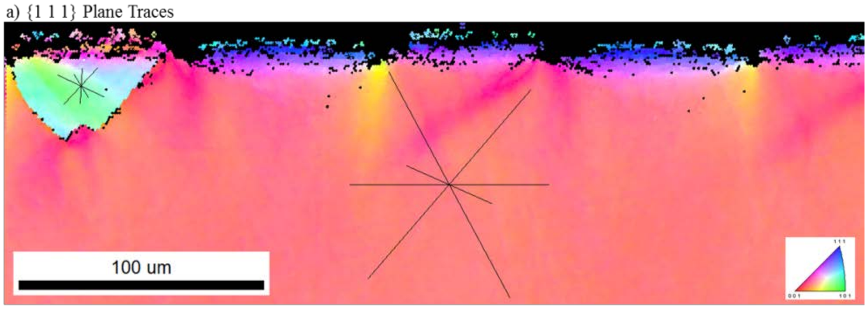

b) {1 1 0} Plane Traces

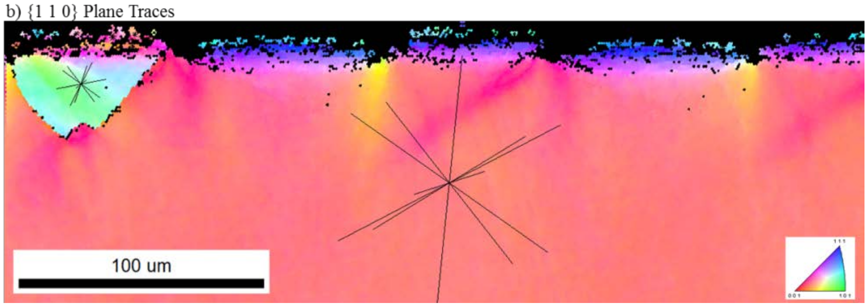

Figure 63: IPF map of the <3 8 29> oriented grain showing plastic deformation following the periodicity of the surface perturbations.

PC copper specimen 24745 containing surface perturbations with a wavelength of 100μm was shock loaded and cross-sectioned from a possible spall signature seen on its VISAR history. Figure 63 shows optical microscopy images of the spall plane as well as an IPF map overlay. The spall damage shows significant growth compared to the size of the grains, which seem to have heavy texture along the <0 0 1>-<1 1 1> side of the standard triangle caused by the heat treatment prior to testing. The voids also appear to be elongated in the direction of the shock and exist periodically along the width of the spall plane, possibly mimicking the periodicity of the surface perturbations.

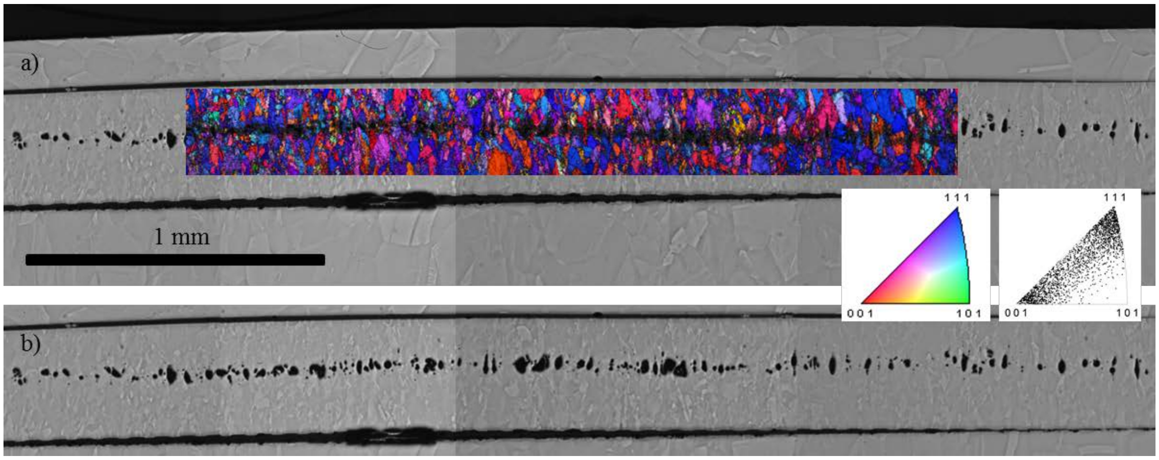

Figure 64: Optical microscopy and IPF map overlay of the spall plane in sample 24745.

The work presented in this chapter is meant to give direction for future studies on RM behavior in shocked metallic materials and provides a proof on concept for the underlying physics behind this phenomenon as it pertains to anisotropy, crystal plasticity, and spall damage.

7. CONCLUSIONS

The flyer-target impact experiments and extensive 2-D and 3-D data analysis performed on copper polycrystals of varying thermomechanical histories, copper multicrystals, and copper poly- and multicrystals containing surface perturbations led to the following conclusions:

- 2-D statistics on damage present at boundaries of varying misorientations was conducted to find which GBs are resistant or susceptible to containing damage. Shocked copper polycrystals of three different thermomechanical processing histories were studied to determine if the damage present at GBs depends only on the material in question (copper) or if the microstructures strongly influence where damage is present within the samples. Critical steps in the data analysis procedure for finding the probability of a GB of a given misorientation angle to contain damage, or, $P(X = 1|\theta)$, were developed in this work that are not present in available studies: consistently defining a spall region bounded by the upper and lowest voids and probing every boundary within that region to obtain the real probabilities for boundaries with and without damage and normalizing damaged boundaries with the texture of the sample within the spall region.
    - From the 2-D statistics it was found that the as received (AR), heat treated (HT), and fully recrystallized (FR) specimens all had the highest probability to find a misorientation angle containing damage in the 25° to 50° range, indicating that a characteristic for damage nucleation at random high angle GBs is a property of the material. It was determined that

    damage was unlikely to nucleate at {111} Σ3 twin boundaries; however, damage was abundantly present at the tips of twins terminated at GBs, which are likely not {111} Σ3s but random high angle boundaries.

  - The AR specimens contained a more pronounced peak in the 25° to 50° misorientation range than in the HT and FR specimens. This suggests that the plasticity present in the grain bulk was responsible for the incipient nature of the damage within the AR specimens and forcing damage to nucleate at the weak links in the microstructure, the GBs, and allowing for their strength to dominate where damage localized. The HT and FR specimens contained less incipient and intergranular spall damage due to the weakening of the grain bulks via the removal of plasticity from heat treatments and allowing for damage to nucleate where the stress state of the material was high enough, leading to a decreased influence from the local microstructure on damage nucleation within the material.

- 3-D X-ray tomography (XRT) data was collected for each microstructure type analyzed in the 2-D statistical study of GB strength to determine the amount of inter- vs. transgranular damage found within each specimen and to develop a nondestructive technique to determine the damage modes present in a shocked specimen. Through visual inspection and shape fitting each individual void from the data sets to best fit ellipsoids it was found that the AR microstructure type contained a ~55% or greater fraction of voids of sheet, or, disc-like shape indicative of intergranular damage and less than 7% fraction of spherical voids indicative of transgranular damage. The HT and FR specimens were found to contain ~47% and ~35% fraction of transgranular damage, ~12% and ~15% fraction of intergranular damage, and ~41% and ~50% fraction of coalesced damage, respectively.

  - It is confirmed from the 2-D statistics that the FR specimen is the least incipient of those studied; meaning that local microstructure had the least effect on where spall damage was found in the material, although the likely preferred damage mode for nucleation was transgranular. The HT specimens showed a transgranular damage mode preference, elucidating and confirming the lessened influence of the GB misorientation on the presence damage seen in the 2-D statistics. It is concluded that plasticity present within the grain bulk leads to an increase in intergranular damage, thus leading to an increased influence of GB strength on finding damage at boundaries.

- Large volume, intergranular damage sites were studied in copper multicrystals in 3-D to provide additional information on what makes these GBs microstrucural weak links in the material. A 3-D reconstruction of the microstructure is the only means to determine the physical GB normal, which is needed as one of 5 parameters to fully characterize a GB. The Taylor factor mismatch along the shock direction and crystallographic GB normal were analyzed along with the misorientation angle and angle between the GB normal and shock direction to elucidate what makes a GB intrinsically weak. It was found that large Taylor factor mismatches for either the shock direction or crystallographic GB normal are favorable for void nucleation, however, the Taylor factor mismatch along the crystallographic GB normal coupled with GB strength / misorientation angle appears to be the primary relationship driving void nucleation. It was also seen that high values of the Taylor factor along the shock direction drives void growth, consistent with simulations by Krishnan [19]. The angle between the shock direction and the GB physical normal encouraged higher volume void growth in the ranges of ~30°-45°. Although additional data is required to make these conclusions statistically sound, the contributions from this study will aide computational efforts of studying GB responses to shock loading.

- Incipient inter- and transgranular damage sites were studied in shocked copper multicrystals via FIB sectioning coupled with EBSD to determine the extent of plastic affected zones around the damage sites in 3-D and interactions these zones have with surrounding damage sites. The orientation surrounding the grains were analyzed with IPF maps and the lattice rotations from the plastic zones were captures with local average misorientation and grain reference orientation deviation maps. It was found from the three FIB sectioned areas and four individual incipient damage sites ranging from 10µm to 18µm in diameter their plastic zone influence extended 25% to 50% of the average void diameter in 3-D.
    - The plastic zone surrounding the voids contained regions or higher misorientations than others, but never greater than ~5° for local average misorientations. There was inconclusive evidence for the effect the Taylor

    factor has on lattice deformation orientation; though there were several examples of dislocation cell directions aligning with high Taylor factor directions. Transgranular incipient spall was present in grains with a high Taylor factor along the shock direction, in correlation with findings by Krishnan [19] that grains associated with low Taylor factors along the shock direction experience significant void growth due to their higher accommodation for plastic deformation.

- Development and implementation of a fabrication process to use photolithography combined with chemical etching to create periodic square waves on the diagnostic free surface of copper target discs was achieved. Richtmyer-Meshkov instability at the free surface interface produced enhanced pressure gradients at the free-surface PMMA window interface, leading to larger than predicted changes in amplitude of the square wave. Amplitudes prior to testing were uniformly 5µm with a wavelength of 150µm for the MC samples tested. It was found that grains close to <0 0 1> with the shock had residual amplitudes of 2.5µm, whereas grains close to <1 0 1> with the shock had residual amplitudes of 1.5µm. These results are an order of magnitude larger than predicted and are obviously affected by anisotropy.
    - Cross sections of a shocked MC specimen with surface perturbations were taken and scanned using EBSD to investigate the extent of plastic deformation at the interface. It was found that for every orientation investigated the {1 1 0} plane traces were aligned with the direction of the

misoriented regions and not along {1 1 1} plane traces indicative of slip in FCC metals. There was no spall damage found in either MC specimen. Spall damage was found in a heavily <0 0 1>, <1 1 1> textured heat treated copper PC containing surface perturbations. From optical microscopy and EBSD it was clear that the spall damage had grown beyond the incipient stage and was elongated along the shock direction with periodicity in the clustering of damage similar to the length scale of the perturbation wavelength.

8. FUTURE WORK

- Implementation of GB strength from the 2-D statistics study found in this work into a continuum damage mechanics model with crystal plasticity is needed to develop better predictive models for damage nucleation in simulated or reconstructed microstructures. Additional statistics for more incipiently spalled HT and FR specimens would go a long way to undoubtedly conclude damage mode preference for transgranular damage and coalescence is a property of these microstructures and not void volume fraction.
- 2-D statistics and 3-D spall zone renderings from XRT in materials other than copper should be performed in a similar vein to the procedures outlined here to determine GB strengths and damage mode preference for at least one other FCC metal, a BCC metal, and an HCP metal. This would provide more global trends for wider use for computational studies and the field of GB engineering.
- Many more instances of large volume damage sites need to be explored in shocked copper MCs to determine what combination of the following sets up the ideal conditions for a weak boundary: Taylor factors along the shock and crystallographic GB normal, misorientation angle, and angle between the shock direction and GB normal. Additionally, one more measureable parameter should be explored and added to the study since it is required to have 5 parameters to accurately describe a GB.

- Data exists for more than three FIB sectioning sites from shocked MCs. This data needs to be explored in a similar vein to the data explored in this work. In depth characterization of the ligaments extending from the intergranular damage sites for all data sets should be pursued in a similar fashion to the transgranular sites examined in this work. Additionally, it is of interest to incorporate the Nye Tensor into the analysis process to directly describe the strain fields fully in 3-D.
- This work lays the foundation for future experiments and analysis for shock loading of target samples containing surface perturbations to investigate Richtmyer-Meshkov instabilities in solids. Analysis of the plasticity along the diagnostic surface is necessary to obtain information on how GBs deform the material adjacent to them without unwanted deformation from wave interactions. Exploring the behavior of spall damage nucleation and growth due to the presence of the surface perturbations is unknown and must be explored. The data in this work suggests that when spall occurs within a specimen there is an effect on the spall plane from the perturbations.

REFERENCES

[1] M.A. Meyers, *Dynamic Behavior of Materials*, John Wiley & Sons, New York, 1994.

[2] Meyers, M.A. and C.T. Aimone, *Dynamic Fracture (Spalling) of Metals.* Prog. Mat. Sci., 1983. **28**: p. 1-96.

[3] D.R. Curran, L. Seaman, D.A. Shockey, Phys. Rep. vol. 147, 1987.

[4] D.E. Grady, J., The Spall Strength of Condensed Matter, J.Mech. Phys. Sol., vol. 36, no 3, pp. 353–384, 1988.

[5] Minich, R.W., Cazamias, J.U., Kumar, M. and Schwartz, A.J., "Effect of Microstructural Length Scales on Spall Behavior of Copper", Metall. Mater. Trans. A, vol. 35A, no. 9, pp. 2663–2673, 2004.

[6] Chen, X., Asay, J.R., Dwivedi, S.K. and Field, D.P., "Spall Behavior of Aluminum with Varying Microstructures", J. Appl. Phys., vol. 99, pp. 1–13, 2006.

[7] Gray, G.T., N.K. Bourne, J.C.F. Millet, and M.F. Lopez. *Influence of Shock-Wave Profile Shape ("Taylor-Wave Versus Square-Topped) on the Shock-Hardening and Spallation Response of 316L Stainless Stell.* in *Shock Compression of Condensed Matter 2003*. 2003. American Institute of Physics.

[8] Gray, G.T., N.K. Bourne, B.L. Henrie, and J.C.F. Millett, *Influence of shock-wave profile shape (triangular- "Taylor-wave" versus square-topped) on the spallation response of 316L stainless steel.* Journal De Physique Iv, 2003. **110**: p. 773-778.

[9] Koller, D.D., R.S. Hixson, G.T. Gray III, P.A. Rigg, L.B. Addessio, E.K. Cerreta, J.D. Maestas, and C.A. Yablinsky, *Influence of shock-wave profile shape on dynamically induced damage in high-purity copper.* J. Appl. Phys., 2005. **98**: p. 103518-1-7.

[10] Peralta, P., S. DiGiacomo, S. Hashemian, S.-N. Luo, D.L. Paisley, R. Dickerson, E. Loomis, D. Byler, K.J. McClellan, and H. D'Armas, *Characterization of Incipient Spall Damage in Shocked Copper Multicrystals.* Int. J. Damage, 2009. **18**: p. 393-413.

[11] Vignjevic, R., N.K. Bourne, J.C.F. Millet, and T. De Vuyst, *Effects of Orientation on the Strength of the Aluminum Alloy 7010-T6 During Shock Loading: Experiment and Simulation.* J. Appl. Phys., 2002. **92**(8): p. 4342-4348.

[12] Hashemian, S., S. DiGiacomo, P. Peralta, H. D'Armas, S.-N. Luo, E. Loomis, D.L. Paisley, R. Dickerson, D. Byler, and K.J. McClellan. *Effects of Microstructure on Spall*

Damage Localization in Shock Loaded Copper Multicrystals. in *TMS Annual Meeting*. 2008. New Orleans, LA: TMS.

[13] Perez-Bergquist, A.G., E.K. Cerreta, C.P. Trujillo, F. Cao, and G.T. Gray, *Orientation dependence of void formation and substructure deformation in a spalled copper bicrystal.* Scripta Materialia, 2011. **65**(12): p. 1069-1072.

[14] Escobedo, J.P., E.K. Cerreta, D.D. Koller, *Effect of Crystalline Structure on Intergranular Failure During Shock Loading.* JOM, 2014. **66**(1): p. 156-164

[15] Escobedo, J.P., D. Dennis-Koller, E.K. Cerreta, B.M. Patterson, C.A. Bronkhorst, B.L. Hansen, D. Tonks, and R.A. Lebensohn, *Effects of grain size and boundary structure on the dynamic tensile response of copper.* Journal of Applied Physics, 2011. **110**(3): p. 033513.

[16] S. DiGiacomo, Mechanical and Aerospace Engineering, Arizona State University, Tempe, AZ, 2008, Master of Science.

[17] S. Hashemian, Mechanical and Aerospace Engineering, Arizona State University, Tempe, AZ, 2008, Master of Science.

[18] L. Wayne, Mechanical and Aerospace Engineering, Arizona State University, Tempe, AZ, 2009, Master of Science.

[19] K. Krishnan, Mechanical and Aerospace Engineering, Arizona State University, Tempe, AZ, 2013, PhD.

[20] Wayne, L., Krishnan, K., DiGiacomo, S., Kovvali, N., Peralta, P., Luo, S.-N., Greenfield, S., Byler, D., Paisley, D., McClellan, K.J., Koskelo, A., Dickerson, R., 2010. *Statistics of weak grain boundaries for spall damage in polycrystalline copper.* Scripta metall. 63, 1065-1068.

[21] Cerreta, E.K., Escobedo, J.P., Perez-Bergquist, A., Koller, D.D., Trujillo, C.P., Gray Iii, G.T., Brandl, C., Germann, T.C., 2012. *Early stage dynamic damage and the role of grain boundary type.* Scripta Materialia 66, 638-641.

[22] Brown, A.D. , K. Krishnan, L. Wayne, P. Peralta, S.N. Luo, D. Byler, B. Patterson, *3-D Characterization of Global and Local Microstructural Effects on Spall Damage in Shock Loaded FCC Metals: Experimental and Modeling.* ASME IMECE, San Diego, CA, 2013. P. 65642.

[23] Brown, A.D., L. Wayne, Q. Pham, K. Krishnan, P. Peralta, S.N. Luo, B. Patterson, S. Greenfield, D. Byler, K.J. McClellan, A. Koskelo, R. Dickerson, X. Xiao,

Microstructural Effects on Damage Nucleation in Shock-Loaded Polycrystalline Copper. Metall. and Mat. Trans A., 2014.

[24] Krishnan, K., A. Brown, L. Wayne, J. Vo, S. Opie, H. Lim, P. Peralta, S.N. Luo, D. Byler, K.J. McClellan, A. Koskelo, R. Dickerson, *Three-Dimensional Characterization and Modeling of Microstructural Weak Links for Spall Damage in FCC Metals.* Metall. and Mat. Trans A., 2014.

[25] Czarnota, C., N. Jacques, S. Mercier, and A. Molinari, *Modeling of Dynamic Ductile Fracture and Application to the Simulation of Plate Impact Tests on Tantalum.* J. Mech. Phys. Sol., 2008. **56**: p. 1624-1650.

[26] Czarnota, C., S. Mercier, and A. Molinari, *Modelling of Nucleation and Void Growth in Dynamic Pressure Loading, Application to Spall Test on Tantalum.* Int. J. Fract., 2006. **141**: p. 177-194.

[27] Molinari, A. and T.W. Wright, *A Physical Model for Nucleation and Early Growth of Voids in Ductile Materials Under Dynamic Loading.* J. Mech. Phys. Sol., 2005. **53**: p. 1476-1504.

[28] Boidin, X., P. Chevrier, J.R. Klepaczko, and H. Sabar, *Identification of Damage Mechanism and Validation of a Fracture Model Based on Mesoscale Approach in Spalling of Titanium Alloy.* Int. J. Solid Struct., 2006. **43**(4595-4615).

[29] Han, W., An, Q., Luo, S., Germann, T., Tonks, D., Goddard, W., 2012. *Deformation and spallation of shocked Cu bicrystals with Σ3 coherent and symmetric incoherent twin boundaries.* Physical Review B 85.

[30] Lin, E.Q., Shi, H.J., Niu, L.S., Jin, E.Z., 2012. Shock response of copper bicrystals with a Σ3 asymmetric tilt grain boundary. Computational Materials Science 59, 94-100.

[31] Meyers, M.A., *A model for Elastic Precursor Waves in the Shock Loading of Polycrystalline Materials.* Mater. Sci. Eng., 1977. **30**(2): p. 99-111.

[32] Martineau, R.L., A Viscoplastic Model of Expanding Cylindrical Shells Subjected to Internal Explosive Detonations. 1998.

[33] Loomis, E., Peralta, P., Swift, D.C., Modeling of Elastic Waves in Dynamically Loaded NiAl Bicrystals. J. Eng. Mat. Tech., 127, 513-522, 2007.

[34] Graef, M.D., McHenry, M.E., Structure of Materials: An Introduction to Crystallography, Diffraction, and Symmetry. New York: Cambridge. 2007.

[35] E. Loomis, Mechanical and Aerospace Engineering, Arizona State University, Tempe, AZ, 2005, PhD.

[36] Isbell, W.M., Measuring the Dynamic Response of Materials. London: Imperial College Press. 2005.

[37] Luo, S.N., et al., High Pressure Research, 24, p. 409. 2004.

[38] Antoun, T., Seaman, D., Curran, R., Kanel, G., Razorenov, S.V., Utkin, A.V., Spall Fracture. Springer, New York. 2003.

[39] Kanel, G.I., Rasorenov, S.V., Fortov, V.E., Shock-wave and High-strain-rate Phenomena in Materials. Marcel Dekker. 1992.

[40] Christy, S., Pak, H.R., Meyers, M.A., Metallurgical Applications of Shock-Wave and High-strain-rate Phenomena. Marcel Dekker, New York. 1986.

[41] Moshe, E. et al., Journal Applied Physics, 83, 4004. 1998.

[42] Buchar, J., Elices, M., Cortez, R., Journal de Physique IV, 1, 623. 1991.

[43] Fortov, V.E., Kostin, V.V., Journal Applied Physics, 70, 4524. 1991.

[44] Lim, Y.S., Kim, J.S., Kim, H.P., Cho, H.D., Journal of Nuclear Materials, 335, 108. 2004.

[45] DeHoff, R.T., Metallography, 8, 71. 1975.

[46] Uchic, M.D. et al., MRS Bulletin, 32, 408. 2007.

[47] Bingert, J.F., Henrie, B.L., Worthington, D.L., 2007. *Three-Dimensional Characterization of Incipiently Spalled Tantalum.* Metall. Mater. Trans. A 38A, 1712-1721.

[48] Henrie, B.L., Mason, T.A., Bingert, J.F., *Investigating incipiently spalled tantalum through multiple section planes and serial sectioning.* Shock Compression of Condensed Matter, 2005.

[49] Gurson, A.L., *Continuum theory of ductile rupture by void nucleation and growth: part I – yield criteria and flow rules for porous ductile media.* J. Eng. Mater. Technol., 1977. **99**: p. 2 -15.

[50] Tvergaard, V., *Influence of voids on shear band instabilities under plane strain condition.* Int'l J. Fract. Mech., 1981. **17:** p. 389-407.

[51] Needleman, A., *A Continuum Model for Void Nucleation by Inclusion Debonding.* J. of App. Mech., 1987. **54**(3): p. 525-531.

[52] Tong, W., G. Ravichandran, *Inertial Effects on Void Growth in Porous Viscoplastic Materials.* J. Appl. Mech., 1995. **62**: p. 633-639.

[53] Ortiz, M., A. Molinari, *Effect of strain hardening and rate sensitivity on the dynamic growth of a void in a plastic material.* J. Appl. Mech., 1992. **59:** p. 48-53.

[54] Czarnota, C., N. Jacques, S. Mercier, and A. Molinari, *Modeling of Dynamic Ductile Fracture and Application to the Simulation of Plate Impact Tests on Tantalum.* J. Mech. Phys. Sol., 2008. **56**: p. 1624-1650.

[55] Roy, G. *Vers une mmodélisation approfondie de l'endommagement ductile dynamique. Investigation expérimentale d'une nuance de tantale et développements théoriques,* in *EcoleNationale Supérieure de Mécanique et d'Aéronautique.* 2003, Université de Poitiers.

[56] Trumel, H., F. Hild, G. Roy, Y.P. Pellegrini, C. Denoual, *On Probabilistic aspects in the dynamic degradation of ductile materials.* J. Mech. and Phys. Solids, 2009. **57:** p. 1980-1998.

[57] Lebensohn, R.A., M.I. Idiart, P.P. Castaneda, P.G. Vincent, *Dilatational viscoplasticity of polycrystalline solids with intergranular cavities.* Philosophical Magazine, 2011. **91**(22): p. 3038-3067.

[58] Lebensohn, R.A., J.P. Escobedo, E.K. Cerreta, D.D. Koller, C.A. Bronkhurst, J.F. Bingert, *Modeling void growth in polycrystalline materials.* Act. Mater., 2013. **61:** p. 6918-6932.

[59] Becker, R., *Effect of Crystal Plasticity on Materials Loaded at High Pressures and Strain Rates.* Int. J. Plast., 2004. **20**: p. 1983-2006.

[60] Lukyanov, A.A., *Constitutive Behaviour of Anisotropic Materials under Shock Loading.* Int. J. Plast., 2008. **24**: p. 140-167.

[61] Luscher, D.J., C.A. Bronkhorst, C.N. Alleman, F.L. Addessio, *A model for finite-deformation nonlinear thermomechanical response of single crystal copper under shock conditions.* J. Mech. Phys. Sol., 2013. **61:** p. 1877-1894.

[62] Lloyd, J.T., J.D. Clayton, R. Becker, D.L. McDowell, *Simulation of shock wave propagation in single crystal and polycrystalline aluminum.* Int. J. Plast., 2014. **60:** p. 118-144.

[63] Potirniche, G.P., M.F. Horstemeyer, X.W. Ling, *An internal state variable damage model in crystal plasticity.* Mech. Mater., 2007. **39:** p. 941-952.

[64] Vignjevic, R. N. Djordjevic, J. Campbell, V. Panov, *Modelling of dynamic damage and failure in aluminum alloys.* Int. J. Impact Eng., 2012. **49:** p. 61-76.

[65] Potirniche, G.P., J.L. Hearndon, M.F. Horstemeyer, X.W. Ling, *Lattice orientation effects on void growth and coalescence in FCC single crystals.* Int. J. Plast., 2006. **22:** 921-942.

[66] Stevens, A.L., L. Davison, and W.E. Warren, *Spall Fracture in Aluminum Monocrystals: A Dislocation-Dynamics Approach.* J. Appl. Phys., 1972. **43**(12): p. 4922-4927.

[67] Clayton, J.D., *Modeling dynamic plasticity and spall fracture in high density polycrystalline alloys.* Int. J. Sol. Struct., 2005. **42:** p. 4613-4640.

[68] Vogler, T.J., J.D. Clayton, *Heterogeneous deformation and spall of an extruded tungsten alloy: plate impact experiments and crystal plasticity modeling.* J. Mech. Phys. Solids, 2008. **56:** p. 297-335.

[69] Traiviratana, S., E.M. Bringa, D.J. Benson, M.A. Meyers, *Void growth in metals: Atomistic calculations.* Acta Mater., 2008. **56:** p. 3874-3886.

[70] Belak, J., *On the nucleation and growth of voids at high strain-rates.* J. Computer-Aided Mats. Des., 1998. **5:** p. 193-206.

[71] Rudd, R. J.F. Belak, *Void nucleation and associated plasticity in dynamic fracture of polycrystalline copper: an atomistic simulation.* Comp. Mat. Sci., 2002. **24:** p. 148-153.

[72] Zhao, K.J., C.Q. Chen, Y.P. Shen, T.J. Lu, *Molecular dynamics study on the nano-void growth in face-centered cubic single crystal copper.* Comp. Mat. Sci., 2009. **46:** p. 749-754.

[73] Seppala, E.T., J. Belak, R.E. Rudd, *Three-dimensional molecular dynamics simulations of void coalescence during dynamic fracture of ductile materials.* Phys. Rev. B, 2005. **71:** 064112.

[74] Madou, K., J.B. Leblond, *A Gurson-type criterion for porous ductile solids containing arbitrary ellipsoidal voids – I: Limit-analysis of some representative cell.* J. Mech. Phys. Sol., 2012. **60:** p. 1020-1036

[75] Madou, K., J.B. Leblond, *A Gurson-type criterion for porous ductile solids containing arbitrary ellipsoidal voids – II: Determination of yield criterion parameters.* J. Mech. Phys. Sol., 2012. **60:** p. 1037-1058

[76] D.E. Grady, M.E. Kipp, High Pressure Shock Compression of Solids, Springer-Verlag, New York, 1993.

[77] Dolan, D.H., Foundations of VISAR Analysis, Sandia Report, 2006.

[78] P. A. Midgley, (University of Cambridge, U.K., 2008).

[79] EDAX-TSL, (2007), Vol. 5.2.

[80] B.M Patterson, J.P. Escobedo, D. Dennis-Koller, E. Cerreta, Microsc. Microanal. 18 (2012) 390.

[81] N.L. Johnson, Biometrika 36 (1949) 149.

[82] H.H. Ku, J. Res. Nat. Bur. Stand. 70C (1966) 263.

[83] B.M Patterson, J.P. Escobedo, D. Dennis-Koller, E. Cerreta, Microsc. Microanal. 18 (2012) 390.

[84] Li, Q., Griffiths, J.G., *Least Squares Ellipsoid Specific Fitting*, Proceedings of the Geometric Modeling and Processing, 2004.

[85] Wang, L., Park, J.P., Fu, Y, *Representation of real particles for DEM simulation using X-ray tomography.* Constr. Building Mats., 2007. **21:** p.338-346

[86] Avizo

[87] D.G. Brandon: Acta Metall., 1966, vol. 14, pp. 1479–84.

[88] V. Randle: Interface Sci., 2002, vol. 10, pp. 271–77.

[89] J.K. MacKenzie: Biometrika, 1958, vol. 45, pp. 229–40.

[90] A.P. Sutton and R.W. Ballufi: Interfaces in Crystalline Materials, Oxford University Press, New York, 1995.

[91] H. Kaneko, M. Hasunuma, A. Sawabe, T. Kawanoue, Y. Kohanawa, S. Komatsu and M. Miyauchi, *Proc. IEEE/IRPS*, (1990), 194.

[92] H. Gleiter and B. Chalmers, *Progress in Material Science*, *16,* (1972), 77.

[93] J. A. Nucci, R. R. Keller, D. P. Field and Y. Shacham-Diamand, *Appl. Phys. Lett.*, *70*, (1997), 1242.

[94] W. T. Read and W. Shockley, *Physical Review*, *78*, (1950), 275.

[95] Chin, G.Y., Mammel, W.L., *Computer Solutions of the Taylor Analysis for Axisymmetric Flow*. Transactions of the Metallurgical Society, 1967. AIME 239, 1400-1405.

[96] Piriz, A.R., Cela, J.J., Richtmyer-Meshkov Instability in Elastic-Plastic Media. Physical Review E, 78, 2008. [97] Peralta, P., Chen, Y., Brown, A., McDonald, R., Krishnan, K., Lim, H., Loomis, E., *Richtmyer-Meshkov Instability in FCC Metals at Low Shock Pressures: Effects of Release Windows and Material Anisotropy*. Philosophical Magazine Letters. 2015. Submitted.

[98] Jones, O.E. and Motes, J.D., J Appl. Phys., 1969. **40**(12), p. 4920-4928.

[99] Caillard, D., Martin, Jean-Luc., *Glide of Dislocations in Non-Octahedral Planes in FCC Metals: A Review*. Int. J. Mat. Res. (formerly Z. Metallkd.) 100 (2009), p. 1403-1410.

[100] Fensin, S.J., Escobedo, J.P., Brandl, C., Cerreta, E.K., Gray III, G.T., Germann, T.C., Valone, S.M., *Effect of loading direction on grain boundary failure under shock loading*. Acta Mater., 2014. Vol. 64, p. 113-122.

APPENDIX A

MATLAB CODE FOR ELLIPSOID SHAPE FITTING USING SURFACE NODES

```
%Andrew Brown
%Surface Point Ellipsoid Solver
%Refer to reference 84, Li et al. for theory guidance

syms x y z xo yo zo a b c h f g

clear all
clc

nmax = 2360;
nvoids = 364;
mat = zeros(nmax,10*nvoids);
mat2 = zeros(nmax,4);

for n=0:(nvoids-1)

L = load('20357aspects.csv');
x = L(:,1+3*n);
y = L(:,2+3*n);
z = L(:,3+3*n);

for q=1:nmax

    if (x(q)== 0) & (y(q)== 0) & (z(q) == 0)
        r=q;
        break
    else r=nmax;
    end
end

for i=1:r-1

    m11 = x(i)^2 ;
    m12 = y(i)^2 ;
    m13 = z(i)^2 ;
    m14 = x(i)*y(i);
    m15 = x(i)*z(i);
    m16 = y(i)*z(i);

    m21 = x(i) ;
    m22 = y(i) ;
    m23 = z(i) ;
    m24 = 1 ;

    Q = [m11 m12 m13 m14 m15 m16 m21 m22 m23 m24];
```

```
    R = [m21 m22 m23 m24];

    for j=1:10
      mat(i,j+10*n) = Q(j);
    end

end

end

csvwrite('FinalTest',mat);

mat3 = zeros(nvoids,3);
L2 = load('FinalTest');

for n=0:(nvoids-1)

x2 = L2(:,1+10*n);
y2 = L2(:,2+10*n);
z2 = L2(:,3+10*n);
xy = L2(:,4+10*n);
xz = L2(:,5+10*n);
yz = L2(:,6+10*n);
x = L2(:,7+10*n);
y = L2(:,8+10*n);
z = L2(:,9+10*n);
ones = L2(:,10+10*n);

for k = 3.5:0.005:10

        S11 = zeros(6,6);
        S12 = zeros(6,4);
        S21 = zeros(4,6);
        S22 = zeros(4,4);
        Do = [-1 k/2-1 k/2-1 0 0 0; k/2-1 -1 k/2-1 0 0 0;k/2-1 k/2-1 -1
0 0 0;
         0 0 0 -k 0 0;0 0 0 0 -k 0;0 0 0 0 0 -k];

        for v=1:nmax
            if (x2 == 0) & (y2 == 0) & (z2 == 0)
                s=v;
                break
                else s=nmax;
            end
        end

        for l=1:s-1

            mi1 = [x2(l) y2(l) z2(l) 2*xy(l) 2*xz(l) 2*yz(l)];
            mi2 = [x(l) y(l) z(l) ones(l)];
            S11 = S11 + transpose(mi1)*mi1;
            S12 = S12 + transpose(mi1)*mi2;
```

```
            S21 = S21 + transpose(mi2)*mi1;
            S22 = S22 + transpose(mi2)*mi2;

        end

    S = S11 - (S12*inv(S22)*transpose(S12));
    Sf = inv(Do)*S;
    [V,D] = eig(Sf);

        for i=1:6
            if D(i,i)>0
                eig1 = D(i,i);
                eigi = i;
            end
        end

    u1 = V(:,eigi);
    u2 = -inv(S22)*transpose(S12)*u1;

    u = transpose([transpose(u1) transpose(u2)]);

    K = [u(1,1) u(6,1) u(5,1); u(6,1) u(2,1) u(4,1); u(5,1) u(4,1)
u(3,1)];

    [V,D] = eig(K);

    q = [u(1,1) u(2,1) u(3,1) u(4,1) u(5,1) u(6,1)];

    check = q*Do*transpose(q);

    if (0.995 <= check) & (check<= 1.005)
     ellipse = check;
     kf = k;
     K;
     [V,D] = eig(K);
     AR = [D(1,1) D(2,2) D(3,3)]
     mat3(n+1,:)= AR;
     break
    end

end

end

csvwrite('AspectRatios',mat3)
```